

UNIVERSITY OF OKLAHOMA
GRADUATE COLLEGE

COMPUTATIONAL INVESTIGATIONS OF RED BLOOD CELL MECHANICAL
TRAUMA AND OF DISEASED RENAL ARTERY HEMODYNAMICS

A DISSERTATION
SUBMITTED TO THE GRADUATE FACULTY
in partial fulfillment of the requirements for the
Degree of
DOCTOR OF PHILOSOPHY

By

LINDEN ALYSSA DOWN
Norman, OK
2011

COMPUTATIONAL INVESTIGATIONS OF RED BLOOD CELL MECHANICAL
TRAUMA AND OF DISEASED RENAL ARTERY HEMODYNAMICS

A DISSERTATION APPROVED FOR THE
DEPARTMENT OF BIOENGINEERING

BY

Dr. Edgar O'Rear, Co-Chair

Dr. Dimitrios Papavassiliou, Co-Chair

Dr. Matthias Nollert

Dr. Rong Gan

Dr. Peter Attar

© Copyright by LINDEN ALYSSA DOWN 2011
All Rights Reserved.

ACKNOWLEDGEMENTS

I would like to thank the following individuals:

Dr. O'Rear, for teaching the class that introduced me to fluid mechanics and encouraging me to continue its study. For always pushing me to shoot for goals I wasn't sure I could achieve and not seeming too surprised when I actually attained some of them.

Dr. Papavassiliou, for introducing me to modeling and always understanding when I ran into stumbling blocks. For always having an idea of how to get past those obstacles, and continually encouraging me and making me feel proud of my work.

Dr. Nollert, for teaching me a different way to think in Unit Ops lab (you may not have realized it, but you did), and for always catching me off guard with an interesting question.

Dr. Gan, for helping me to understand the biomechanics side of the fluids problem I was looking at and for teaching me to go back to the basics when I'm having issues. For always smiling when I came into your office.

Dr. Attar, for greatly contributing to my understanding of the FSI problems I was beginning to tackle, and for continuing to provide guidance and advice in that area.

My friends and family, for always sounding impressed when I talked about graduate school and for attempting to understand any of the work I was doing when I tried to describe it. For always supporting and encouraging me, even when I thought I wouldn't make it.

My parents and brother, for not even entertaining the idea of me failing at anything I ever tried to do, and for always being proud of me. For always making me feel like I could do anything. For always being there.

My husband, for staying here with me (almost) the whole time so I could fulfill my dream without missing you too much. For always being able to calm me down when I would start to feel overwhelmed. For being proud of me, and proud to discuss what I'm doing with anyone, anywhere. For never questioning whether or not I could do it.

TABLE OF CONTENTS

ACKNOWLEDGEMENTS	iv
LIST OF TABLES	viii
LIST OF FIGURES	ix
ABSTRACT	xiv
CHAPTER 1: INTRODUCTION	1
1.1 Hemolysis	1
1.1.1 Significance	1
1.1.2 Estimation Methods	1
1.2 Renovascular Hypertension	6
1.2.1 Renal Artery Stenosis	8
1.2.2 Renal Artery Aneurysm	9
1.3 Using CFD to Study Hemodynamics	12
1.4 Motivation	13
1.4.1 Hemolysis Estimation	13
1.4.2 Renovascular Disease Simulation	14
1.5 Nomenclature	15
1.6 References	16
CHAPTER 2: COMPUTATIONAL METHODS	31
2.1 General Procedure	31
2.2 Modeling Turbulent Flow	32
2.3 Modeling Fluid Structure Interaction	34
2.4 Computational Domain	36
2.4.1 Grid Generation	36
2.4.2 Boundary Conditions	36
2.4.2.1 Fluent	36
2.4.2.2 COMSOL	38
2.4.3 Mechanical Properties for Fluid Structure Interaction	39
2.5 Nomenclature	43
2.6 References	44
CHAPTER 3: HEMOLYSIS ESTIMATION	48
3.1 Introduction to Hemolysis Simulations	48
3.2 FDA Critical Path Initiative	51
3.2.1 Geometry and Flow Conditions	51
3.2.2 Computational Domain	51
3.2.2.1 Boundary Conditions	51
3.2.2.2 Grid	52
3.3 FDA Critical Path Initiative Results	52
3.3.1 Velocity	52
3.3.2 Shear Stresses	53
3.3.3 Reynolds Stresses	53
3.4 Capillary Tube Geometries and Computational Domain	54
3.4.1 Geometries and Flow Conditions	54
3.4.2 Computational Domain	55
3.4.2.1 Boundary Conditions	55

3.4.2.2 Grid	55
3.5 Capillary Tube Results	56
3.5.1 Maximum Shear Stress Along Threshold Streamline	56
3.5.2 Maximum Gradient of Shear with Respect to Displacement . . . Streamline ..	57
3.5.3 Maximum Extensional Components of Stress Tensor . . .Streamline	57
3.5.4 Illustrated Mechanism of Damage Due to Elongational Flow	62
3.6 Turbulent Couette Viscometer Geometry and Computational Domain	64
3.6.1 Geometries and Flow Conditions	64
3.6.2 Computational Domain	64
3.6.2.1 Boundary Conditions	64
3.6.2.2 Grid	65
3.7 Turbulent Couette Viscometer Results	65
3.7.1 Turbulent Kinetic Energy Dissipation Rate	66
3.7.2 Kolmogorov Length Scale	66
3.8 Conclusions	68
3.9 Nomenclature	70
3.10 References	71
CHAPTER 4: RENAL ARTERY STENOSIS	94
4.1 Introduction to Stenoses	94
4.2 Renal Artery Stenosis Geometries and Computational Domains	96
4.2.1 Stenosis Geometries	96
4.2.2 Computational Domain	96
4.2.2.1 Boundary Conditions	96
4.2.2.2 Grid	97
4.3 Two-Dimensional Steady Flow Results	98
4.3.1 Effect of Stenosis Axial Position	98
4.3.2 Effect of Stenosis Shape and Percent Stenosis	100
4.4 Two-Dimensional Time-Dependent Results	102
4.4.1 Effect of Stenosis Shape on Peak Pressure Loss	102
4.5 Three-Dimensional CFD Results – Effect of Stenosis Eccentricity	103
4.6 Conclusions	104
4.7 Nomenclature	106
4.8 References	107
CHAPTER 5: RENAL ARTERY ANEURYSM IN TWO-DIMENSIONS	116
5.1 Renal Artery Aneurysm Geometries and Computational Domain	116
5.1.1 Renal Artery Aneurysm Geometries	116
5.1.2 Computational Domain	117
5.1.2.1 Boundary Conditions	117
5.1.2.2 Grid	117
5.2 Two-Dimensional Steady Results	118
5.2.1 Effect of Aneurysm on Arterial Pressure Loss	118
5.3 Two-Dimensional Deformed Steady Flow Results	119
5.3.1 Effect of Deformation on Arterial Pressure Loss	119
5.4 Conclusions	123
5.5 References	125

CHAPTER 6: RENAL ARTERY ANEURYSM IN THREE-DIMENSIONS	135
6.1 Introduction to Three-Dimensional RAA Model	135
6.1.1 Aneurysm Fluid Structure Interaction Literature Review	135
6.1.2 Three-Dimensional Aneurysm Geometries	135
6.1.3 Computational Domain	137
6.1.3.1 Boundary Conditions	137
6.1.3.2 Grid	137
6.2 Saccular Renal Artery Aneurysm of Main Artery Results	138
6.2.1 Effect of Aneurysm Geometry	138
6.2.2 Effect of Mechanical Properties	139
6.3 Saccular Renal Artery Aneurysm of Main Branch Results	141
6.3.1 Effect of Mechanical Properties	141
6.3.2 Effect of Aneurysm Asymmetry	143
6.4 Conclusions	144
6.5 References	146
CHAPTER 7: CONCLUSIONS	158
7.1 Conclusions	158
7.1.1 Hemolysis	158
7.1.2 Renovascular Hypertension	159
7.2 Suggested Future Work	161
7.3 References	162

LIST OF TABLES

CHAPTER 1

Table 1.1. Large center and case studies that indicate a relationship between renal artery aneurysms and renovascular hypertension. These cases indicate that renal artery aneurysms are related to a curable form of renovascular hypertension. Page 30.

CHAPTER 3

Table 3.1: Summary of simulation parameters and results. Capillary diameter - 0.035 cm. Maximum - maximum value on threshold streamline. Page 93.

CHAPTER 5

Table 5.1 Calculated pressure losses for renal arteries with various aneurysms. Page 133.

Table 5.2. Calculated pressure losses for various aneurysms with imposed occlusions. Page 134.

CHAPTER 6

Table 6.1. Saccular aneurysm of the main artery simulations performed. Page 156.

Table 6.2. Saccular aneurysm of the main branch simulations performed. P/D = Proximal Aneurysm Young's Modulus/Distal Aneurysm Young's modulus for aneurysm with variable stiffness. Page 157.

LIST OF FIGURES

CHAPTER 1

Figure 1.1 Nozzle Geometry Specified by FDA Critical Path Initiative. The geometry was designed to include features relevant to medical devices, and to be modeled under conditions thought to produce hemolysis. Page 25.

Figure 1.2. Schematic of simulation domain for a 3:1 contraction from Keshaviah's work. A) Axial view of constriction geometry. B) Cross sectional view of constriction. The average number of nodes for all simulated capillaries was approximately 710,000 with an average computational cell size at the entrance of the capillary on the order of magnitude of $5 \times 5 \mu\text{m}$. Page 26.

Figure 1.3. Sutura et al.'s turbulent Couette viscometer geometry. For simulation simplicity, only $1/16^{\text{th}}$ of the viscometer geometry was modeled. Page 27.

Figure 1.4. Stenosis geometries. A) Characteristic stenosis dimensions. B) Characteristic shape of elliptical stenosis. C) Characteristic shape of Shalman "conical" type stenosis. D) Characteristic shape of Young "blunt" type stenosis. Page 28.

Figure 1.5. Renal artery aneurysm geometries. A) Fusiform aneurysm of the main branch. B) Wide-necked, saccular aneurysm of the main branch. C) Saccular aneurysm of the main artery. D) Saccular aneurysm of the main branch. D) Characteristic diameters of the branches of the renal artery modeled in 2D. Page 29.

CHAPTER 2

Figure 2.1. Example 3D meshes. A) An example hexahedral mesh used in 3D Fluent simulations. B) An example tetrahedral mesh used in 3D COMSOL simulations. Page 46.

Figure 2.2. Example hexahedral mesh used in 3D Fluent simulations. Page 47.

CHAPTER 3

Figure 3.1. A) Contours of velocity magnitude at the corner of a 27 to 1 contraction ($Re = 1055$; $\mu = 0.005 \text{ Pa}\cdot\text{s}$). Flow is from left to right. The threshold streamline is shown, and the hemolysis and hemolysis free zones are illustrated. The volumetric flow rate passing through the area between the threshold streamline and the vessel wall as a percentage of the total volumetric flow is equal to the percent hemolysis for this experiment. The boundaries are not shown, but are similar to those given in Figure 1. B) The expected shear stress profile along the threshold streamline, with the large increase in shear stress magnitude at the entrance highlighted. CFD simulations indicate that there is a large peak in shear stress at the entrance followed by a constant shear stress value in the capillary. The peak in shear stress occurs at a streamline length, $s = 0.45 \text{ cm}$, which corresponds to $z = 0.1038 \text{ cm}$. Page 74.

Figure 3.2. Velocity vectors and contours of velocity magnitude for the conical diffuser orientation of the FDA CPI nozzle. Page 75.

Figure 3.3. Velocity vectors and contours of velocity magnitude for the sudden expansion orientation of the FDA CPI nozzle. Page 76.

Figure 3.4. Contours of shear stress magnitude for the conical diffuser orientation of the FDA CPI nozzle. Page 77.

Figure 3.5. Contours of shear stress magnitude for the sudden expansion orientation of the FDA CPI nozzle. Page 78.

Figure 3.6. Contours of Reynolds stress magnitude for the conical diffuser orientation of the FDA CPI nozzle. Page 79.

Figure 3.7. Contours of Reynolds stress magnitude for the sudden expansion orientation of the FDA CPI nozzle. Page 80.

Figure 3.8. Contours of shear stress magnitude at the entrance of a sharp contraction (CR = 27:1; Re = 1055; $\mu = 0.005$ Pa-s). High shear stresses are seen at the corner of the contraction, and a plume of elevated shear stress magnitude is seen to extend into the capillary. CR: Contraction Ratio. Page 81.

Figure 3.9. Peak shear stress on threshold streamline versus percent hemolysis. The slope of the trendline shows the lack of a consistent threshold peak shear stress across investigated parameters. Hemolysis threshold streamline is chosen such that the "hemolysis zone" shown in Figure 2 encompasses a fraction of the flow equal to the percent hemolysis from Keshaviah's data. CR: Contraction Ratio. Page 82.

Figure 3.10. Peak gradient of shear stress with respect to displacement along a streamline on the threshold streamline versus percent hemolysis. The data does not indicate a constant threshold value for the gradient of the shear stress, and lower gradients are observed for the higher viscosity experiments, even though hemolysis is higher. CR: Contraction Ratio. Page 83.

Figure 3.11. **A)** Peak radial stress tensor component on threshold streamline versus percent hemolysis for various contraction ratios and viscosities. **B)** Peak axial stress tensor component on threshold streamline versus percent hemolysis for various contraction ratios and viscosities. For both plots, a regression of the data is shown – for both extensional components, the slope of the regression is smaller than that for the shear stress. Page 84.

Figure 3.12. Comparison of τ_{rz} and τ_{rr} along the threshold streamline for a single experimental scenario (Re = 1055; $\mu = 0.005$ Pa-s). This plot shows that τ_{rr} has a sharp peak at the entrance of the capillary and then drops to zero once in the capillary, while the shear stress peaks at the entrance, but then maintains a value of the same order of magnitude as the peak through the capillary. This indicates that the effect of τ_{rr} is concentrated at the entrance of the capillary, while that of τ_{rz} likely would be an important effect throughout the capillary, contrary to the entrance-effect conclusions of Keshaviah. Page 85.

Figure 3.13. Contours of shear stress magnitude for (A) a tapered geometry with a high volumetric flow rate and (B) a 27 to 1 sharp contraction with a low flow rate. For (A) Re = 1173; $\mu = 0.005$ Pa-s; For (B) CR = 27:1; Re = 706; $\mu = 0.005$ Pa-s. Page 86.

Figure 3.14: Velocity components in the red blood cell membrane (seen from above) according to Fischer: $v_x = fC(y)$ and $v_y = 0$ where f is the tank-tread frequency. Page 87.

Figure 3.15: Percent hemolysis versus maximum rate of turbulent kinetic energy dissipation on the threshold iso-surface (i.e. percent volume isolated by iso-surface = percent hemolysis). No threshold value for ϵ is apparent. Page 88.

Figure 3.16: Kolmogorov Length Scales for two gap shear values and, correspondingly, two levels of hemolysis. Length scales of the size of a RBC are found at both rotational rates, with a larger portion of the flow exposed to smaller KLS in the case with more hemolysis. Page 89.

Figure 3.17: Percent hemolysis/Percent volume isolated by KLS iso-surface versus gap shear stress. If a threshold KLS were evident, Sutura's data would fall on the same curve as the data points for one of the Kolmogorov Length Scales, however it does not. Page 90.

Figure 3.18: Percent hemolysis versus median Kolmogorov Length Scale. The plot shows a dependence of hemolysis on median KLS, with smaller median KLS values indicating more hemolysis. The size range for a RBC is shown for comparison. Page 91.

Figure 3.19: Kolmogorov Length Scales for the FDA CPI nozzle geometry in the sudden expansion orientation, at $Re = 5000$. Kolmogorov Length Scales on the same order of magnitude as the size of a RBC are seen. Page 92.

CHAPTER 4

Figure 4.1. 3D model of abdominal aorta, renal arteries and renal branches with an 80% stenosis located at 0.9 normalized axial position. The insets show the velocity profile as blood enters the renal artery from the abdominal aorta and the velocity profile in and immediately after the stenosis. The velocity profile entering the renal artery is drastically different from the flat velocity profile given in previous, renal artery only simulations. Page 110.

Figure 4.2. Pressure loss versus axial location for a renal artery. In this system, the abdominal aorta, the renal arteries, and the main renal artery branch are simulated in order to achieve a more realistic inlet velocity profile and outlet conditions. Simulation conditions are: steady flow; elliptical stenosis; blood viscosity, 0.004 Pa s; blood density, 1060 kg/m³; blood flow rate through renal artery, 10 mL/s; renal artery diameter, 5 mm; renal artery length, 50 mm; for 50% stenosis, laminar model; for 64% and 80% stenosis, turbulent k- ϵ model. Page 111.

Figure 4.3. Pressure loss versus percent stenosis. Results show a clear critical percent occlusion near 75% stenosis. Simulation conditions are: steady flow; blood viscosity, 0.004 Pascal second; blood density, 1060 kg/m³; blood flow rate through renal artery, 10 mL/second; up to 50% stenosis, laminar model; higher than 50% stenosis, turbulent k- ϵ model. Page 112.

Figure 4.4. Pressure loss versus time for one pulse. Results show that hemodynamically significant pressure loss occurs for a 75% stenosis and that the stenosis structure is important in determining the pressure loss across a constriction. Simulation conditions are: unsteady flow; blood viscosity, 0.004 Pascal second; blood density, 1060 kg/m³; 75% stenosis; turbulent k- ϵ model. Page 113.

Figure 4.5. Velocity profiles in and immediately following an 80% stenosis placed at the center of a 5 cm renal artery. Starting from the top image, the stenosis is moved progressively closer to the center of the artery in these 3D simulations until the stenosis and the artery are co-axial (eccentricity = 0). Page 114.

Figure 4.6. Pressure loss versus stenosis eccentricity. Eccentricity is defined as the distance between the axial center of the artery and the axial center of the stenosis divided by the stenosis radius. This definition means the upper limit of eccentricity increases with the extent of occlusion. In other words, the smaller the stenotic lumen, the closer its center can approach the wall of the artery. Simulation conditions are: steady flow; elliptical stenosis; blood viscosity, 0.004 Pascal second; blood density, 1060 kg/m³; blood

flow rate through renal artery, 10 mL/second; for 50% stenosis, laminar model; for 80% stenosis, turbulent k- ϵ model. Page 115.

CHAPTER 5

Figure 5.1. (A) Saccular aneurysm of the renal artery (Degertikin)*; (B) 2D mesh representative of pathologic geometry given in Degertikin, et al. (dimensions 33 x 31 mm). Page 128.

Figure 5.2. Possible progression of occlusion of the renal artery by aneurysm cusp. Pressure values in A, B, C and D are mm Hg. A) Saccular renal artery aneurysm of the main bifurcation; B) Close-up showing higher pressure inside the aneurysm when compared to pressure in arterial branches; C) Initial deflection of the aneurysm cusp into the blood stream – the pressure difference across the cusp is larger than before deformation; D) Aneurysm cusp occluding the arterial branches with high pressure on the upstream side of the cusp - up to a 5 mm Hg pressure difference across the cusp. Page 129.

Figure 5.3. Increase in pressure loss across the renal artery with increasing percent occlusion for the saccular aneurysm of both the main artery and the main branch. The dashed line shows where the physiologically relevant pressure loss is reached. Page 130.

Figure 5.4. Illustration of the proposed mechanism of occlusion for the saccular aneurysm of the main renal artery. Page 131.

Figure 5.5. The effect of geometry on the predicted correlation between aneurysms and hypertension. A) Pressure inside the fusiform aneurysm would tend to force the walls of the aneurysm outward, B) Similar to the fusiform aneurysm, the walls of the mild saccular aneurysm would be forced outward; C) The forces acting on the walls of the saccular aneurysm with neck would tend to deform the aneurysm lip into the blood stream. Page 132.

CHAPTER 6

Figure 6.1. Saccular Aneurysm of Main Artery Geometry. The aneurysm is located in the middle of the artery, which has a length of 50 mm. A 1.5 mm aneurysm is shown. Inset: Original (heavy line) and revised (light line) neck geometries. Page 149.

Figure 6.2. Saccular aneurysm of the main branch geometry. A) Cut-away view of artery and aneurysm. B) Exterior view of artery and aneurysm. It is clear that the aneurysm is resting tightly against the artery branch. C) and D) Two different perspectives of the entrance to the artery, showing the opening in the artery wall that leads to the anerysm. E) Cut-away view of aneurysm, with cusp domain highlighted in red. Page 150.

Figure 6.3. Decreasing Young's modulus for symmetric saccular aneurysm of the main artery. The perspective on the left is looking down the upper branch, towards the occlusion. From top to bottom, the cusp Young's moduli are 1×10^5 , 5×10^4 , 1×10^4 , 5×10^3 and 1×10^3 Pa. The deflection of the cusp increases with decreasing Young's modulus. Page 151.

Figure 6.4. Decreasing Young's modulus for symmetric saccular aneurysm of the main artery, thin cusp. The perspective on the left is looking down the upper branch, towards the occlusion. From top to bottom, the cusp Young's moduli are 1×10^5 , 5×10^4 , 1×10^4 ,

5×10^3 and 1×10^3 Pa. The deflection of the cusp increases with decreasing Young's modulus. Page 152.

Figure 6.5. Percent Occlusion versus cusp Young's modulus for a symmetric aneurysm of the main branch. The measured maximum percent occlusion increases with decreasing Young's modulus, and also with a thinner wall. Thick = 1 mm. Thin = 0.5 mm. Page 153.

Figure 6.6. Decreasing Young's modulus for asymmetric saccular aneurysm of the main artery. The perspective on the left is looking down the upper branch, towards the occlusion. From top to bottom, the cusp Young's moduli are 1×10^5 , 5×10^4 , 1×10^4 , and 5×10^3 Pa. The deflection of the cusp increases with decreasing Young's modulus. Page 154.

Figure 6.7. Decreasing Young's modulus for asymmetric saccular aneurysm of the main artery, thin cusp. The perspective on the left is looking down the upper branch, towards the occlusion. From top to bottom, the cusp Young's moduli are 1×10^5 , 5×10^4 , 1×10^4 and 7.5×10^3 Pa. The deflection of the cusp increases with decreasing Young's modulus. Page 155.

ABSTRACT

In this work, Computational Fluid Dynamics (CFD) and Fluid Structure Interaction (FSI) methods were used to study two separate problems: red blood cell damage in flow and the hemodynamics of diseased renal arteries; specifically, those with renal artery stenoses or aneurysms.

The study of red blood cell trauma was motivated by deficiencies in the current empirical models used for hemolysis estimation. Using CFD, classic hemolysis experiments performed in capillary tubes for laminar flow and a Couette viscometer for turbulent flow were re-examined. The results of the capillary tube simulations indicated that the extensional stresses present in the flow contributed to hemolysis, with a threshold value of approximately 3000 Pa for exposure times on the order of microseconds being indicative of hemolysis. In the turbulent Couette viscometer simulations, where experimental exposure times were five minutes, it was found that Kolmogorov Length Scales of the same order of magnitude as the size of a red blood cell were indicative of hemolysis, with some dependence on the median Kolmogorov Length Scale in the flow. The results of an inter-laboratory FDA study are also reported.

Simulations of diseased renal arteries were also performed, which included simulations of stenoses and aneurysms of varying geometries. Initially, this work was done solely with CFD, however FSI was eventually incorporated into the renal artery aneurysm simulations. The results of this study indicate that the uncertain relationship between renal artery aneurysms and renin-dependent hypertension is possibly related to transient occlusions of the artery that occur when high pressure within the aneurysm causes the aneurysm and underlying vessel wall to deform into the blood stream.

CHAPTER 1: INTRODUCTION

1.1 Hemolysis

1.1.1 Significance

Interest in the rheology of the erythrocyte in the mid-20th Century grew out of an appreciation of the role of the red cell in diseases like sickle cell anemia and also the susceptibility of red blood cells (RBCs) to hemolysis in medical devices emerging at the time. Cell damage observed even today with prosthetic heart valves (Ge, 2008; Simon, 2007), cardiopulmonary bypass (Kang, 2010), and artificial kidneys contributes to anemia, along with the toxic effects associated with free hemoglobin in the circulatory system (Polaschegg, 2009). The cause of mechanical trauma to blood cells has been attributed to large frictional forces or shear stresses (Leverett, 1972), which are associated with the flow of blood through such devices.

Factors and conditions resulting in hemolysis were established by using well-defined flow systems in the laboratory. Such work led to an understanding that hemolysis depends on both exposure time and on the magnitude of the shear stress, when data generated by various techniques at different labs were considered in aggregate (Leverett, 1972; Nevaril, 1969; Sutura, 1975). Inversely related, short exposures to high stresses or long exposures at lower stresses cause cell destruction (Giersiepen, 1990).

1.1.2 Estimation Methods

Many investigators sought to develop mathematical expressions to predict the fraction of cells lysed based on this theoretical relationship between shear stress and exposure time (Arvand, 2005; Bludszuweit, 1995; Chan, 2002; Giersiepen, 1990; Song, 2003). A power-law equation typically related free hemoglobin to the product of stress

and exposure time, each raised to a power determined from a fit to experimental data. While these equations have been helpful in understanding mechanical trauma, empirical models of hemolysis as a function of shear stress and exposure time have fallen short over the years in fully characterizing lethal damage to RBCs. Results from application of correlations to predict hemolysis quantitatively have been disappointing, and for various reasons some researchers have proposed amendment of the power law model or the use of entirely different models (Arvand, 2005; Behbahani, 2009; Chen, 2010; Goubergrits, 2004; Grigioni, 2005; Gu, 2005; Kataoka, 2006; Kim, 2009; Paul, 2003).

One of the problems with these empirical models relates to the cell's exposure. Differences in the nature of shear stress exposure in controlled laboratory conditions compared to the reality of clinical settings contribute to inaccuracies of the power-law model of hemolysis estimation. The clinical situation in blood contacting devices has been described as localized regions of high stress, "hot spots", with very short exposure times (Zhao, 2006). Grigioni et al. cited the fact that prior estimations were derived using experimental set-ups that yielded a constant, uniform shear – which did not take into account repetitive transient loading on the cells, a common scenario in many blood contacting devices (Grigioni, 2004). Some investigators have recognized the potential importance of the history of mechanical loading in blood trauma and its combination with resistance of cells to accumulated damage (Chan, 2002; Yeleswarapu, 1995). As such, the inability of current power-law models to account for the past shear history of a cell adds to the inaccuracy of their predictions (Grigioni, 2004; Gu, 2005), where, for example, sub-hemolytic trauma to cells can leave them more susceptible to rupture when subjected to shear yet again. Antaki also discussed the utility of power law models and concluded

that they are unable to capture the effects of subtle features of the blood contacting geometry, which have been shown to largely affect hemolysis (Antaki, 2008). Previous researchers have attempted to use current blood damage power-law models to estimate hemolysis from Computational Fluid Dynamics (CFD) results, often using a Lagrangian approach (Gu, 2005; Mitoh, 2003; Yano, 2003), where damage was calculated along multiple streamlines in the domain of interest. These conventional models provide poor estimates of hemolysis when compared to experimental hemolysis data in the same flow system, thus these investigators have illustrated the inaccuracy of current models for hemolysis prediction. These shortcomings are important because they compromise the validity of catastrophic damage estimates made by engineers working on the design, development and improvement of life-saving medical devices (Girdhar, 2008; Zhang, 2008).

In 2009, a total of 28 groups across the country participated in an FDA Critical Path Initiative titled “Standardization of Computational Fluid Dynamic Techniques Used to Evaluate Performance and Blood Damage Safety in Medical Devices.” These groups performed numerical simulations to predict stress levels and hemolysis in a model flow with features known to cause hemolysis, particularly turbulent blood flow through a sudden contraction or sudden expansion. As a part of that group, simulations were performed on the given nozzle geometry (Figure 1.1). A total of 10 scenarios were simulated, representing the two different orientations and flow in both the laminar and turbulent regimes. The results obtained from this investigation prompted the study of two other experimental systems at the University of Oklahoma, in an effort to further elucidate the effects of flow on red blood cell damage.

The first of these was a set of classical hemolysis experiments in capillary tubes by Keshaviah (Keshaviah, 1974). Keshaviah studied hemolysis in small diameter capillary tubes with an emphasis on the effect of entrance geometry. His experimental procedure was to force diluted washed RBCs into a capillary, varying the ratio of the larger antechamber diameter to the capillary diameter, as well as the fundamental geometry of the entrance (i.e., sharp edged versus tapered). In this work, the capillary experiments performed by Keshaviah were recreated using computational fluid dynamics (CFD). An example of one of the experimental geometries simulated can be found in Figure 1.2.

The initial aim of this analysis was to ascertain the critical level of shear stress required for cell lysis. In the absence of a consistent finding, the effects of extensional flow at the capillary entrance were explored. Results from this analysis provided evidence that hemolysis in this laminar shearing flow can be more closely related to extensional stresses than shear stresses, and indicate that new models should consider extensional stress as well as exposure history for accurate hemolysis predictions.

The nature of steady elongational flow is such that it is difficult to study experimentally with adjacent fluid elements separating at an exponential rate (Bird, 1987). McGraw, in a thesis supervised by Frattini, was the first to examine the deformation of the erythrocyte in a miniaturized extensional flow rheometer under a microscope (McGraw, 1992). They obtained larger cell deformations for extensional flows, aspect ratios of 2.0 to 5.9, than those observed for a shearing flow at comparable stress levels (Chien, 1992). Just recently, Lee et al. examined red cell deformability in a microfluidic device where both extensional and shear flow effects were compared.

Deformability as gauged by the Deformability Index, $DI = (L-B)/(L+B)$ where L and B are semiaxial lengths of the deformed cell, was found to be 0.51 and 0.29 at 3.0 Pa for extensional and shearing flows, respectively (Lee, 2009). Taking the greater deformation into account and the fact that extensional flows of liquids more readily result in drop breakup, Lee noted the insufficiency of existing hemolysis models that focus only on shear stress.

Lee's observation of relative deformability for extensional and shear stresses is particularly notable in light of an elegant analysis incorporating the stress tensor to characterize mechanical trauma of the red cell (Arora, 2004). In this work, Arora et al. obtained the following equation for hemolysis:

$$\frac{\Delta Hb}{Hb} = 3.62 \times 10^{-7} \left(\mu_{blood} \sqrt{\frac{f_1^2 DI^2}{(1-DI^2)f_2^2}} \right)^{2.416} t^{0.785} \quad (1.1)$$

where f_1 and f_2 are constants, Hb is hemoglobin concentration, t is exposure time, μ_{blood} is the viscosity of blood, and DI is a distortion index synonymous with the deformability index defined by Lee et al. Ultimately, the tensor analysis by this group is based only on shear stress, but, interestingly, the final expression (Equation 1.1) includes as a key dynamic factor the "distortion index" of the cell. According to Lee, DI approaches constant values of 0.6 and 0.55 as stress increases for extensional and shear flows, respectively. If the Arora equation also reflects the dependence on DI for extensional flows, then the small difference in DI above suggests 40% greater likelihood of hemolysis in extensional flow compared to a shearing flow.

Others have reported cell damage in the presence of extensional flow (Gregoriades, 2000; Lokhandwalla, 2001; Mollet, 2008). Lokhandwalla and Sturtevant,

for example, noted the presence of extensional flow with hemolysis from shock wave lithotripsy (Lokhandwalla, 2001). When working with hamster ovary cells, Mollet et al. found that high levels of cell damage were seen in areas of high extensional stress (Mollet, 2008). Although ovarian cells are much different from red blood cells, it would not be unreasonable to assume the same mechanisms might affect RBCs and ovarian cells alike. To date, no one has provided evidence that extensional stresses in a typical flow cause hemolysis. Some studies have speculated that extensional stress may be related to membrane breakup, however this work is the first to provide a link between a threshold value of extensional stress and red cell hemolysis.

Finally, in addition to the nozzle geometry and the capillary geometry, simulations were used to model flow in a Couette viscometer (Sutera, 1975). In work performed by Sutera et al., hemolysis related to shear stress was investigated using a viscometer with a rotating inner cylinder, in which turbulence could be achieved. Sutera found a critical shear stress of 2500 – 3000 dynes/cm² for exposure times of 2 minutes. The experimental geometry from Sutera's work is illustrated in Figure 1.3. The simulation of this experimental work allowed for a closer examination of hemolysis occurring in turbulent flow, so that both laminar and turbulent regimes were examined in the hemolysis portion of this work.

1.2 Renovascular Hypertension

Secondary hypertension afflicts millions of adults in the United States with underlying causes often being associated with the kidney. It is well-established that altered geometry and flow of the renal artery can lead to renin-dependent hypertension.

This was notably illustrated in experiments by Goldblatt, who induced renin-dependent hypertension in dogs by placing clamps on the renal arteries (Goldblatt, 1934). Clinically, the potential to alter systemic blood pressure in a similar way by changing the vessel structure occurs with renal artery stenoses (Harman, 2003; Serter, 2007), transplanted renal artery complications (Al-Harbi, 1998) and congenital defects (e.g. elongated renal arteries) (Kem, 2005). It is thought that this renovascular hypertension frequently is caused by a malfunction in the renin-angiotensin-aldosterone system (RAAS), in which unwarranted vasoconstrictors are released, causing systemic hypertension. Not only can this system failure lead to hypertension, but persistently high levels of angiotensin II and aldosterone can also lead to vascular and myocardial remodeling, abnormal endothelial functioning, inflammation and plaque susceptibility (Hackman, 2007).

Hormonal imbalances of the RAAS, like those occurring with stenoses, have been linked to mechanical factors. It is well known that flow across a constriction or stenosis causes a localized drop in pressure. In the case of the stenotic renal artery, juxtaglomerular cells in the afferent arteriole of the kidney respond to changes in arterial blood pressure (Phillips, 2005) (i.e., baroreceptors) and register lower than normal values, which are incorrectly interpreted as low systemic pressure. An average pressure loss as small as 10 mm Hg or a peak pressure loss of 20 mm Hg across a renal artery stenosis is considered hemodynamically relevant by physicians, meaning that this level of pressure loss is capable of causing a malfunction in the RAAS (Jaff, 2001; Yim, 2004).

1.2.1 Renal Artery Stenosis

Generally, arterial stenosis is defined as a constriction or narrowing of the artery, and is capable of causing physiologically significant pressure losses as blood flows through an artery. This change in pressure can have adverse implications for the functioning of many of the body's systems. Carotid artery stenosis is a severe example of an arterial constriction; it can cause insufficient perfusion and can give rise to a transient ischemic attack (Caplan, 2008). A second example is renal artery stenosis - the most common cause of renovascular hypertension, a leading cause of end-stage renal disease in dialysis patients and an independent predictor of cardiovascular complications such as myocardial infarction (White, 2009).

How a stenosis leads to a large pressure loss can be understood from principles of fluid dynamics and laboratory experiments with model stenoses (Young, 1979; Shalman, 2001). Young et al. developed a correlation relating the pressure drop across a stenosis to blood vessel dimensions, flow characteristics, and stenosis dimensions for a blunt geometry (Young, 1979). Shalman et al., used a summation of pressure drops across the axisymmetric, converging, straight, and diverging portions of a stenosis as a method for estimating the pressure drop across an atherosclerotic coronary artery (Shalman, 2001). Yim et al. adapted the stenosis model used by Shalman for comparison to Computational Fluid Dynamics (CFD) calculations based on MR angiography and phase contrast MR data from a renal artery with stenosis and experimental measurements using a glass model (Yim, 2004).

Here, the hemodynamics of various stenosis geometries have been investigated using CFD, specifically stenoses comparable in size to a renal artery stenosis (Kem,

2005). The goal of these simulations was to elucidate the effects of various geometric properties of stenoses on the pressure loss across a stenotic renal artery. The characteristic dimensions and geometries simulated are shown in Figure 1.4. The conical stenosis of Yim's work, the blunt stenosis of Young's work and a more physically realistic elliptical stenosis were all simulated. This work is different from previous computational studies of arteries such as the coronary or carotid, where the goal of the work has been to assess the effect of wall-shear-stress on the development of atherosclerotic plaque. In addition, the flow conditions in the renal artery are unlike those present in other arteries of different dimensions conveying much smaller volumes of blood to the heart or brain. The pressure loss through the renal artery under pathologic conditions is a significant factor for the development of secondary systemic hypertension, and an improved understanding of how the pressure loss is related to changes in arterial structure could allow physicians to make better decisions about surgical intervention using only advanced imaging techniques.

1.2.2 Renal Artery Aneurysm

In addition to renal artery stenosis, renal artery aneurysms have also been shown to be related to renovascular hypertension. As an additional type of geometry alteration, renal artery aneurysms may alter flow sufficiently to affect the pressure difference between the entrance to the renal artery and the baroreceptors in the kidney. Renal artery aneurysms are an expansion of the lumen of the renal artery. The incidence of renal artery aneurysms has been reported as up to 0.1% (Serter, 2007). Although this is not an extremely high figure compared to other types of hypertension, it equates to over a quarter of a million persons in the United States alone, with 70% or more exhibiting

hypertension. Additionally, renal artery aneurysms are being diagnosed more frequently in recent years due to the increased use of non-invasive imaging techniques (Tham, 1983; Gallagher, 2008). It is important that we understand their pathophysiology because the associated hypertension is potentially curable.

Hypertension frequently co-exists in the presence of renal artery aneurysms. In a study involving 168 aneurysmatic patients, Henke et al. found 73% exhibited chronic high blood pressure (Henke, 2001). Four other investigations, ranging in size from 19 to 67 patients, have reported similar incidences of 69-100% (Hubert, 1980; Lumsden, 1996; Bastounis, 1998; Hupp, 1992). Table 1.1 gives a summary of prior studies involving renal artery aneurysms in which most patients exhibited hypertension, the physician performed some sort of clinical intervention, and the hypertension was subsequently eliminated or decreased. There are two basic types of aneurysm - saccular and fusiform. It has been reported that most renal artery aneurysms are saccular, with one large center study showing 79% saccular and 21% fusiform renal artery aneurysms. The most common aneurysm location was the bifurcation of the main renal artery (60%) (Henke 2001).

Though clearly connected, there is much debate as to how renal artery aneurysms relate to hypertension, with no mechanism as yet established to explain the relationship. One interpretation of this correspondence involves renal artery aneurysm being caused by (not causative of) hypertension, though the fact that surgical intervention eliminates or mitigates hypertension in most cases strongly suggests a cause and effect relationship with hypertension being secondary to the presence of the aneurysm. In line with this latter sequence, it has been proposed that renal artery aneurysms lead to hypertension

through mechanical kinking or twisting, thereby forcing altered blood flow, renal embolization, or external compression of the aneurysm (Hartman, 2003). Such explanations, while certainly plausible, lack evidence through formal studies.

The presence of a renal artery aneurysm can lead to serious health complications such as hypertension, hemorrhagic shock and transient ischemic attack. The risk of hemorrhagic stroke is not considered to be great with renal artery aneurysms unless the aneurysm is very large or subjected to changes in blood flow that may induce rupture, such as in pregnancy or blunt trauma. These two morbidities, renovascular hypertension and rupture, associated with renal artery aneurysm are the most commonly discussed in clinical case studies on renal artery aneurysms. Currently, when renal artery aneurysms are diagnosed, usually either incidentally or in an attempt to diagnose uncontrolled hypertension, the decision whether or not to surgically intervene is made based on a few factors. For women who are pregnant or are of childbearing age, an aneurysm of any size is considered dangerous because of the risk of rupture. In other situations, however, the decision is not so clear and is typically based on the size of the aneurysm. Currently, there is not a consensus among physicians concerning when a renal artery aneurysm should be removed or excluded, or simply monitored, with estimates of the critical aneurysm size ranging from 0.5 - 1.5 cm in diameter (Henke 2001).

Because of their close relationship to renovascular hypertension, a computational investigation of the effect of renal artery aneurysms on renovascular hemodynamics was undertaken. Initially this was done using a 2D, rigid wall model and when interesting results arose, this model was extended to a 3D, fluid structure interaction model in which the flow was allowed to influence the distensible artery walls and vice versa. The

geometries investigated in the 2D rigid wall simulations are shown in Figure 1.5, and included A) a fusiform aneurysm of the main branch, B) a wide-neck, saccular aneurysm of the main branch, C) a saccular aneurysm of the main artery and D) a saccular aneurysm of the main branch. Similar aneurysms were modeled in 3D – the details of these geometries can be found in Chapter 5.

1.3 Using CFD to Study Hemodynamics

CFD is a powerful analysis tool, which has been widely used to assess the effect of wall-shear-stress on the development of atherosclerotic plaque in the aorta and renal arteries (Buchanan, 2003; Liang, 2006; Steinman, 2002; Taylor, 1998), to model normal and pathologic coronary arteries as well as carotid arteries (Shalman, 2001; Goubergrits, 2009; Suo, 2008; Wentzel, 2005; Nguyen, 2008) and to assess the effects of hemodynamics in cranial aneurysms (Castro, 2006; Dempere-Marco, 2006; Hoi, 2006; Shojima, 2004). CFD has also been used by multiple investigators to assess the role of fluid dynamics in red blood cell trauma – in both experimental flow loops, and in blood contacting devices (Zhao, 2006; Gu, 2005; Mitoh, 2003; Yano, 2003; Kameneva, 2004). The advantage of using CFD to investigate both the macro effects of blood flow on arterial wall movement, and the micro effects of stresses on red blood cells is that CFD allows for the investigation of many geometries and flow conditions, and is also able to provide certain details about the flow that are difficult to obtain experimentally. In this work, the power of CFD has been used to augment the current understanding of certain aspects of the effect of flow on red blood cells, and to provide novel insights into the effect of hemodynamics on multiple aspects of renovascular health.

1.4 Motivation

1.4.1 Hemolysis Estimation

Interest in mechanical trauma remains high as evidenced by the FDA Critical Path Initiative. Currently, an estimation of hemolysis from computations can vary widely depending on the choices and assumptions made by the user performing the simulation. Specifically, the numerical method, the type of computational mesh, the order of convergence and the turbulence model chosen are among the factors that are important to the simulation outcome. Using experimental measurements by three different laboratories as the basis for validating the computational results, the FDA sought to identify the most accurate model. Preliminary results of this analysis have been presented and the wide variation in results for flow calculations and hemolysis estimations indicates the need for both new physical insights and numerical approaches (Hariharan, 2010; Stewart, 2009).

The ongoing problems with predicting hemolysis during flow suggest a continuing need to re-examine the theoretical basis for mechanical trauma. Keshaviah concluded that hemolysis in his experiments was related to the structure of the entrance to the capillary. For example, a tapered entrance caused only 0.1% hemolysis while a blunt entrance region at the same flow conditions resulted in a much higher level of cell damage at 5.9%. These findings suggested that examination of the entrance region with CFD might lead to new insights into mechanism(s) of catastrophic damage to erythrocytes during flow. With CFD, the nature of the flow in the entrance region of Keshaviah's experimental setup was examined more closely. The effect of turbulence on red blood cell damage is also receiving continued scrutiny, and an investigation of the

turbulent Couette viscometer work of Suter with CFD allowed for a renewed and detailed study of the effects of this type of flow as well.

1.4.2 Renovascular Disease Simulation

It is widely accepted in the literature that a hemodynamic effect due to the presence of a renal artery stenosis can lead to renin-dependent hypertension. However, parametric numerical studies of stenoses of a comparable size to renal artery stenosis did not represent physiologically realistic stenosis shapes, and lacked investigation into some parameters that might be influential. Although renal artery aneurysms would not be expected to have the same hemodynamic effect as a constriction, there is evidence that some effect of the fluid flow on the renin-angiotensin-aldosterone system occurs in this case as well. A better understanding of this phenomenon is greatly needed, and would be very beneficial to physicians in their clinical decision making. Computational modeling can provide a better idea of the hypertension related pathology of renal artery stenosis and renal artery aneurysms, and ultimately lead to better patient care.

Portions of this chapter have been reproduced from the following sources:

Down LA, Papavassiliou DV, O’Rear EA. *Significance of Extensional Stresses to Red Blood Cell Lysis in a Shearing Flow*. Annals of Biomedical Engineering. 2011; 39: 1632 – 1642.

Heflin LA, Street CB, Papavassiliou DV, O’Rear EA. *A Computational Investigation of the Geometric Factors Affecting the Severity of Renal Arterial Stenoses*. Journal of Biorheology. 2009; 23: 102-110.

Heflin LA, Street CB, Papavassiliou DV, Kem DC, Wu DH, O’Rear EA. *Transient Stenotic-Like Occlusions as a Possible Mechanism for Renovascular Hypertension due to Aneurysm*. Journal of the American Society of Hypertension. 2009; 3:192-200.

1.5 Nomenclature

B – cell semiaxial length II

DI – deformability index

f_1 and f_2 – constants

Hb – hemoglobin concentration

L – cell semiaxial length I

t – exposure time (s)

μ_{blood} – viscosity of blood

1.6 References

Al-Harbi A, Chaudry T, Linjawi T, Alfarayh O, Al-Sohaibani H, Al-Shaibani K, et al. Renal Artery Stenosis in Renal Transplantation Presentation and Management. *Saudi J Kidney Dis Transpl* 1998; 9:22-26.

Antaki J. Computational indices for prediction of flow-induced blood trauma. *Biorheol* 45: 75-76, 2008.

Arora D, Behr M, Pasquali M. A tensor-based measure for estimating blood damage. *Artif. Organs* 1002-1015, 2004.

Arvand A, Hormes M, Reul H. A validated computational fluid dynamics model to estimate hemolysis in a rotary blood pump. *Artif. Organs* 29: 531-540, 2005.

Bastounis E, Pikoulis E, Georgopoulos S, Alexiou D, Leppaniemi A, Boulafendis D. Surgery for renal artery aneurysms: a combined series of two large centers. *Eur Urol* 1998; 33:22-27.

Behbahani M, Behr M, Hormes M, Steinseifer U, Arora D, Coronado O, Pasquali M. A review of computational fluid dynamics analysis of blood pumps. *Eur. J. Appl. Math.* 20: 363-397, 2009.

Bird RB, Armstrong RC, Hassager O. in *Dynamics of Polymeric Liquids*. Vol. 1, 2nd Ed.: Fluid Mechanics. (John Wiley & Sons, New York) pp. 103. 1987.

Bludszuweit C. Model for a general mechanical blood damage predication. *Artif. Organs* 19: 583-589, 1995.

Buchanan J, Kleinstreuer C, Hyun S, Truskey G. Hemodynamics simulation and identification of susceptible sites of atherosclerotic lesion formation in a model abdominal aorta. *J Biomech* 2003; 36:1185-1196.

Caplan L. A 70-Year-Old Man With a Transient Ischemic Attack. *J Am Med Assoc* 2008; 300: 81-90.

Castro MA, Putman CM, Cebal JR. Patient-specific computational modeling of cerebral aneurysms with multiple avenues of flow from 3D rotational angiography images. *Acad Radiol* 2006; 13:811-821.

Chan WK, Wong YW, Ding Y, Chua LP, Yu SCM. Numerical investigation of the effect of blade geometry on blood trauma in a centrifugal blood pump. *Artif. Organs* 26: 785-793, 2002.

Chen Y, Sharp MK. A strain-based flow-induced hemolysis prediction model calibrated by in vitro erythrocyte deformation measurements. *Artif Organs* 2011; 35: 145-156.

Chien S, Sung LA, Lee MM, Skalak R. Red cell membrane elasticity as determined by flow channel technique. *Biorheol* 1992; 29: 467-478.

Cooney D. *Biomedical Engineering Principles: An Introduction to Fluid, Heat, and Mass Transport Processes*. New York: Marcel Dekker, 1976.

Dempere-Marco L, Oubel E, Castro M, Putman C, Frangi A, Cebal J. CFD analysis incorporating the influence of wall motion: application to intracranial aneurysms. *Med Image Comput Comput Assist Interv Int Conf Med Image Comput Comput Assist Interv* 2006; 9(Pt 2):438-445.

Gallagher K, Phelan M, Stern T, Bartlett S. Repair of complex renal artery aneurysms by laparoscopic nephrectomy with ex vivo repair and autotransplantation. *J Vasc Surg* 2008; 48: 1408-1413.

Ge L, Dasi LP, Sotriopoulos F, Yoganathan AP. Characterization of hemodynamic forces induced by mechanical heart valves: reynolds vs. viscous stresses. *Ann. Biomed. Eng.* 36: 276-297, 2008.

Giersiepen M, Wurzinger LJ, Opitz R, Reul H. Estimation of shear-related blood damage in heart valve prostheses – in vitro comparison of 25 aortic valves. *Int. J. Artif. Organs* 13(5): 300-306, 1990.

Girdhar G, Bluestein D. Biological effects of dynamic shear stress in cardiovascular pathologies and devices. *Expert. Rev. Med. Devices* 5:167-181, 2008.

Goldblatt H, Lynch J, Hanzal R, Summerville W. Studies on Experimental Hypertension I. The production of persistent elevation of systolic blood pressure by means of renal ischemia. *J Exp Med* 1934; 59:347-379.

Goubergrits L, Affeld K. Numerical estimation of blood damage in artificial organs. *Artif. Organs* 499-507, 2004.

Goubergrits L, Wellnhofer E, Kertzsch U, Affeld K, Petz C, Hege H. Coronary artery WSS profiling using a geometry reconstruction based on biplane angiography. *Ann Biomed Eng* 2009; 37: 682-691.

Gregoriades N, Clay J, Ma N, Koelling K, Chalmers J. Cell damage of microcarrier cultures as a function of local energy dissipation created by a rapid extensional flow. *Biotechnol. Bioeng.* 69: 171-182, 2000.

Grigioni M, Daniele C, Morbiducci U, D'Avenio G, Benedetto G, Barbaro V. The power-law mathematical model for blood damage prediction: analytical developments and physical inconsistencies. *Artif. Organs* 467-475, 2004.

Grigioni M, Moriducci U, D'Avenio G, Benedetto G, Gaudio C. A novel formulation for blood trauma prediction by a modified power-law mathematical model. *Biomech. Model Mechanbiol.* 4: 249-260, 2005.

Gu L, Smith W. Evaluation of computational models for hemolysis estimation. *ASAIO J.* 51: 202-207, 2005.

Hackam D, Spence J, Garg A, Textor S. Role of renin-angiotensin system blockade in atherosclerotic renal artery stenosis and renovascular hypertension. *Hypertension* 2007; 50:998-1003.

Hariharan P, Giarra M, Reddy V, Day SW, Manning KB, Deutsch S, Burgreen GW, Patterson EG, Myers MR, Berman MR, Stewart SFC, Malinauskas RA. Interlaboratory measurements of flow parameters for comparison to CFD simulations in FDA's nozzle model. *ASAIO J.* 56: 82, 2010.

Hartman R, Kawashima A, King B, Jr. Evaluation of renal causes of hypertension. *Radiol Clin North Am* 2003; 41:909-929.

Heflin L, Street C, Papavassiliou D, Kem D, Wu D, O'Rear E. Transient stenotic-like occlusions as a possible mechanism for renovascular hypertension due to aneurysm. *J Am Soc Hypertens* 2009; 3: 192-200

Henke P, Cardneau J, Welling T, 3rd, Upchurch G, Jr., Wakefield T, Jacobs L, et al. Renal artery aneurysms: a 35-year clinical experience with 252 aneurysms in 168 patients. *Ann Surg* 2001; 234:454-462; discussion 462-453.

Hoi Y, Woodward S, Kim M, Taulbee D, Meng H. Validation of CFD simulations of cerebral aneurysms with implication of geometric variations. *J Biomech Eng* 2006; 128:844-851.

Hubert J, Jr., Pairolero P, Kazmier F. Solitary renal artery aneurysm. *Surgery* 1980; 88:557-565.

Hupp T, Allenberg J, Post K, Roeren T, Meier M, Clorius J. Renal artery aneurysm: surgical indications and results. *Eur J Vasc Surg* 1992; 6:477-486.

Jaff M. *Endovascular Therapy for Atherosclerotic Renal Artery Stenosis: Present and Future*. New York: Futura Publishing, 2001.

Kameneva MV, Burgreen GW, Kono K, Repko B, Antaki JF, Umezo M. Effects of turbulent stresses upon mechanical hemolysis: experimental and computational analysis. *ASAIO J.* 50: 418-423, 2004.

Kang YJ, Kim MG, Son KH, Lim CH, Son HS, Yoon SY, Kwon HS, Yang S. Experimental investigation of pulsatility effect on the deformability and hemolysis of blood cells. *Artif. Organs* 34: E103-E109, 2010.

Kataoka H, Kimura Y, Fujita H, Takatani S. Influence of radial clearance and rotor motion to hemolysis in a journal bearing of a centrifugal blood pump. *Artif. Organs* 30: 841-854, 2006.

Kem D, Lyons D, Wenzl J, Halverstadt D, Yu X. Renin-dependent hypertension caused by nonfocal stenotic aberrant renal arteries: proof of a new syndrome. *Hypertens* 2005; 46:380-385.

Keshaviah P. *Hemolysis in the accelerated flow region of an abrupt contraction*. Doctoral Dissertation. University of Minnesota. 1974.

Kim NJ, Diao C, Ahn KH, Lee SJ, Kameneva MV, Antaki JF. Parametric study of blade tip clearance, flow rate, and impeller speed on blood damage in rotary blood pump. *Artif. Organs* 33: 468 – 474, 2009.

Lee S, Yim Y, Ahn K, S Lee. Extensional flow-based assessment of red blood cell deformability using hyperbolic converging microchannel. *Biomed. Microdevices* 11: 1021-1027, 2009.

Leverett LB, Hellums JD, Alfrey CP, Lynch EC. Red blood cell damage by shear stress. *Biophys. J.* 12: 257-273, 1972.

Liang F, R Yamaguchi, Liu H. Fluid Dynamics in Normal and Stenosed Human Renal Arteries: an Experimental and Computational Study. *J Biomech Sci Eng* 2006; 1:171-182.

Lokhandwalla M, Sturtevant B. Mechanical haemolysis in shock wave lithotripsy (SWL): 1. Analysis of cell deformation due to SWL flow fields. *Phys. Med. Biol.* 46: 413-437, 2001.

Lumsden A, Salam T, Walton K. Renal artery aneurysm: a report of 28 cases. *Cardiovasc Surg* 1996; 4:185-189.

McGraw L. Blood cell deformability in uniaxial extensional flow. Doctoral Dissertation. Carnegie Mellon University. 1992.

Mitoh A, Yano T, Sekine K, Mitamura Y, Okamoto E, Kim DW, Yozu R, Kawada S. Computational fluid dynamics analysis of an intra-cardiac axial flow pump. *Artif Organs* 27:34-40, 2003.

Mollet M, Godoy-Silva R, Berdugo C, Chalmers J. Computer simulations of the energy dissipation rate in a fluorescence-activated cell sorter: implications to cells. *Biotechnol. Bioeng.* 100: 260-272, 2008.

Nevaril CG, Hellums JD, Alfrey CP, Lynch EC. Physical effects in red blood cell trauma. *AIChE J.* 15(5): 707-711, 1969.

Nguyen K, Clark C, Chancellor T, Papavassiliou DV. Carotid geometry effects on blood flow and on risk for vascular disease. *J Biomech* 2008; 41:11-19.

Paul R, Apel J, Klaus S, Shügner F, Schwindke P, Reul H. Shear stress related blood damage in laminar couette flow. *Artif. Organs* 27(6): 517-529, 2003.

Phillips J. Pathogenesis of hypertension in renal failure: role of the sympathetic nervous system and renal afferents. *Clin Exp Pharmacol Physiol* 2005; 32:415-8.

Polaschegg HD. Red blood cell damage from extracorporeal circulation in hemodialysis. *Semin. Dialysis.* 22: 524-531, 2009.

Serter S, Oran I, Parildar M, Memis A. Fibromuscular dysplasia-related renal artery stenosis associated with aneurysm: successive endovascular therapy. *Cardiovasc Intervent Radiol* 2007; 30:297-299.

Shalman E, Barak C, Dgany E, Noskowitz H, Einav S, Rosenfeld M. Pressure-based simultaneous CFR and FFR measurements: understanding the physiology of a stenosed vessel. *Comput Biol Med* 2001; 31:353-363.

Shojima M, Oshima M, Takagi K, Torii R, Hayakawa M, Katada K, et al. Magnitude and role of wall shear stress on cerebral aneurysm: computational fluid dynamic study of 20 middle cerebral artery aneurysms. *Stroke* 2004; 35:2500-2505.

Simon HA, Dasi LP, Leo HL, Yoganathan AP. Spatio-temporal flow analysis in bileaflet heart valve hinge regions: potential analysis for blood element damage. *Ann. of Biomed. Eng.* 35: 1333-1346, 2007.

Song S, Throckmorton A, Wood H, Antaki J, Olsen D. Computational fluid dynamics prediction of blood damage in a centrifugal pump. *Artif. Organs* 27: 938-941, 2003.

Steinman D. Image-based computational fluid dynamics modeling in realistic arterial geometries. *Ann Biomed Eng* 2002; 30:483-497.

Stewart SFC, Day S, Burgreen GW, Paterson EG, Manning KB, Hariharan P, Deutsch S, Giarra M, Cheek C, Reddy V, Berman MR, Myers MR, Malinauskas RA. Preliminary results of FDA's "Critical Path" project to validate computational fluid dynamics methods used in medical device evaluation. *ASAIO J.* 55: 173, 2009.

Suo J, Oshinski J, Giddens D. Blood flow patterns in the proximal human coronary arteries: relationship to atherosclerotic plaque occurrence. *Mol Cell Biomech* 2008; 5: 9-18.

Sutera SP, Mehrjardi MH. Deformation and fragmentation of human red blood cells in turbulent shear flow. *Biophys. J.* 15: 1-10, 1975.

Taylor C, Hughes T, Zarins C. Finite element modeling of three-dimensional pulsatile flow in the abdominal aorta: relevance to atherosclerosis. *Ann Biomed Eng* 1998; 26:975-987.

Tham G, Ekelund L, Herrlin K, Lindstedt E, Olin T, Bergentz S. Renal artery aneurysms. Natural history and prognosis. *Ann Surg* 1983; 197:348-352.

Wentzel J, Gijzen F, Schuurbiers J, Krams R, Serruys P, De Feyter P, Slager C. Geometry guided data averaging enables the interpretation of shear stress related plaque development in human coronary arteries. *J Biomech* 2005; 38: 1551 – 1555.

White C, Olin, J. Diagnosis and management of atherosclerotic renal artery stenosis: improving patient selection and outcomes. *Nat Clin Pract Cardiovasc Med* 2009; 6: 176-190.

Yano T, Sekine K, Mitoh A, Mitamura Y, Okamoto E, Kim DW, Nishimura I, Murabayashi S, Yozu R. An estimation method of hemolysis within an axial flow blood pump by computational fluid dynamics analysis. *Artif Organs* 27:920-925, 2003.

Yeleswarapu KK, Antaki JF, Kameneva MV, Rajagopal KR. A mathematical model for shear-induced hemolysis. *Artif Organs* 19:576-582, 1995.

Yim P, Cebra J, Weaver A, Lutz R, Soto O, Vasbinder B, Ho V, Choyke P. Estimation of the differential pressure at renal artery stenoses. *Magn Reson Med* 2004; 51:969-977.

Young D. Fluid Mechanics of Arterial Stenoses. *J Biomech Eng* 1979; 101:185-196.

Zhang Y, Zhan Z, Gui XM, Sun HS, Zhang H, Zheng Z, Zhou JY, Zhu XD, GR Li, Hu SS, Jin DH. Design optimization of an axial blood pump with computational fluid dynamics. *ASAIO J.* 54:150-155, 2008.

Zhao R, Antaki JF, Naik T, Bachman TN, Kameneva MV, Wu ZJ. Microscopic investigation of erythrocyte deformation dynamics. *Biorheol* 43: 747-765, 2006.

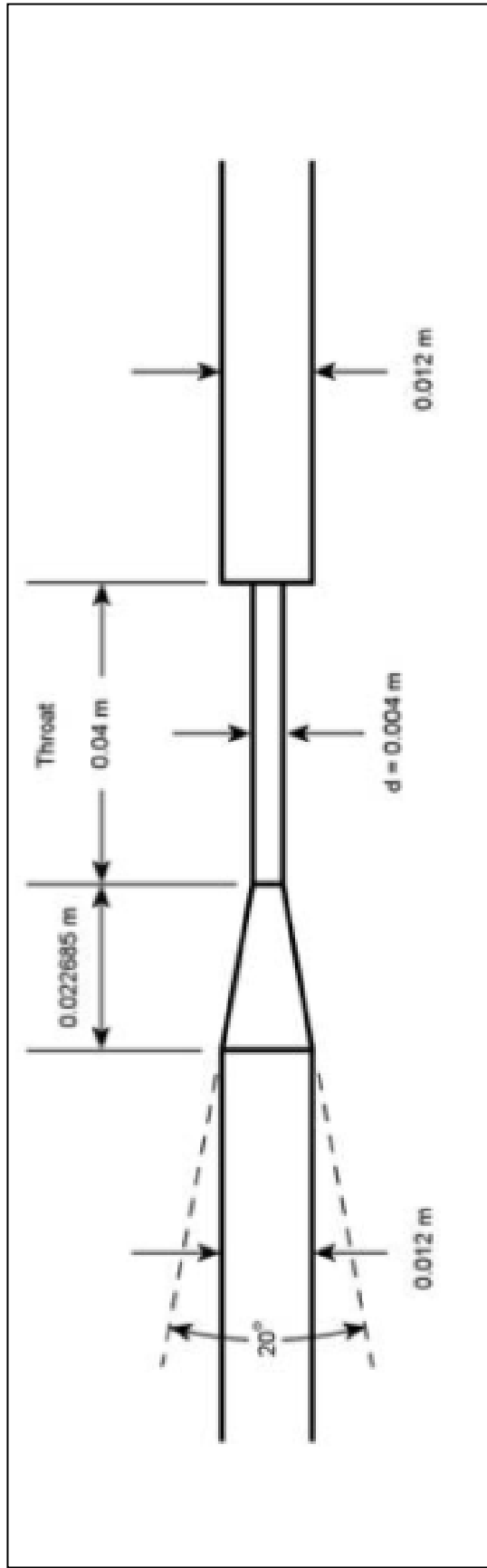


Figure 1.1 Nozzle Geometry Specified by FDA Critical Path Initiative. The geometry was designed to include features relevant to medical devices, and to be modeled under conditions thought to produce hemolysis.

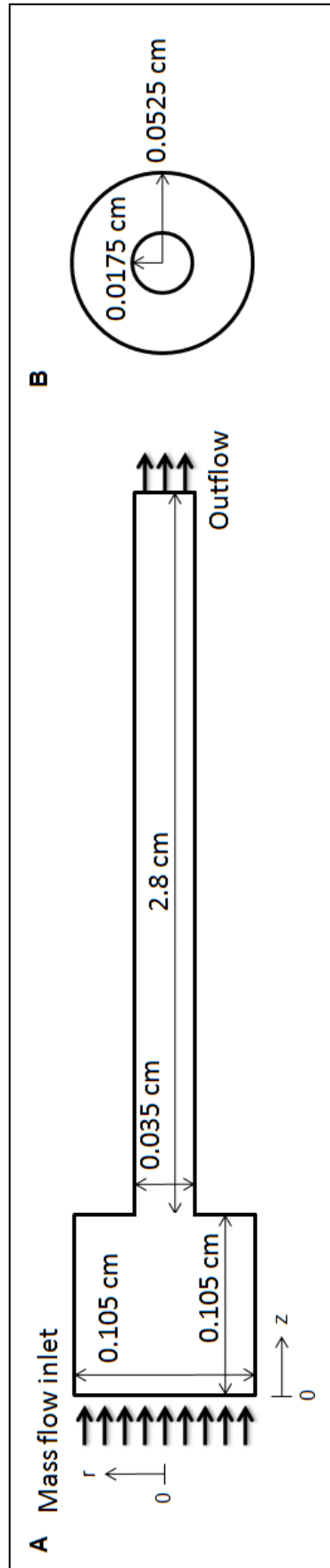


Figure 1.2. Schematic of simulation domain for a 3:1 contraction from Keshaviah's work. A) Axial view of constriction geometry. B) Cross sectional view of constriction. The average number of nodes for all simulated capillaries was approximately 710,000 with an average computational cell size at the entrance of the capillary on the order of magnitude of $5 \times 5 \mu\text{m}$.

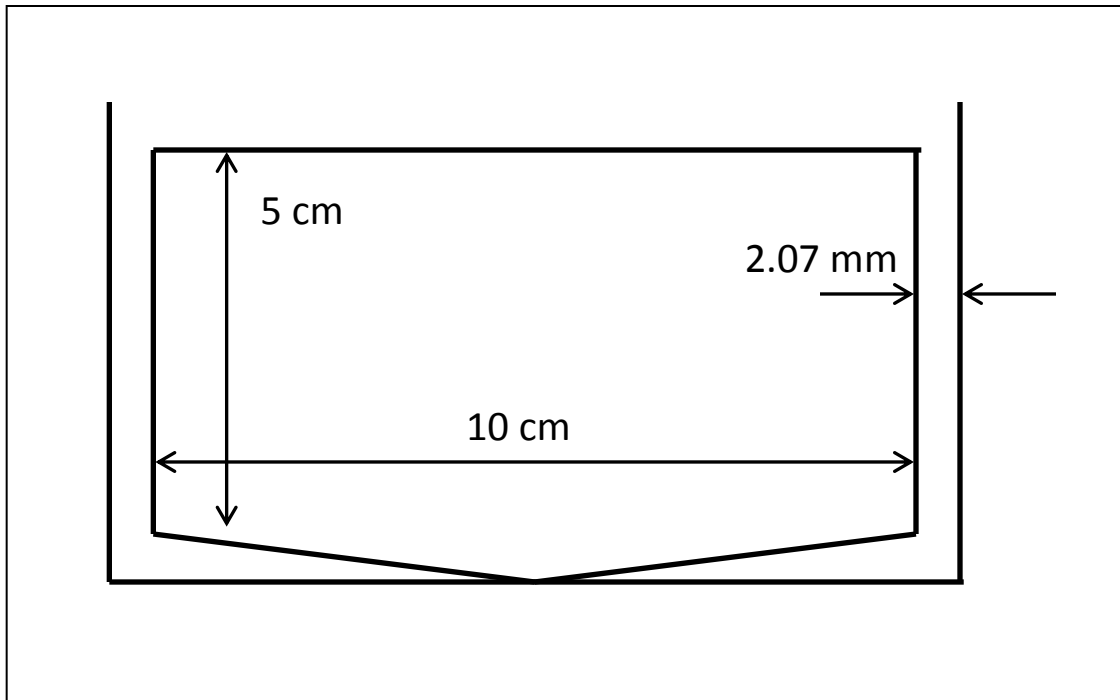


Figure 1.3. Sutera et al.'s turbulent Couette viscometer geometry. For simulation simplicity, only 1/16th of the viscometer geometry was modeled.

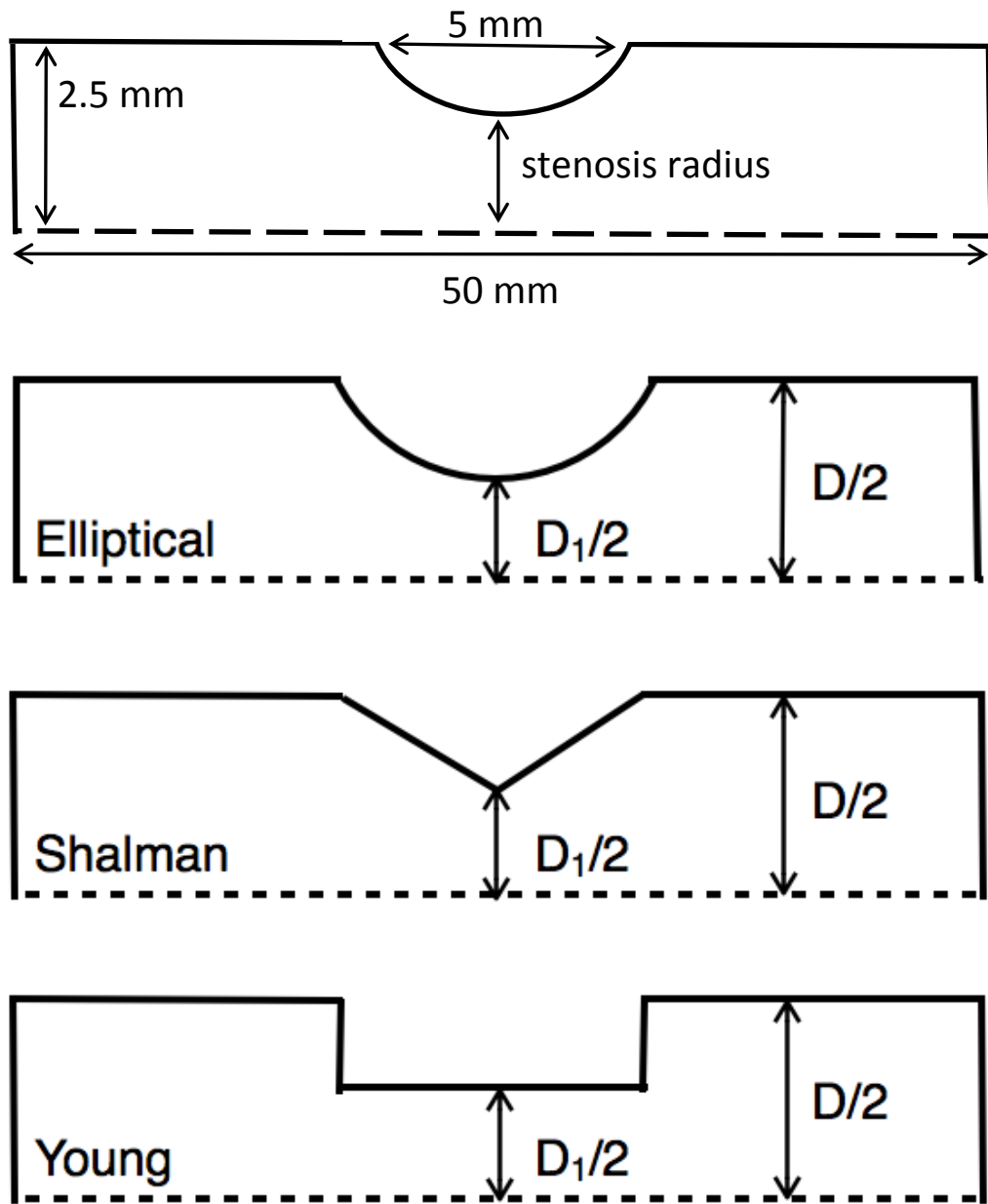


Figure 1.4. Stenosis geometries. A) Characteristic stenosis dimensions. B) Characteristic shape of elliptical stenosis. C) Characteristic shape of Shalman “conical” type stenosis. D) Characteristic shape of Young “blunt” type stenosis.

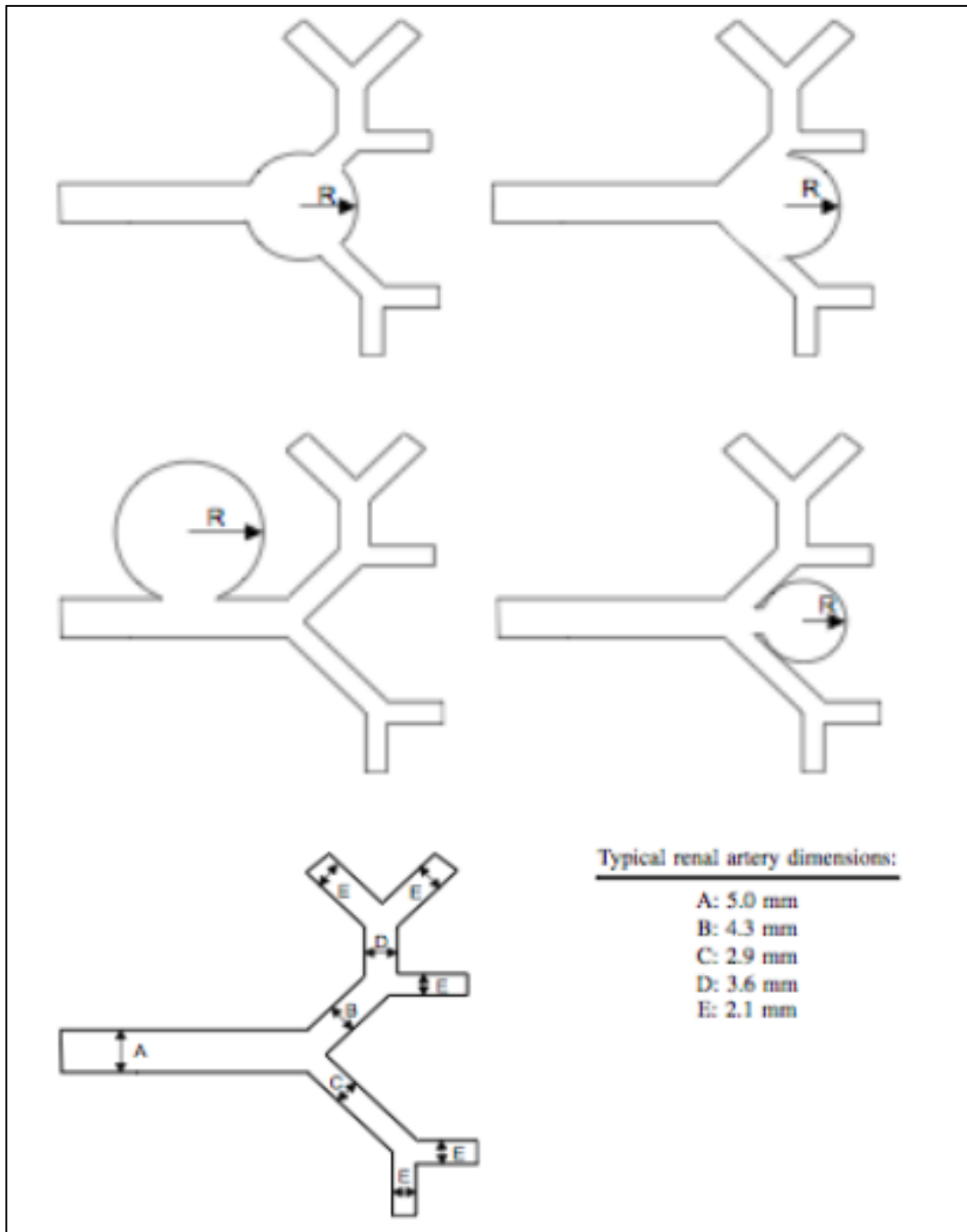


Figure 1.5. Renal artery aneurysm geometries. A) Fusiform aneurysm of the main branch. B) Wide-necked, saccular aneurysm of the main branch. C) Saccular aneurysm of the main artery. D) Saccular aneurysm of the main branch. D) Characteristic diameters of the branches of the renal artery modeled in 2D.

Abnormality	Geometry	Dimensions	Hypertension	Treatment	Outcome
168 cases: 73% with hypertension (Henke, 2001)	79% Saccular, 21% Fusiform	Average size: 1.3-1.5 cm	73%	Aneurysmectomy, angioplastic renal artery closure, segmental renal artery reimplantation, aneurysmectomy and renal artery bypass, nephrectomy	Of 40 patients with follow up, 60% had significant decline in blood pressure
67 cases: 69% with hypertension (Hubert, 1980)	Saccular, Fusiform, Dissecting	0.3 – 4 cm (mean 1.5)	69%	Surgical therapy in 5 patients	Improved hypertension in 1 surgical patient
28 cases: 79% with hypertension (Lumsden, 1996)	80% Saccular	0.5 - 8 cm (mean 2.1)	79%	Surgical therapy in 10 patients, aorto renal bypass, aneurysm excision	Not given
21 cases: 100% with hypertension (Bastounis, 1998)	62% Saccular, 24% Fusiform, 14% Dissect.	2 – 6.5 cm	100%	Resection with either closure using a venous patch or end-to-end anastomosis, aorto-renal bypass	Cured hypertension: 67% Improved: 19%
19 cases: 89% with hypertension (Hupp, 1992)	Saccular, Fusiform	0.5-16.5 cm	89%	Aorto-renal bypass, aneurysm resection, embolisation	Cured hypertension: 41% Improved: 59%
Aneurysm of right renal artery (Degertekin, 2006)	Saccular	35x33x31 mm	Yes	Stent-graft	Controlled hypertension with 1 anti-hypertensive
Two severe stenoses and aneurysm (Bui, 1995)	Saccular	1.5 x 1 cm	Yes	Percutaneous placement of stent-graft	Normotensive
Aneurysm immediately following 90% stenosis (Bisschops, 2001)	Bilobed	Large: 1cm Small: 0.4 cm	Yes	Stent-graft	Normotensive
Aneurysm of right renal artery (Tan, 2001)	Saccular	3 cm	Yes	Covered stent (loss of one renal artery branch)	Normotensive with 1 anti-hypertensive
Aneurysm of left renal artery (Pershad, 2004)	Saccular	1.2-1.3 cm	Yes	Covered stent (loss of one renal artery branch)	Not given
Aneurysm of left renal artery (Castillo, 2006)	Saccular	2.5 cm	Yes	Laparoscopic vascular reconstruction	Controlled hypertension with 1 anti-hypertensive
Aneurysm of right renal artery following 90% stenosis (Serter, 2007)	Saccular	Not given (small)	Yes	Transluminal angioplasty and coil embolization	Normotensive

Table 1.1. Large center and case studies that indicate a relationship between renal artery aneurysms and renovascular hypertension. These cases indicate that renal artery aneurysms are related to a curable form of renovascular hypertension.

CHAPTER 2: COMPUTATIONAL METHODS

2.1 General Procedure

The simulations completed in both Fluent and COMSOL were performed using a dual Pentium Xeon PC. Simulation time varied from a few seconds for the 2D simulations, to a week for the 3D FSI simulations, depending on the mesh density and required convergence criteria.

While the details of the modeling varied depending on the methods used and the situation being modeled, in general the set up was similar for all cases. Initially, a geometry representative of either the desired biology or the desired experimental set up was created (using either Gambit or the built-in geometry creation environment in COMSOL). This computational domain was then discretized into a mesh. The type of boundary conditions to be used were specified for the domain, and, in the case of the Fluent simulations, the discretized mesh was imported from Gambit into Fluent. For those cases that required turbulence modeling, the k- ϵ turbulence model was specified. The specific boundary conditions were set (for example, the magnitude of the mass flow rate of fluid entering the domain).

When setting up the solution parameters, the discretization method was specified as well as the convergence criteria. For all Fluent simulations, either the first or second order upwind discretization scheme was used. Convergence was considered to be achieved when the residuals of all equations were below a specified level. The final step before simulation was initialization, where initial estimates of key parameters were specified. The simulation was then begun, the residuals were monitored, and once they reached the specified convergence criteria, the simulation was concluded.

2.2 Modeling Turbulent Flow

The standard k-ε turbulence model in Fluent is a semi-empirical model derived from transport equations for the turbulence kinetic energy and the dissipation rate of turbulent kinetic energy. The turbulence kinetic energy, $k = 1/2 \overline{u_i u_i}$, and the dissipation

rate of turbulent kinetic energy, $\varepsilon = \nu \left(\overline{\frac{\partial u_i}{\partial x_j} \frac{\partial u_i}{\partial x_j}} + \overline{\frac{\partial u_i}{\partial x_j} \frac{\partial u_j}{\partial x_i}} \right)$, are determined using the

following equations:

$$\frac{\partial}{\partial t} (\rho k) + \frac{\partial}{\partial x_i} (\rho k u_i) = \frac{\partial}{\partial x_i} \left[\left(\mu + \frac{\mu_t}{\sigma_k} \right) \frac{\partial k}{\partial x_j} \right] + G_k - \rho \varepsilon + S_k \quad (2.1)$$

$$\frac{\partial}{\partial t} (\rho \varepsilon) + \frac{\partial}{\partial x_i} (\rho \varepsilon u_i) = \frac{\partial}{\partial x_i} \left[\left(\mu + \frac{\mu_t}{\sigma_\varepsilon} \right) \frac{\partial \varepsilon}{\partial x_j} \right] + C_{1\varepsilon} \frac{\varepsilon}{k} (G_k) - C_{2\varepsilon} \rho \frac{\varepsilon^2}{k} + S_\varepsilon \quad (2.2)$$

$$\mu_t = \rho C_\mu \frac{k^2}{\varepsilon} \quad (2.3)$$

where u_i is the fluctuation of velocity in the i direction, with the overbar denoting time average; ν is kinematic viscosity; ρ is density; μ is viscosity; μ_t is turbulent viscosity; G_k is the generation of turbulence kinetic energy due to mean velocity gradients; the model constants are $C_{1\varepsilon} = 1.44$, $C_{2\varepsilon} = 1.92$, and $C_\mu = 0.09$, and the turbulent Prandtl numbers for k and ε are $\sigma_k = 1.0$ and $\sigma_\varepsilon = 1.3$ (ANSYS Fluent 12 Theory Guide).

For the capillary tube, stenosis, and aneurysm simulations, the k-ε turbulence model was used for simulations where the Reynolds number was above a critical Reynolds number. The Reynolds number distinguishes laminar ($Re < 2000$), transition ($Re 2000 - 2500$) and turbulent flows ($Re > 2500$), and is generally given as:

$$Re = \frac{\rho D v}{\mu} \quad (2.4)$$

for flow in a tube where v is the bulk velocity in the tube, D is the tube diameter, ρ is the fluid density, and μ is the fluid viscosity. For the renal artery stenosis simulations, this critical Reynolds number was determined by comparing the Reynolds number in the unobstructed artery to data from Azuma, et al., which gives the critical Reynolds number for an axisymmetric, streamlined stenosis as a function of percent area reduction (Azuma, 1976). For all simulations where the Reynolds number did not reach this critical value, the simulation was performed using the laminar solver.

For flow such as in the Couette viscometer, with the inner cylinder rotating and the outer cylinder stationary, turbulence is determined by a dimensionless parameter called the Taylor number:

$$Ta = \frac{\Omega_i R_i^{1/2} h^{3/2}}{\nu} \quad (2.5)$$

where Ω_i is the angular speed of the inner cylinder, R_i is the radius of the inner cylinder, h is the gap width, and ν the kinematic viscosity of the fluid (Sutera, 1975). The Taylor number describes the various flow regimes that can occur in this type of viscometer, including Taylor vortices, wavy Taylor vortices, modulated wavy vortices, and turbulent Taylor vortices. Taylor vortices are large, counter-rotating toroidal vortices, stacked vertically in the z -direction in the flow (Bird, 2007). For this definition of the Taylor number, the flow is known to become turbulent at a Taylor number greater than 400. For all of the rotational rates of interest simulated here, the flow was in the turbulent Taylor vortex regime, and the realizable k - Σ turbulence model was used. The realizable k - Σ model uses a similar equation for k (i.e. equation 2.1) to the standard k - Σ model, but the equation for Σ is different:

$$\frac{\partial}{\partial t}(\rho\varepsilon) + \frac{\partial}{\partial x_i}(\rho\varepsilon u_i) = \frac{\partial}{\partial x_j} \left[\left(\mu + \frac{\mu_t}{\sigma_\varepsilon} \right) \frac{\partial \varepsilon}{\partial x_j} \right] + \rho C_1 S \varepsilon - \rho C_2 \frac{\varepsilon^2}{k + \sqrt{\nu \varepsilon}} + S_\varepsilon \quad (2.6)$$

where: $C_1 = \max \left[0.43, \frac{\eta}{\eta + 5} \right]$, $\eta = S \frac{k}{\varepsilon}$, $S = \sqrt{2 S_{ij} S_{ij}}$ and $C_{1\varepsilon}=1.44$, $C_2=1.9$, $\sigma_k=1.0$ and $\sigma_\varepsilon=1.2$. (ANSYS Fluent 12 Theory Guide).

2.3 Modeling Fluid Structure Interaction

For finite element analysis, COMSOL uses a weighted residual formulation. The software discretizes the solution domain into finite elements and assumes a shape function representing the physical behavior of an element, developing an approximate solution to the governing differential equations. COMSOL uses a weak finite element formulation, the Galerkin finite element method, to solve the set of ordinary differential equations obtained from discretization of the domain.

COMSOL uses a partitioned approach for solving a fluid structure interaction problem, meaning the equations that govern the fluid flow and the displacement of the solid are solved separately. The velocities and the forces at the boundary between the fluid and the solid are matched, thus coupling the solid displacement and the fluid flow. The software iteratively solves the Navier-Stokes equations of motion, a complex set of nonlinear partial differential equations, for the blood flowing in the artery, and Hooke's Law for the displacement of the arterial wall.

Hooke's law states generally that for linear elastic materials, strain is directly proportional to stress:

$$\sigma = E\varepsilon \quad (2.7)$$

where σ is tensile stress, E is the constant of proportionality called Young's modulus and ϵ is the strain. When working in three dimensions, an elasticity tensor, characterized by the Young's modulus and the Poisson's ratio for an isotropic material, is used to relate the stress tensor and the strain tensor. The Young's modulus is a material property that describes the stiffness of an elastic material. It is the ratio of stress to strain and can be determined for a material experimentally. The Poisson's ratio is a material characteristic related to the expansion or contraction of a particular material due to compression or stretching, respectively. It is described as the ratio of contraction to extension (or transverse strain to axial strain) occurring when a material is stretched. A perfectly incompressible material would have a Young's modulus of 0.5. For this work, the material is also assumed to have a linear strain-displacement relationship.

For fluid structure interaction studies, COMSOL uses an Arbitrary Lagrangian-Eulerian (ALE) formulation for the mesh, which is a combination of the fully stationary Eulerian form, typically used for the simulation of fluids, and the Lagrangian form, a type of mesh typically used for the simulation of solids, which is allowed to move with the solid domain. In the ALE formulation the mesh can move arbitrarily to optimize the shape of the elements in the mesh. The spatial coordinates of the mesh nodes at a given time after the initial configuration are determined using a mesh smoothing function that relates the spatial coordinate system to the coordinates of the mesh nodes attached to the material, which may have moved depending on the problem boundary conditions. In this work, Winslow smoothing was used to determine the spatial coordinates of the deformed mesh (COMSOL User's Guide).

2.4 Computational Domain

2.4.1 Grid Generation

For both the finite volume (Fluent) and the finite element (COMSOL) techniques used in this work, the computational domain must be discretized into small volumes or elements over which the calculations are made. It is important that the elements not be highly skewed (i.e. large aspect ratios) in order to obtain a stable solution. For all two-dimensional simulations a quadrilateral mesh was used. For 3D simulations conducted in Fluent, a hexahedral mesh was used and for all simulations performed in COMSOL a tetrahedral mesh was used. Examples of the hexahedral mesh used in 3D Fluent simulations and the tetrahedral mesh used in COMSOL are shown in Figures 2.1 and 2.2.

For the meshes used in Fluent, the initial mesh was created using a uniform element size, then subsequently refined in regions of high velocity gradient for increased accuracy. For most meshes used in COMSOL, the program generated a non-uniform mesh with smaller elements concentrated near fluid-solid boundaries and in regions with small geometric features. Each type of simulation performed required a different grid, so the details of each of these grids are discussed in their respective chapters.

2.4.2 Boundary Conditions

2.4.2.1 Fluent

For the work completed in Fluent, either a velocity inlet or a mass flow inlet was specified. A velocity inlet boundary condition is used to set the flow velocity at flow inlets. When a velocity inlet boundary condition is set, the total pressure is not fixed but will adjust in response to the calculated static pressure to the value required to provide the specified velocity. In this work, two techniques were used to describe the velocity at

the inlet. The first, and most simple, method was to set the magnitude of the velocity normal to the boundary, which created a flat, constant velocity at the inlet. The second was to use a user defined function to describe the velocity at the inlet. For the two-dimensional studies, simulations were completed with two types of user defined velocities: a parabolic inlet velocity in one case, and a time-dependent pulsatile velocity in the other. Using the velocity given, Fluent calculates the mass flow into the computational domain and the flux of momentum through the inlet.

Similar to the velocity inlet, the mass flow boundary condition can be used to set the mass flow rate at the inlet, allowing the total pressure to adjust in order to meet the requirements of the specified inlet condition. In this work, the mass flow was specified normal to the boundary. For inlets specified using a mass flow boundary condition, the software calculates a velocity for each face on the inlet, and this velocity is used to calculate the flux of momentum into the computational domain.

Two types of outlet boundary conditions were used: a pressure outlet condition and an outflow outlet condition. For a pressure outlet condition, the static (gauge) pressure at the outlet boundary is specified. During computation, Fluent uses the given static pressure at the outlet boundary and extrapolates the other flow conditions from the interior of the domain. An outflow boundary condition can be used when the precise details of the exit flow are unknown prior to simulation. With this outlet boundary type, the only condition specified at the outlet is the percentage of flow through the boundary, and the specific flow conditions at the outlet are extrapolated from the interior of the domain.

A periodic boundary condition can be used when the geometry of interest and the anticipated flow solution have a periodically repeating character. That is, the flow across two planes in the geometry is identical. For the turbulent couette viscometer simulations, rotationally periodic boundaries were used so that the size of the computational domain could be reduced. For periodic boundary conditions, Fluent assumes that the flow at a periodic boundary is the same as that in the cells adjacent to its matching periodic boundary.

Symmetry boundary conditions can be used when the geometry of interest and the anticipated flow solution display bilateral symmetry. During computation, Fluent assumes zero flux of all values across the symmetry plane. There is no normal velocity and are no normal gradients of any variable at a symmetry boundary. For axisymmetric problems performed in 2D, an axis boundary condition is defined as the centerline in the axisymmetric geometry. No flow conditions are defined at an axis boundary condition.

All boundaries not specified as inlet, outlet, periodic or symmetric boundaries are considered wall boundaries. For all simulations in this work, a no-slip boundary condition was used at the walls, meaning the velocity of the wall and the fluid at the wall is the same. For the turbulent couette viscometer simulations, a moving wall was specified, wherein the angular velocity of the wall was set.

2.4.2.2 COMSOL

For all simulations conducted in COMSOL, a velocity inlet was used to specify the flow into the domain. Similar to the analogous boundary condition in Fluent, a constant velocity normal to the inflow boundary is specified at the inlet. A pressure outlet was used for all simulations as well, and is specified by a value for the pressure at

the outlet. A no slip wall condition was applied at all fluid boundaries not specified as an inlet or an outlet. A symmetry boundary was specified at the plane of symmetry in the desired geometry in order to reduce the size of the computational domain.

For the structural mechanics portion of the simulation, a fixed boundary constraint was added. A fixed boundary constrains the displacements in all directions to zero.

In order to couple the fluid and solid mechanics, a fluid-solid interface boundary is defined at all boundaries where the modeled fluid and solid come into contact. This boundary condition defines the fluid load on the solid and the way in which the displacement of the solid affects the fluid velocity. The fluid-solid interface boundary condition specifies that the force and velocity at the fluid-solid boundary are matched for the fluid and the solid.

2.4.3 Mechanical Properties for Fluid Structure Interaction

For the 3D fluid structure interaction simulations that included the arterial wall, specification of the mechanical properties of the artery and aneurysm was necessary. The renal arteries carry approximately 25% of the total cardiac output - approximately 600 ml/min through each artery (Cooney 1976). An arterial wall is typically composed of three layers: the intima, media and adventitia. The intima is the innermost layer and contains the endothelial cells. The media contains the smooth muscle cells, and the adventitia, the outermost layer, is mainly composed of collagen fibers and other substances. The size of these three layers relative to each other varies according to the size of the artery. The renal artery is considered a medium sized artery, with a smaller amount of elastin in the media compared to other larger elastic arteries (Fung 2004). In order to complete the fluid structure interaction simulations successfully, a few

simplifying assumptions were made. First, while it is understood that arterial walls are in fact viscoelastic materials, the arterial and aneurysmal wall were both treated as linear elastic materials in order to simplify computation. Simulations were performed using three different arterial Young's moduli – 1×10^4 , 1×10^5 and 1×10^6 Pa. These values were chosen to represent the evident variation in material properties surrounding aneurysms and to correspond to a range of Young's modulus values from the literature. Most investigators assume that arterial wall tissue is an almost incompressible material, thus the Poisson's ratio for both the artery and the aneurysm was chosen as 0.499 (Balocco 2010). The thickness of the arterial wall was also an important parameter for the model, and a value of 1 mm was chosen for most simulations. This thickness was determined based on other investigators who have estimated arterial wall thickness as approximately 20% of the inner diameter of the vessel (Bazilevs, 2010).

Determining the mechanical properties of the aneurysm wall proved to be more difficult, as very little information on the structure of renal artery aneurysms is reported in the literature. Due to this, data from cerebral aneurysms was used because of its relative abundance and the idea that cerebral aneurysms (and the arteries from which they grow) more closely resemble renal arteries and renal artery aneurysms than other highly reported aneurysms, such as abdominal aortic aneurysm. Cerebral aneurysms are similar in size to renal artery aneurysms, ranging from a few to tens of millimeters (Zhao, 2011) while renal artery aneurysms average 15 mm in size (Henke, 2001). Many reports in the literature state that the vessel wall is extremely thinned in an aneurysm (Zhao 2011; Ferguson, 1972), with ranges reported from 20 – 500 microns (Challa, 2007; Balocco, 2010; Kyriacou, 1996). As such, most simulations were performed with an aneurysm

wall of 0.5 mm (the top of the range), while some simulations with a thinner wall were performed for comparison. These estimates of aneurysm wall thickness are difficult to verify – there is currently no method to measure aneurysm wall thickness *in vivo* (Zhao, 2011; Balocco, 2010), so measurements are typically made after aneurysm rupture, in which case the aneurysm wall is thought to be thinned even more (Balocco, 2010; Kyraicou, 1996), with the thinnest portion of the wall occurring at the rupture site. The Young's modulus of aneurysms compared to the arteries from which they grew are thought to be stiffer (Ferguson, 1972; Humphrey, 1995), however, some investigators have shown that these properties vary throughout the aneurysm (Balocco, 2010; Chall, 2007). Because of these factors, aneurysms were simulated with Young's moduli of 1×10^5 , 1×10^6 and 1×10^7 Pa, with some simulations incorporating a varying Young's modulus over the aneurysm sac.

Anisotropy is a well know characteristic of arterial wall tissue (Fung, 2004), with the mechanical properties of the arterial wall usually being characterized as transversely orthotropic, with different properties in the axial and circumferential directions (Humphrey, 1995). The values of the circumferential and axial Young's moduli are difficult to determine, and these measurements, to the best of the author's knowledge, do not exist in the literature for renal arteries. As such, in order to investigate the effect of orthotropicity, simulations were performed where the axial Young's modulus was an order of magnitude lower than the circumferential, and vice versa. These values of the axial and circumferential Young's moduli are consistent with other assumed differences in magnitude used in other computational structural mechanics investigations of cerebral aneurysms (Kyriacou, 1996). Anisotropy may not be as important a characteristic for the

aneurysm wall as for the arterial wall, as it is known that the collagenous tissue of the aneurysm wall remodels in response to the changing stresses in the wall (Zhao, 2011) and some investigators have speculated that the aneurysm wall would not be expected to be more anisotropic than the artery from which it grew because as the aneurysm deforms from the more cylindrical shape of the artery to the more spherical shape of the aneurysm sac the stresses in the spherical shape would be expected to be more uniform (Kyriacou, 1996). In this case, through remodeling, the aneurysm wall might even be expected to become more isotropic, or differently anisotropic.

2.5 Nomenclature

$C_{1\varepsilon}$ - 1.44

C_2 - 1.9

$C_{2\varepsilon}$ - 1.92

C_μ - 0.09

G_k – generation of turbulence kinetic energy due to mean velocity gradients

k – turbulence kinetic energy

u_i – fluctuation of velocity in the i direction

S – modulus of the mean rate-of-strain tensor

ε - dissipation rate of turbulent kinetic energy

μ - viscosity

μ_t – turbulent viscosity

ν - kinematic viscosity

ρ - density

σ_k – turbulent Prandtl number for $k = 1.0$

σ_ε – turbulent Prandtl number for $\varepsilon = 1.3$ for standard k - ε , 1.2 for realizable k - ε

2.6 References

"4.4.1 Standard k-e Model." *ANSYS Fluent 12.0 Theory Guide*. ANSYS, Inc., 23 Jan. 2009. Web. 30 Nov. 2009.

Azuma T, Fukushima, T. Flow Patterns in Stenotic Blood Vessel Models. *Biorheol* 1976; 13: 337-355.

Balocco S, Camara O, Vivas E, Sola T, Guimaraens L, Gratama van Andel H, Majoie C, Pozo J, Bijmens B, Frangi A. Feasibility of estimating regional mechanical properties of cerebral aneurysms in vivo. *Med Phys* 37(4): 2010: 1689-1706.

Bazilevs Y, Hsu MC, Zhang Y, Wang W, Kvamsdal T, Hentschel S, Isaksen JG. Computational vascular fluid-structure interaction: methodology and application to cerebral aneurysms. *Biomech Model Mechanobiol* 2010; 9: 481-498.

Challa V, Han HC. Spatial variations in wall thickness, material stiffness and initial shape affect wall stress and shape of intracranial aneurysms. *Neurol Res* 2007; 29: 569-577.

Ferguson GC. (1972). "Physical factors in the initiation, growth, and rupture of human intracranial saccular aneurysms." *J Neurosurg* 37: 666-677.

Fung YC. (2004). Biomechanics: Mechanical Properties of Living Tissues. New York, Springer.

Humphrey JD. Critical reviews in biomedical engineering. *Mechanics of the arterial wall: review and directions*. 1995.

Kyriacou SK, Humphrey JD. Influence of size, shape and properties on the mechanics of axisymmetric saccular aneurysms. *J Biomech* 1996; 29: 1015-1022.

Zhao X, Raghavan M, Lu J. Identifying heterogeneous anisotropic properties in cerebral aneurysms: a pointwise approach. *Biomech Model Mechanobiol* 2011; 10: 177-189.

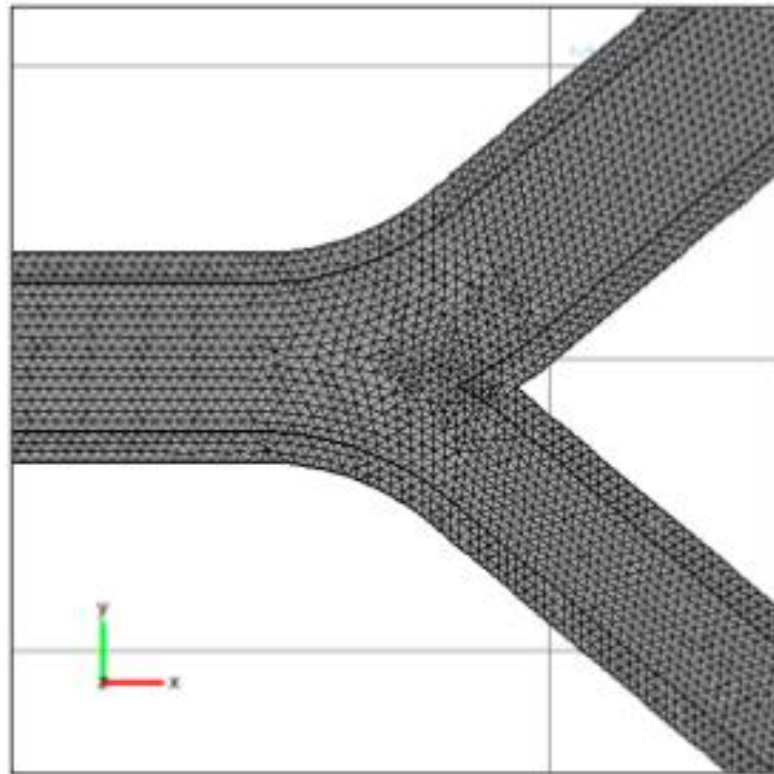
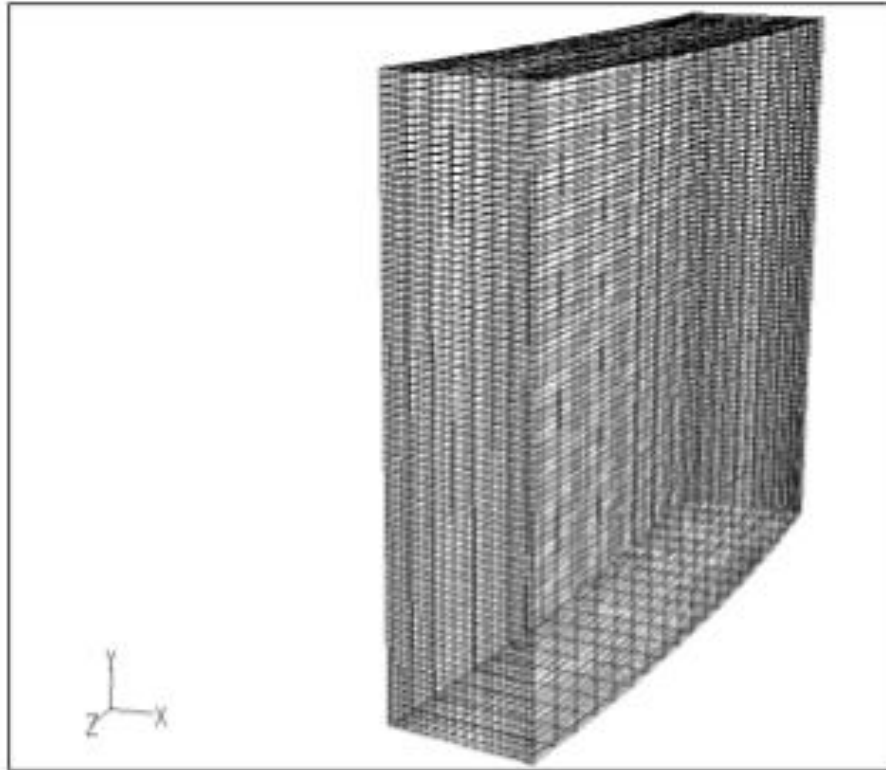


Figure 2.1. Example 3D meshes. A) An example hexahedral mesh used in 3D Fluent simulations. B) An example tetrahedral mesh used in 3D COMSOL simulations.

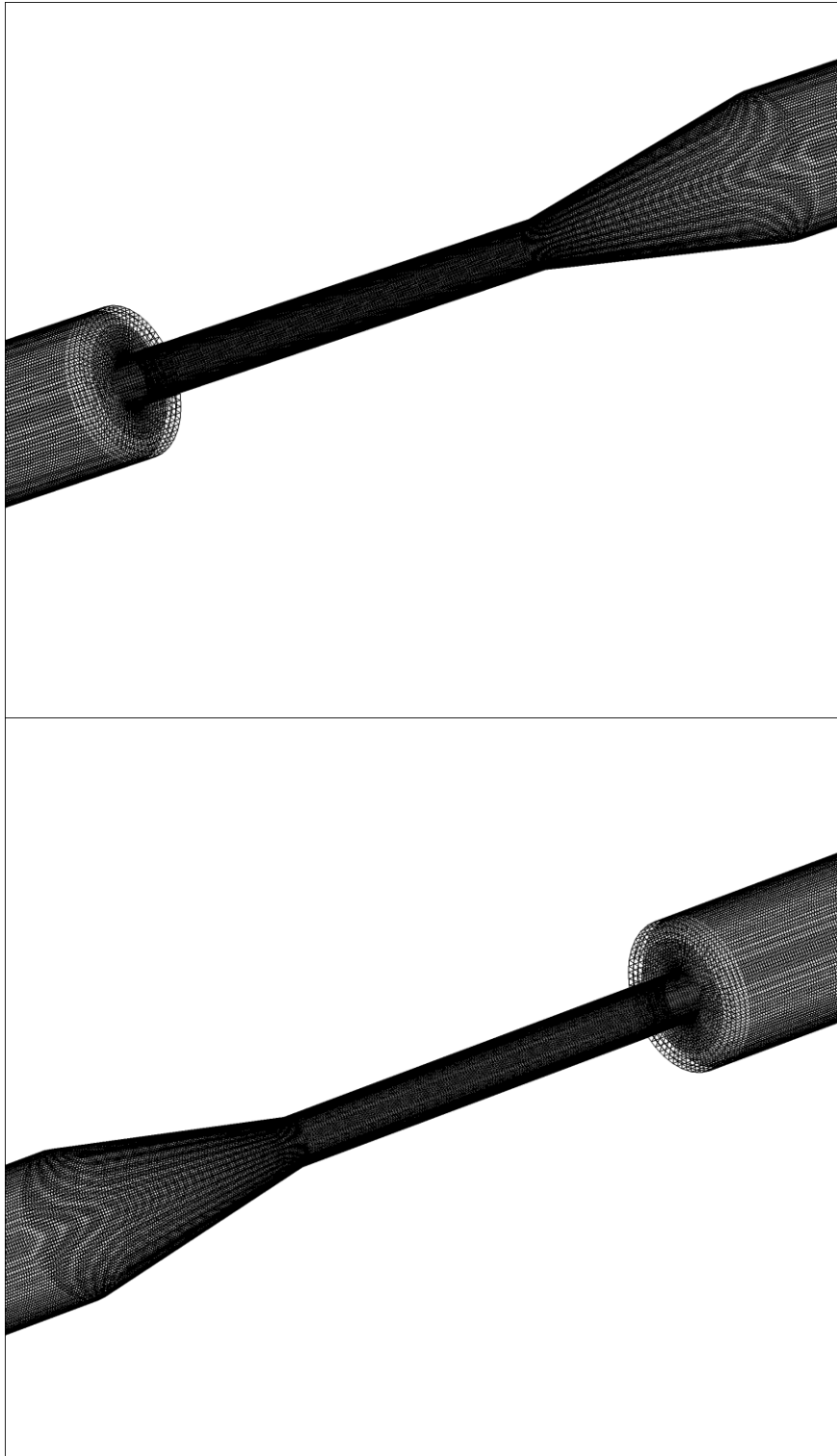


Figure 2.2. Example hexahedral mesh used in 3D Fluent simulations.

CHAPTER 3: HEMOLYSIS ESTIMATION

3.1 Introduction to Hemolysis Simulations

As mentioned previously, in this study of hemolysis three different types of simulations were undertaken in order to investigate the effects of different types of flow on the stresses applied to RBCs. Initially, this portion of the project was motivated by the announcement of the FDA Critical Path Initiative, which had the goal to “accelerate the safety assessment of medical devices in the preclinical stage, with particular attention paid to blood damage, and to standardize CFD techniques for such use.” This collaborative study asked groups around the nation to perform CFD studies using a standardized nozzle geometry, and report back such results as the velocities, stresses present, and estimates of hemolysis. This call to contribute to the development of better CFD practices and hemolysis estimations from CFD by the FDA underscored the lack of standardized simulation models that have been validated with experimental results in this area, and, in addition to the FDA model, prompted further study with the two subsequent models. In order to continue the study of hemolysis in laminar flow, the experimental work of Keshaviah in glass capillary tubes was reproduced computationally (Keshaviah, 1974). Because of Keshaviah’s conclusion that entrance effects dominated the damage to red blood cells, this portion of the work focused on determining which features of the flow were most consistently related to the entrance of the capillary. Finally, to study the effects of turbulence on flow related cellular damage, the turbulent Couette viscometer work of Suter et al. (Sutera, 1975), where cells were exposed to stress for five minutes, was reproduced using a three dimensional model.

It has been shown that the forces associated with blood flow cause hemolysis. From basic fluid mechanics it is known that these forces will be high near the wall and will decrease toward the centerline in the capillary tube model. As such, our approach for the capillary simulations was an “all or nothing” assumption in which there exists a hemolysis zone near the wall of the capillary, where the higher stresses existed, and a core region where cells passed without overt cell damage (Figure 3.1A). In this conceptualization, all cells and only cells in the hemolysis zone experience failure of the cell membrane. The boundary between these two regions was determined so that the fraction of the volumetric flow rate passing through the hemolysis zone corresponded to the observed percent hemolysis reported by Keshaviah. Thus, the spatial location of the *threshold streamline* or pathline varied with experimental conditions (e.g., an experiment that resulted in more hemolysis would have a larger hemolysis zone) while stresses at the boundary between the hemolysis and hemolysis-free regions would presumably be similar in all cases. Figure 3.1B is an illustration of the stress profile that a cell traveling along the threshold streamline would experience – a constant low shear stress while traveling through the large chamber, followed by a sharp increase in stress over a period of microseconds as the flow is constricted to enter the capillary, and finally a constant stress while the cell travels through the capillary. In order to analyze the flow results for the effects of the flow-induced stresses, the shear stress and the extensional components of the stress tensor were calculated for blood treated as a Newtonian fluid. The shear stress is given by (Bird, 2007):

$$\tau_{rz} = -\mu \left(\frac{\partial v_r}{\partial z} + \frac{\partial v_z}{\partial r} \right) \quad (3.1)$$

where μ is the dynamic viscosity of blood, v_r is the radial velocity and v_z is the axial velocity. The radial and axial directions are shown in Fig. 1.2A. The equations for the extensional components of the stress tensor are (Bird, 2007):

$$\tau_{rr} = -\mu \left(2 \frac{\partial v_r}{\partial r} \right) \quad (3.2)$$

$$\tau_{zz} = -\mu \left(2 \frac{\partial v_z}{\partial z} \right) \quad (3.3)$$

These variables were calculated in the entire flow domain as well as along a threshold streamline that originated at the inlet of the flow field.

A similar “all-or-nothing” concept was used in the analysis of the turbulent Couette viscometer results. For this set-up, the percent of the fluid volume corresponding to the percent hemolysis was isolated by an isosurface of the parameter of interest and an attempt to find a threshold value of the investigated parameters on this surface was made. In addition to investigating the rate of turbulent kinetic energy dissipation present in the turbulent Couette viscometer simulations, an additional parameter that has been proposed as a possible predictor of hemolysis was investigated – the Kolmogorov Length Scale (KLS) (Kameneva, 2004).. The KLS is the smallest length scale in turbulent flow and is defined as:

$$\eta = \left(\frac{v^3}{\varepsilon} \right)^{\frac{1}{4}} \quad (3.4)$$

where v is the kinematic viscosity and ε is the rate of turbulent kinetic energy dissipation (Tennekes and Lumley, 1972). The Kolmogorov Length Scale has been proposed as a possible parameter for hemolysis estimation instead of typically reported Reynolds

stresses because they are the smallest turbulence scales, which if they are on the order of magnitude of the size of a RBC would be able to affect the cell - as opposed to Reynolds stresses, which can be related to much larger length scales.

3.2 FDA Critical Path Initiative

3.2.1 Geometry and Flow Conditions

The nozzle geometry was specified by the FDA, and is shown in Figure 1.1. The entrance and exit tube diameters were 0.012 m, the diameter of the throat was 0.004 m and the length of the throat was 0.04 m. Simulations were run using both orientations of the nozzle geometry: (1) a sudden contraction with a conical diffuser and (2) a gradual contraction with a sudden expansion. For each orientation, 5 simulations were completed, representing Reynolds numbers of 500, 2000, 3500, 5000 and 6500.

For momentum, the 1st order upwind interpolation scheme was used; for pressure, the standard Fluent interpolation; and for pressure-velocity coupling, the SIMPLE scheme was used. The specified fluid for all simulations was considered Newtonian, with a viscosity of 0.0035 Pa-s and a density of 1056 kg/m³. For those simulations performed in the turbulent regime, the turbulent k-ε model was used, with the default model parameters.

3.2.2 Computational Domain

3.2.2.1 Boundary Conditions

Based on the Reynolds number for the specified flow rate, either the laminar or turbulent k-ε model was used. A mass-flow inlet and an outflow outlet were specified for both of the simulation orientations (sudden expansion and sudden

contraction). A symmetry boundary condition was specified at the midplane, so that modeling of only half of the experimental geometry was required. All walls were given a no-slip boundary condition.

3.2.2.2 Grid

The experimental nozzle geometry was created in Gambit 2 as a 3D, hexahedral grid. The mesh was imported as a 3D model into Fluent 6. 700,000 grid cells were required to achieve grid independence, with smaller cells concentrated near the walls of the nozzle. This led to an average cell size of $4 \times 10^{-2} \text{ mm}^3$. The grid used for both the sudden expansion and the sudden contraction orientations is shown in Figure 2.2.

3.3 FDA Critical Path Initiative Results

3.3.1 Velocity

A plot of the velocity magnitude contours and velocity vectors for both orientations at all Reynolds numbers is given in Figures 3.2 and 3.3. The acceleration of the fluid in the contraction is shown for both cases, as well as the jet present after the sudden expansion, in that orientation. For the conical diffuser orientation, the maximum velocity in the constriction ranges from 0.5 m/s for the Re number 500 case to 6.4 m/s for the Re number 6500 case. A similar range of 0.6 to 5.8 m/s is found in the constriction for the sudden expansion orientation. For the conical diffuser orientation, the acceleration of the fluid at the entrance of the contraction is more rapid than for the sudden expansion orientation. For the sudden expansion, a recirculation zone is found directly following the expansion on either side of the jet.

3.3.2 Shear Stresses

The shear stress contours for the sudden contraction and the sudden expansion at the simulated Reynolds numbers is given in Figures 3.4 and 3.5. It is clear that the stresses increase as the Reynolds number increases for both orientations, with the highest stresses present near the wall of the contraction and on the edge of the jet in the case of the sudden expansion. In the conical diffuser orientation the maximum shear stress, occurring near the walls of the constriction, ranged from 9.5 to 190 N/m². For the sudden expansion orientation, this maximum shear stress ranged from 12.5 to 280 N/m². The maximum shear stresses are higher in the sudden expansion orientation for all Reynolds numbers.

3.3.3 Reynolds Stresses

The Reynolds stress contours for the sudden contraction and the sudden expansion at the simulated Reynolds numbers are given in Figures 3.6 and 3.7. It is clear that the stresses increase as the Reynolds number increases for both orientations, with the highest stresses present near the wall of the contraction and on the exterior of the jet, with an increasingly large “plume” of Reynolds stresses in the jet of the sudden expansion as Reynolds number is increased. The maximum Reynolds stress for each case ranges from 12.5 to 1700 N/m² for the conical diffuser orientation, and from 12.5 to 850 N/m² for the sudden expansion orientation. The highest Reynolds stresses are found at the sharp contraction of the conical diffuser orientation. Reynolds stresses have been proposed by some as a comparable stress to shear stress in laminar flow for hemolysis estimation in turbulent flow (Giersiepen, 1990; Hanle, 1987; Nygaard, 1992; Schoephoerster, 1991), however support for this measure as an appropriate predictor of cell damage is lacking;

which might be explained by the underlying differences in the mechanism for momentum transfer.

3.4 Capillary Tube Geometries and Computational Domain

3.4.1 Geometries and Flow Conditions

The dimensions of the capillary tube were 0.035 cm inner diameter and 2.8 cm length for all simulations. The flow equations were solved using the implicit formulation and the laminar solver available in Fluent, because all capillary Reynolds numbers were within the laminar regime. For momentum, the 1st order upwind interpolation scheme was used; for pressure, the standard Fluent interpolation; and for pressure-velocity coupling, the SIMPLE scheme was used.

Twenty-one experiments were reproduced computationally, representing different entrance geometries, flow rates and fluid viscosities. See Table 3.1 for a summary of these conditions. Four different two-dimensional models were created, representing the variations in contraction ratio (for a sharp contraction) as well as the tapered contraction that was also investigated experimentally by Keshaviah. The contraction ratio is the ratio of the larger chamber diameter to the capillary tube diameter (see Figure 1.1 for a contraction ratio of 3:1). Specifically, these included a contraction ratio of 27:1 with flows ranging in Re between 700 and 1050, a contraction ratio of 3:1 with flows ranging from Re 875 to 1255, a contraction ratio of 2:1 with flows ranging from Re 925 to 1230, as well as simulations with more than double the viscosity of those previously discussed and a contraction ratio of 27:1, with flows ranging from Re 200 to 400. The specified fluid for all simulations was considered Newtonian, with a viscosity of 0.005 Pa-s for

most simulations and a viscosity of 0.013 Pa-s for simulations of Keshaviah's higher viscosity experiments with dextran.

3.4.2 Computational Domain

3.4.2.1 Boundary Conditions

The boundary conditions were specified as a mass flow rate inlet condition and as an outflow outlet condition at the capillary exit. The centerline of the capillary was specified as the axis, about which the model was symmetric. A no-slip boundary condition was applied at the walls.

3.4.2.2 Grid

To set up the computational model, a two-dimensional representation of the capillary tube and entrance geometry was created and fitted with a quadrilateral grid using the mesh-generation software Gambit 2. The mesh was then imported to the CFD package Fluent 6 as a two-dimensional, axisymmetric model. For each model, an initial simulation was run using the mesh created in Gambit. After this initial simulation, the mesh was refined in regions of high velocity gradient and then refined globally until the velocity magnitude at multiple points in the domain did not change significantly (percent difference < 3%) with additional decreases in grid cell size. The average number of nodes for grid-independent results for the simulated capillaries was approximately 710,000, with smaller mesh cells concentrated near the entrance of the capillary and in other regions where high gradients of velocity would be expected. This method of grid refinement led to an average computational cell size at the entrance of the capillary on the order of magnitude of $5 \times 5 \mu\text{m}$, with smaller cells concentrated closer to the capillary wall. The size of the smallest grid cells is smaller than the size of a red blood cell, thus

the assumption of a Newtonian fluid does not hold at this scale for the flow of red blood cells. However, this level of refinement was only required in order to resolve the sharp corner of the capillary entrance and not the bulk flow, allowing for the assumption of Newtonian behavior for the majority of the flow.

3.5 Capillary Tube Results

3.5.1 Maximum Shear Stress Along Threshold Streamline

Because most investigators consider the shear stress to be one of two major factors in hemolysis, the first parameter investigated was τ_{rz} . When the shear stress is calculated for the entire domain, it is clear that as the fluid enters the capillary tube from a larger chamber an area of high velocity gradients and shear stresses develops at the corner of the contraction (Figure 3.8). This area of higher shear is also observed when the shear stress is plotted along the specified threshold streamline – as evidenced by a sharp spike in shear stress magnitude at the capillary entrance (Figure 3.1). When the maximum shear stress along the threshold streamline for all cases is plotted (varying Reynolds number, contraction ratio, and viscosity), no uniform threshold value of stress is observed (Figure 3.9). In Figure 3.9, a linear regression of the shear stress data versus percent hemolysis is shown. In the presence of a threshold shear stress value, the slope of shear stress versus hemolysis should be zero, however, the large slope of this regression line indicates that the peak value of shear stress does not yield a threshold stress value that applies for all experimental scenarios.

3.5.2 Maximum Gradient of Shear with Respect to Displacement

Along a Streamline

The second parameter investigated as a possible cause of cell lysis was the gradient of the shear stress with respect to displacement along a given streamline. A large gradient in shear stress might give rise to a tension sufficient to rupture the cell membrane. This analysis also does not yield a threshold value that was common for all experimental scenarios, as seen in Figure 3.10. Instead, a nonlinear relationship with hemolysis was observed and, although hemolysis levels are much higher in the higher viscosity simulations, the gradient of the shear stress along the threshold streamline is much smaller in magnitude than that for the lower viscosity experiments.

3.5.3 Maximum Extensional Components of Stress Tensor on

Threshold Streamline

The final factors investigated as possible predictors of hemolysis in this flow were the extensional components of the stress tensor. Like shear stress, these components exhibited spikes in magnitude in the entrance to the capillary tube. The extensional stresses also vary depending on location within the domain – the magnitude is nearly zero in most of the entrance chamber and the capillary while close to the wall at the entrance it is as much as an order of magnitude larger than the maximum value on the threshold streamline. Unlike shear stress and the shear stress gradient, the extensional stresses yield a consistent threshold for hemolysis. When either the maximum radial or axial extensional stress is found along the specified threshold streamline, and these data are compared across all simulated experiments, little variation in the maximum value of extensional stress with hemolysis is seen (Figure 3.11).

The extensional components of the stress tensor are significant in the entrance region of the capillary and similar in magnitude to τ_{rz} (Figure 3.12). From the Figure 3.12, it is clear that the radial extensional component is near zero everywhere except the entrance, where a large spike in stress magnitude occurs. In comparison, the shear stress magnitude is small in the entrance chamber and peaks during the contraction, then levels off in the capillary tube at a value of the same order of magnitude as the peak. This indicates that, if lysis were correlated to shear stress only, the damage would not be associated with the entrance region, contrary to Keshaviah's conclusions.

Shear stress and exposure time have been reported for years as the major factors contributing to hemolysis, but alone in power law models have not served as an adequate framework for broadly understanding cell damage in the laboratory or clinic. Alternatively or in combination, extensional stress may be a significant factor contributing to failure of the RBC membrane. Zhao et al. examined the deformability of the RBC in a constricted microchannel where cells were subjected to a shear stress up to 5000 Pa (Zhao, 2006). They found that a maximum RBC elongation index (i.e., the same quantity termed as deformability index in Lee et al.) of approximately 0.5 was reached at a shear stress of 123 Pa in the entrance to the constriction. Zhao et al. did not observe cell rupture in their experiments, however it appears that a chamber with a well-rounded capillary entrance was used, which would lower stress levels at the entrance of the constriction. Using conditions from the worst-case hemolysis experiment by Keshaviah (27:1 contraction ratio, highest flow rate), an additional simulation with a well-rounded entrance (as defined in Vennard, 1961) was performed. It was found that the extensional stresses along the threshold streamline decreased significantly, below a level that

hemolysis would be expected based on the results presented here (axial stresses were reduced by 1/2, radial stresses were reduced by an order of magnitude). The importance of constriction inlet geometry on hemolysis level has been observed elsewhere (Umezu, 1995), and is a valid reason for the lack of cell rupture seen by Zhao et al. The fact that Zhao et al. did not observe cell rupture, even at shear stresses of 5000 Pa, tends to support our conclusion that shear stress was not the determining factor for hemolysis in Keshaviah's experiments, where shear stresses of the same order of magnitude were present.

The significance of the entrance region to hemolysis is reiterated in the comparison shown in Figure 3.13. With a flow rate nearly twice as large, shear stresses for fully developed flow in the capillary region of Figure 3.13A with a tapered entrance must be greater than those of the capillary of Figure 3.13B with the sharp contraction. Cell damage, however (as measured by hemoglobin loss) was more than 3 times as great (6% vs. 1.8%) for the abrupt 27:1 contraction when compared to the gradual entrance. Thus, something unique to the capillary orifice seems to be causing hemolysis in this flow system. Also underlining the effect of the entrance region, it was determined that the maximum shear stress along the threshold streamline is not significantly larger than the shear stress experienced by the fluid while in the capillary – a fact that does not fit well with the conclusion that entrance effects are the predominant cause of blood cell trauma in this system, especially when one considers the exposure time to be orders of magnitude larger within the capillary. In contrast, extensional stresses exist only in the neighborhood of the capillary orifice. That is, they are unique to the entrance and they are similar in magnitude to shear stress.

The more cogent evidence from this study in support of extensional stress comes from the "all-or-nothing" threshold analysis, in which a series of threshold streamlines were calculated for a series of experimental scenarios. Maximum shear stress fails to exhibit a threshold value consistent with the level of hemolysis (Figure 3.9). Moreover, the magnitude of the maximum shear stress on the threshold decreases markedly as hemolysis increases! On the other hand, the peak values of the extensional stresses τ_{rr} and τ_{zz} along the threshold streamline remain relatively constant when plotted against level of hemolysis (Figure 3.11). When comparing the four parameters studied, one can look at the spread of the data for each in an attempt to determine which has the characteristics of an appropriate threshold value. The spread is a measure of how close all collected data points are to the average value of those data points and is defined as the range of values divided by the mean of all values. The spread for the peak gradient of the shear and the peak shear stress, 2.00 and 0.85 respectively, was larger than that for the peak radial and axial extensional stresses, with values of 0.43 and 0.55 respectively.

The analysis of each variable discussed thus far is based on the assumption that there is a threshold magnitude of any given variable and that this threshold magnitude is experienced by a cell traveling along a streamline chosen to correspond to the assumed boundary between the hemolysis zone and the hemolysis free zone. Assuming that there is a constant threshold value of any given variable, it would be expected for plots of the maximum magnitude of this variable found on the threshold streamline versus the percent hemolysis to yield a horizontal line – i.e. the maximum value of the variable on the threshold streamline and percent hemolysis should have no correlation because the percent hemolysis is taken into account when choosing the threshold streamline. One

measure of the correlation between two variables is the coefficient of determination, or r^2 . The coefficient of determination, r^2 , is a measure of how well the data can be predicted by the regression and is equal to the sum of the squared differences between the actual data values and the average of all data values (the total sum of squares) minus the sum of the squared differences between the actual data values and the estimated values from the regression, normalized by the total sum of squares (Excel 2007 User's Guide). In the absence of randomly distributed points, correlation coefficients r^2 near zero suggest a constant function relationship. Linear regression yielded r^2 values for τ_{rr} and τ_{zz} of 0.20 and 0.16, which compared to 0.75 for τ_{rz} . We believe these results make a strong case for hemolysis by extensional flow. The maximum value of the angular component of the stress tensor on the threshold streamline was also analyzed but yielded a significantly lower magnitude, approximately a quarter of the value of the other components, and an r^2 value of 0.92, thus this component was not considered further. It is difficult to tell whether τ_{rr} or τ_{zz} might be more important than the other for this flow; in some cases, τ_{zz} is slightly larger, but cells experience large values of τ_{rr} first and the exposure time is longer while in other cases the reverse is true. In any case, onset of damage in Keshaviah's experiments occurs at stress levels of approximately 3000 Pa with exposure times on the order of microseconds. The level is comparable to the magnitude of stress reported for jets with a similar exposure time, where shear stresses were assumed to be responsible (Leverett, 1972). It is also well above stresses on the order of 10 Pa applied by Lee in his microfluidics system, for which he specifically noted the absence of cell rupture with extensional flow (Lee, 2009).

These findings do not eliminate shear stress as playing an important role in hemolysis, but they do indicate that extensional components must be considered for accurate predictions. Extensional flow is a feature common to contractions and expansions, geometries notably relevant to many clinical situations and to the FDA Critical Path Initiative. While the present investigation dealt with laminar flows, it perhaps raises the issue as to whether extensional components in turbulence might also be contributing to clinical instances of hemolysis, an area that is also undergoing reexamination (Antiga, 2009; Kameneva, 2004).

3.5.4 Illustrated Mechanism of Damage Due to Elongational Flow

Since extensional flow more effectively increases DI, and DI has been related to cell damage, the findings in this work are consistent with extensional flows contributing to hemolysis. It is not clear whether shear stress is a necessary element or not. Results from the literature on red cell rheology do help to suggest a mechanism by which shear stress and extensional stress might work in concert. The motion of an RBC in a shearing flow field is unusual. Rather than rotating, the cell membrane revolves around the cytoplasm in a manner characterized as “tank treading.” (Fischer, 1978). Fischer deduced the motion of the red cell membrane from videomicroscopy images of cells during flow in a device called the rheoscope, essentially a specially constructed cone and plate viscometer (Fisher, 1980). Increases in the shear rate result in a higher frequency of revolution with the same basic velocity profile for the membrane. Described in Cartesian components after Fischer, the velocity components in the membrane (Figure 3.14) are $v_x = fC(y)$ and $v_y = 0$ where f is the tank-tread frequency and $C(y)$ represents the

circumference parallel to the x-axis. This velocity profile describes a shearing flow within the two dimensional structure of the red cell membrane.

Observations in micropipette deformation experiments led to the characterization of the red cell membrane as essentially a two dimensional fluid (Evans, 1979), and, since dilation of only a few percent results in rupture, it can be characterized as a two dimensional incompressible fluid. As such, flow in the membrane must satisfy the two dimensional continuity equation:

$$\frac{\partial v_x}{\partial x} + \frac{\partial v_y}{\partial y} = 0 \quad (3.5)$$

Note that Fischer's velocity profile for the erythrocyte membrane given above satisfies the mathematical constraint of continuity. Moreover, with v_y identically equal to zero in a shearing flow, it follows that v_x must be a constant at any given value of y to satisfy the continuity equation. A cell entering a region with an extensional flow component in the direction of translation, will encounter a gradient of v_x and, constrained by continuity, it dilates with the prospect of failure. This is precisely the situation with the complex flow in the entrance region of the capillary. This mechanism could possibly also explain hemolysis due to changes in the permeability of the red blood cell membrane, attributed to the opening of pores in the cellular membrane through which hemoglobin can leak. An implicit assumption to this analysis is that the two dimensional incompressible fluid character observed at the very low deformation rate of the micropipette experiments and at the intermediate deformation rates of the rheoscope apply at the high deformation rates of the capillary tube.

3.6 Turbulent Couette Viscometer Geometry and Computational Domain

3.6.1 Geometries and Flow Conditions

The Couette viscometer simulation geometry was created based on the gap width of 2.07 mm given in Sutura et al.'s work. This geometry can be seen in Figure 1.3. To reduce computational time, only the gap, and not the conical or top portions of the viscometer, was modeled. For these simulations, the procedure was to begin the simulation with a slowly rotating inner wall (so that the flow would be in the laminar regime), and to slowly increase the rotational rate of the wall until the shear stress values obtained experimentally were achieved. A number of simulations were completed because of this process of ramping up the rotational rate of the wall, but data was extracted for only seven rotational rates, corresponding to the shear values investigated in Sutura's work. The shear stress levels investigated were 1500, 2000, 2500, 3500, 4500 dynes/cm². Once the rotational rate was high enough that turbulence would be anticipated, the realizable k- ϵ turbulence model and enhanced wall functions were employed.

For momentum, the 1st order upwind interpolation scheme was used; for pressure, the standard Fluent interpolation; and for pressure-velocity coupling, the SIMPLE scheme was used. The specified fluid for all simulations was considered Newtonian, with a viscosity of 0.001 Pa-s and a density of 998.

3.6.2 Computational Domain

3.6.2.1 Boundary Conditions

Using the given dimensions from Sutura's work, a three-dimensional model of 1/16th of the experimental geometry was created. The model was specified as symmetric

in the z-direction, with symmetry boundary conditions at the top and bottom of the domain, and rotationally periodic, with periodic boundary conditions on both sides of the simulation domain. The inner and outer walls of the viscometer were given a no-slip boundary condition. The simulation was begun by specifying a rotational velocity of the inner wall such that the flow would remain laminar, followed by slowly increasing the rotational rate of the inner wall until the resulting shear stress was equal to the experimental values given by Sutura, et al. At this point, the flow was in the turbulent regime.

3.6.2.2 Grid

As previously mentioned, 1/16th of the experimental geometry was created in Gambit 2. The geometry was then fit with a hexahedral grid. This grid was imported into Fluent and subsequently refined. The number of grid cells was 33,600, with an average grid cell size of $4 \times 10^{-3} \text{ mm}^3$.

3.7 Turbulent Couette Viscometer Results

Flow in a Couette viscometer with inner cylinder rotating and outer cylinder stationary can be characterized by a dimensionless parameter called the Taylor number, mentioned in Chapter 2. For the rotational rates used in the simulation of Sutura's work, the Taylor number ranged from approximately 5000 to 10,000; well above the transition Taylor number of 400. Thus, the flow for all simulations was in the turbulent Taylor vortex regime. Each of the vortices observed in the simulation results contained an assumed equal portion of the flow; therefore in order to perform an all-or-nothing analysis of the stresses present similar to that for the capillaries, it was necessary to create

iso-surfaces of the desired variables so that the percent of the volume contained by the created iso-surface corresponded to the percent hemolysis. The maximum turbulent kinetic energy dissipation and Kolmogorov Length Scales were examined using these surfaces and throughout the entire domain.

3.7.1 Turbulent Kinetic Energy Dissipation Rate

Initially, because some investigators have put forth turbulent kinetic energy dissipation as a possible predictor of hemolysis in turbulent flow, isosurfaces were created such that the percentage of the volume outside the isosurface was equal to the percent hemolysis and the maximum turbulent kinetic energy dissipation on these isosurfaces was determined. Figure 3.15 shows the percent hemolysis versus this maximum turbulent kinetic energy dissipation rate, however no correlation between these values is observed.

3.7.2 Kolmogorov Length Scale

Some researchers have speculated that the Kolmogorov length scale, a parameter related to the rate of energy dissipation, and the smallest length scale in turbulent flow, may be related to hemolysis of cells in turbulent flow (Kameneva, 2004). The Kolmogorov Length Scale is the smallest length scale in turbulent flows – i.e., the size of the smallest eddies in the flow. The proposed mechanism through which hemolysis in turbulent flows might be related to the Kolmogorov Length Scale, is that if length scales approaching the size of a red blood cell were present, these eddies might lead to cell rupture. In Figure 3.16, it can be seen that Kolmogorov Length Scales are small in the Couette viscometer, and in parts of the domain (on the outer edges of the vortices) are of the size of a red blood cell. These results compare well to the results of others who have

investigated Kolmogorov length scales in heart valves. Ellis et al. found a KLS of 7 microns near the hinge region of prosthetic heart valves (Ellis, 1998). Travis et al. and Liu et al. found scales ranging from 36 – 72 microns and 25 – 47 microns, respectively, in other regions of the valve – which is of the same order of magnitude as some of the results found here (Travis, 2002; Liu, 2000). Additionally, Jones calculated the Kolmogorov length scales for four different experimental systems in which hemolysis was studied and found a range of 1.6 – 11 microns for the average KLS (Jones, 1995). Initially, isosurfaces of KLS were created in the hopes that a threshold KLS would emerge, so that hemolysis could be predicted by determining the volume of a flow encompassed by the threshold KLS, and that that volume would correspond to percent hemolysis. Assuming the system is well-mixed, if such a threshold existed, it would be expected for a plot of percent volume encompassed by the KLS isosurface versus gap shear to fall on the same curve as the percent hemolysis versus gap shear data of Suter for the threshold KLS. In Figure 3.17, however, it is clear that this is not the case – KLS isosurfaces of multiple KLSs were created, however the percent volume they enclose does not correspond to percent hemolysis for any KLS.

The lack of evidence for a threshold KLS motivated the study of the entire range of KLS in the flow, not just on the surface encompassing the volume that corresponds to percent hemolysis. A few statistical methods of looking at the overall Kolmogorov Length Scales in the flow were used, however it was found that only the median KLS had a correlation with percent hemolysis, with the median KLS becoming smaller as hemolysis increases, and the median KLS becoming larger as hemolysis decreases, up to the point where KLS are larger than the size of the cell and no hemolysis would be

expected. This correlation is shown in Figure 3.18. The Kolmogorov Length Scales present in the FDA CPI nozzle geometry were also plotted for the entire domain. It can be seen from Figure 3.19 that KLS length scales of the size of a red blood cell are present in the FDA nozzle. Publication of the results of an interlaboratory hemolysis study using the FDA nozzle are forthcoming, and may show this same dependence on median Kolmogorov Length Scale in the prediction of hemolysis.

The Couette viscometer simulations were performed using the realizable $k-\varepsilon$ turbulence model in Fluent. Although this model has improvements over the standard $k-\varepsilon$ model, some of the inherent deficiencies common to all $k-\varepsilon$ models as semi-empirical models are still present. One of these weaknesses involves the use of user-defined constants for parameters that can vary in reality. In order to have better confidence in the Kolmogorov length scale results presented here, other turbulence models should be used and compared. The use of Direct Numerical Simulation (DNS) would allow for a much more complete characterization of the flow in Sutura's Couette viscometer.

3.8 Conclusions

It is clear from the FDA Critical Path Initiative that there is still ample room and need for investigation of hemolysis related to flow. Simulations of laminar capillary entrance blood flow yield evidence that the hemolysis seen in this type of flow is related to the extensional components of the stress tensor. This, in combination with an available mechanism for rupture due to extensional stresses, leads to the conclusion that extensional stresses can be a significant cause of RBC trauma. This work proposes a threshold value of the extensional stresses for hemolysis of 3000 Pa for exposure times

on the order of microseconds. While this explanation does not eliminate the possibility that some hemolysis is caused by shear stress, there is sufficient indication that extensional stresses should be taken into account in blood trauma models. In addition, there is an indication that hemolysis in turbulent flows may be related to the Kolmogorov Length Scale, with scales on the order of the size of a RBC seen in turbulent flows known to produce hemolysis. Some dependence on the median Kolmogorov Length Scale for flow in a turbulent Couette viscometer has been shown, however much more work needs to be completed to prove the reliability of this parameter as an indicator of hemolysis.

Portions of this chapter have been reproduced from the following source:

Down LA, Papavassiliou DV, O'Rear EA. *Significance of Extensional Stresses to Red Blood Cell Lysis in a Shearing Flow*. Annals of Biomedical Engineering. 2011; 39: 1632 – 1642.

3.9 Nomenclature

ε - rate of turbulent kinetic energy dissipation

η - Kolomogorov length scale

μ - dynamic viscosity of blood

ν - kinematic viscosity

u_r – radial velocity

u_z – axial velocity

3.10 References

Antiga L, Steinman DA. Rethinking turbulence in blood. *Biorheol* 46: 77-81, 2009.

Bird RB, Stewart WE, Lightfoot EN. *Transport Phenomena*. New York: John Wiley & Sons, 2007 pp. 844.

Ellis JT, Wick TM, Yoganathan AP. Prosthesis-induced hemolysis: mechanisms and quantification of shear stress. *J Heart Valve Dis* 7: 376-386, 1998.

Evans EA, Skalak R. Mechanics and thermodynamics of biomembranes: part 1. *CRC Crit. Rev. Bioeng.* 3: 181-330, 1979.

Fischer TM On the energy dissipation in a tank-treading human red blood cell. *Biophys. J.* 32: 863-868, 1980.

Fischer TM, Stöhr-Liesen M, Schmid-Shönbein H. The red cell as a fluid droplet: tank tread-like motion of the human erythrocyte membrane in shear flow. *Science* 202: 894-896, 1978.

Hanle DD, Harrison EC, Yoganathan AP, Corcoran WH. Turbulence downstream from the loneseu-Shiley bioprosthesis in steady and pulsatile flow. *Med Biol Eng Comput* 1987; 25: 645-649.

Jones SA. A Relationship Between Reynolds Stresses and Viscous Dissipation: Implications to Red Cell Damage. *Ann Biomed Eng* 23: 21-28, 1995.

Kameneva MV, Burgreen GW, Kono K, Repko B, Antaki JF, Umezo M. Effects of turbulent stresses upon mechanical hemolysis: experimental and computational analysis. *ASAIO J.* 50: 418-423, 2004.

Keshaviah P. Hemolysis in the accelerated flow region of an abrupt contraction. Doctoral Dissertation. University of Minnesota. 1974.

Lee S, Yim Y, Ahn K, Lee S. Extensional flow-based assessment of red blood cell deformability using hyperbolic converging microchannel. *Biomed. Microdevices* 11: 1021-1027, 2009.

Leverett LB, Hellums JD, Alfrey CP, Lynch EC. Red blood cell damage by shear stress. *Biophys. J.* 12: 257-273, 1972.

Liu JS, Lu PC, Chu SA. Turbulence characteristics downstream of bileaflet aortic valve prostheses. *J Biomech Eng* 122: 118-124, 2000.

Nygaard H, Giersiepens M, Hasenkam JM, Reul H, Paulsen PK, Røvsing PE, Westphal D. Two-dimensional color-mapping of turbulent shear stress distribution downstream of two aortic bioprosthetic valves *in vitro*. *J Biomech* 1992; 25: 429-440.

Schoephoerster RT, Chandran KB. Velocity and turbulence measurements past mitral valve prostheses in a model left ventricle. *J Biomech* 1991; 24: 549-562.

Sutera SP, Mehrjardi MH. Deformation and fragmentation of human red blood cells in turbulent shear flow. *Biophys. J.* 15: 1-10, 1975.

Tennekes H, Lumley J. *A First Course in Turbulence*. MIT Press, 1972.

Travis BR, Leo HL, Shah PA, Frakes DH, Yoganathan AP. An analysis of turbulent shear stresses in leakage flow through a bileaflet mechanical prostheses. *J Biomech Eng* 124: 155-165, 2002.

Umezumi M, Fujimasa H, Yamada T, Fujimoto T, Ranawake M, Nogawa A, Kijima T. "Fluid dynamic investigation of mechanical blood hemolysis." In: 5th International

Symposium on Artificial Heart and Assist Devices, edited by T. Akutsu, and H. Koyanagi. Tokyo: Springer, 1995, pp 327-335.

Vennard JK. Elementary Fluid Mechanics. New York: John Wiley & Sons, 1961, pp. 315.

Zhao R, Antaki JF, Naik T, Bachman TN, Kameneva MV, Wu ZJ. Microscopic investigation of erythrocyte deformation dynamics. *Biorheol* 43: 747-765, 2006.

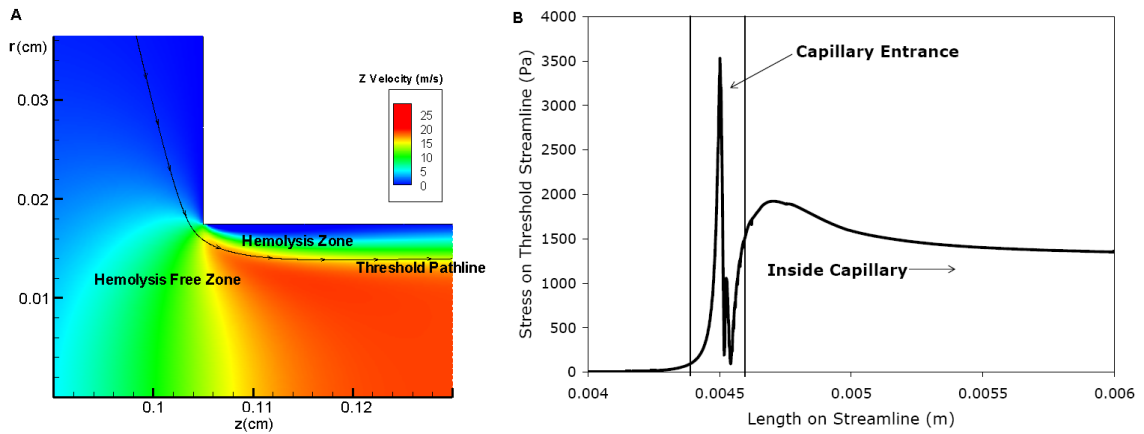


Figure 3.1. **A)** Contours of velocity magnitude at the corner of a 27 to 1 contraction ($Re = 1055$; $\mu = 0.005$ Pa-s). Flow is from left to right. The threshold streamline is shown, and the hemolysis and hemolysis free zones are illustrated. The volumetric flow rate passing through the area between the threshold streamline and the vessel wall as a percentage of the total volumetric flow is equal to the percent hemolysis for this experiment. The boundaries are not shown, but are similar to those given in Figure 1. **B)** The expected shear stress profile along the threshold streamline, with the large increase in shear stress magnitude at the entrance highlighted. CFD simulations indicate that there is a large peak in shear stress at the entrance followed by a constant shear stress value in the capillary. The peak in shear stress occurs at a streamline length, $s = 0.45$ cm, which corresponds to $z = 0.1038$ cm.

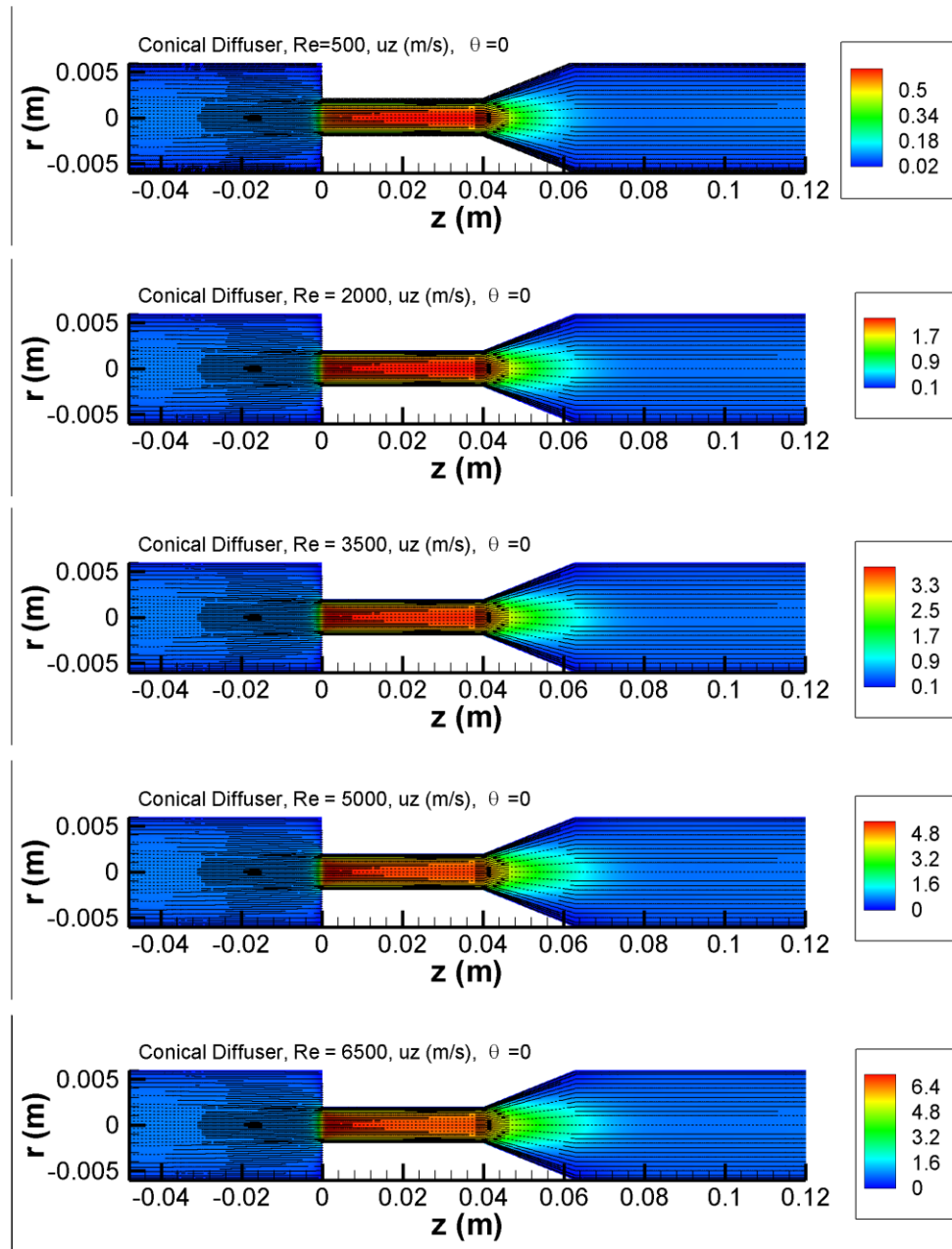


Figure 3.2. Velocity vectors and contours of velocity magnitude for the conical diffuser orientation of the FDA CPI nozzle.

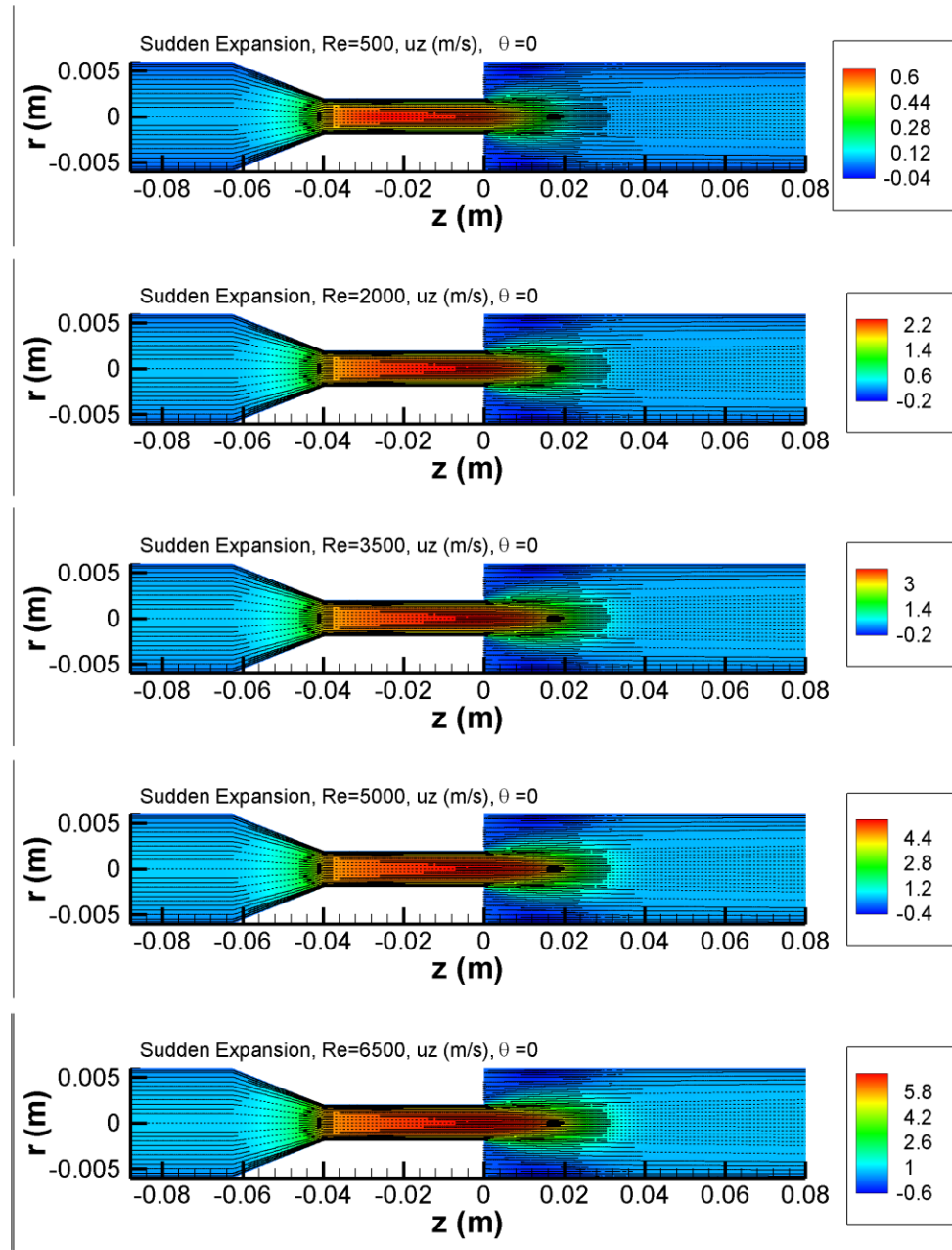


Figure 3.3. Velocity vectors and contours of velocity magnitude for the sudden expansion orientation of the FDA CPI nozzle.

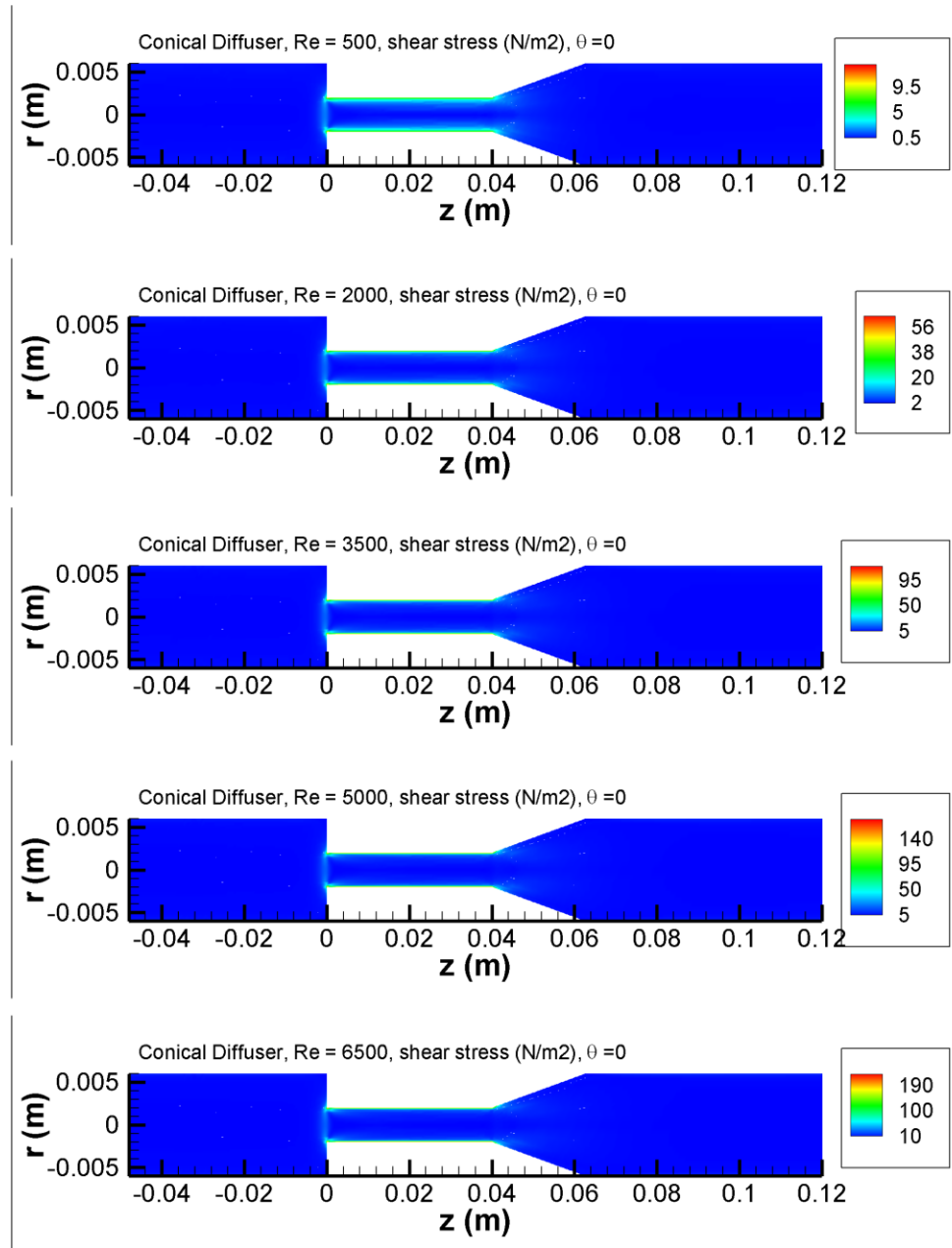


Figure 3.4. Contours of shear stress magnitude for the conical diffuser orientation of the FDA CPI nozzle.

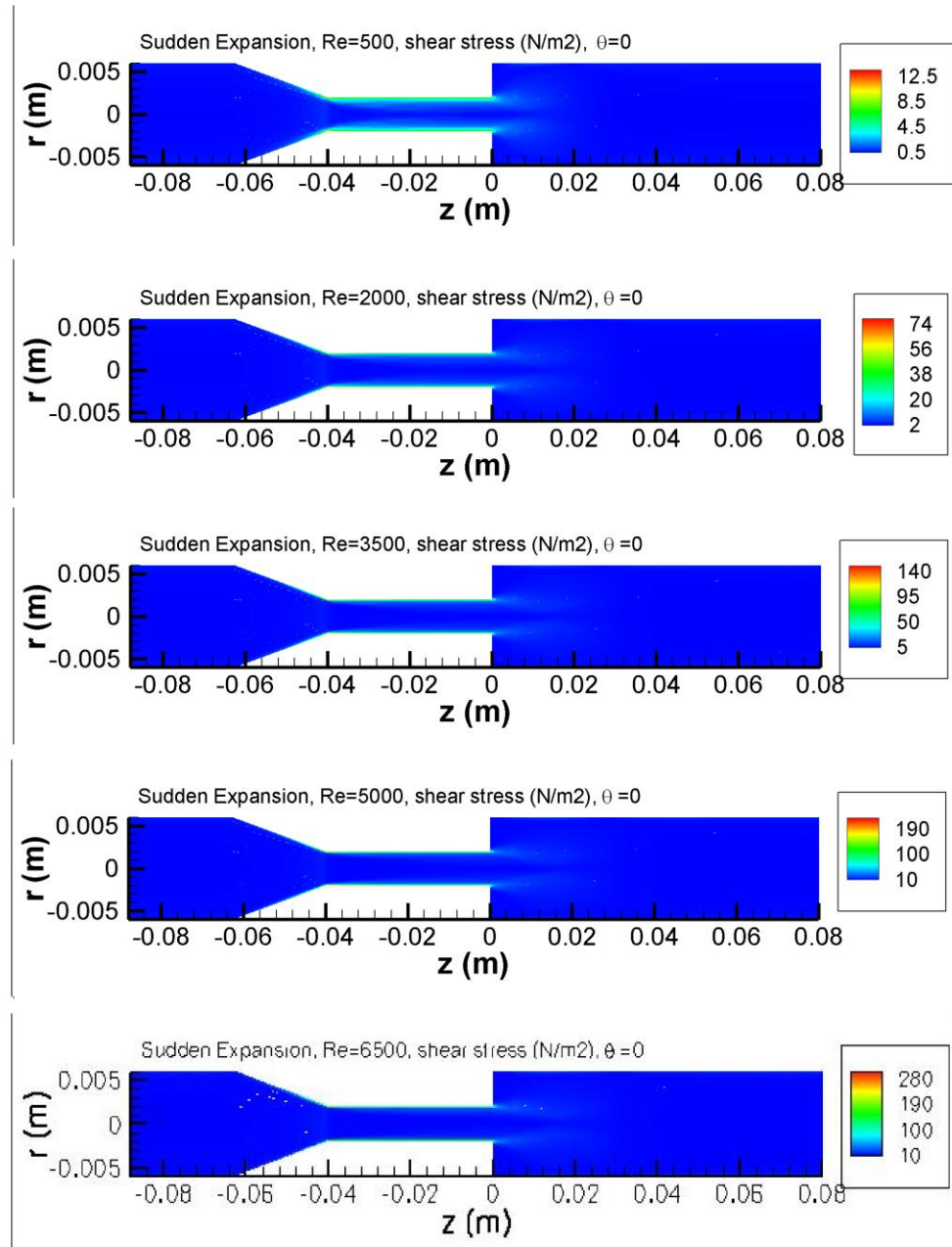


Figure 3.5. Contours of shear stress magnitude for the sudden expansion orientation of the FDA CPI nozzle.

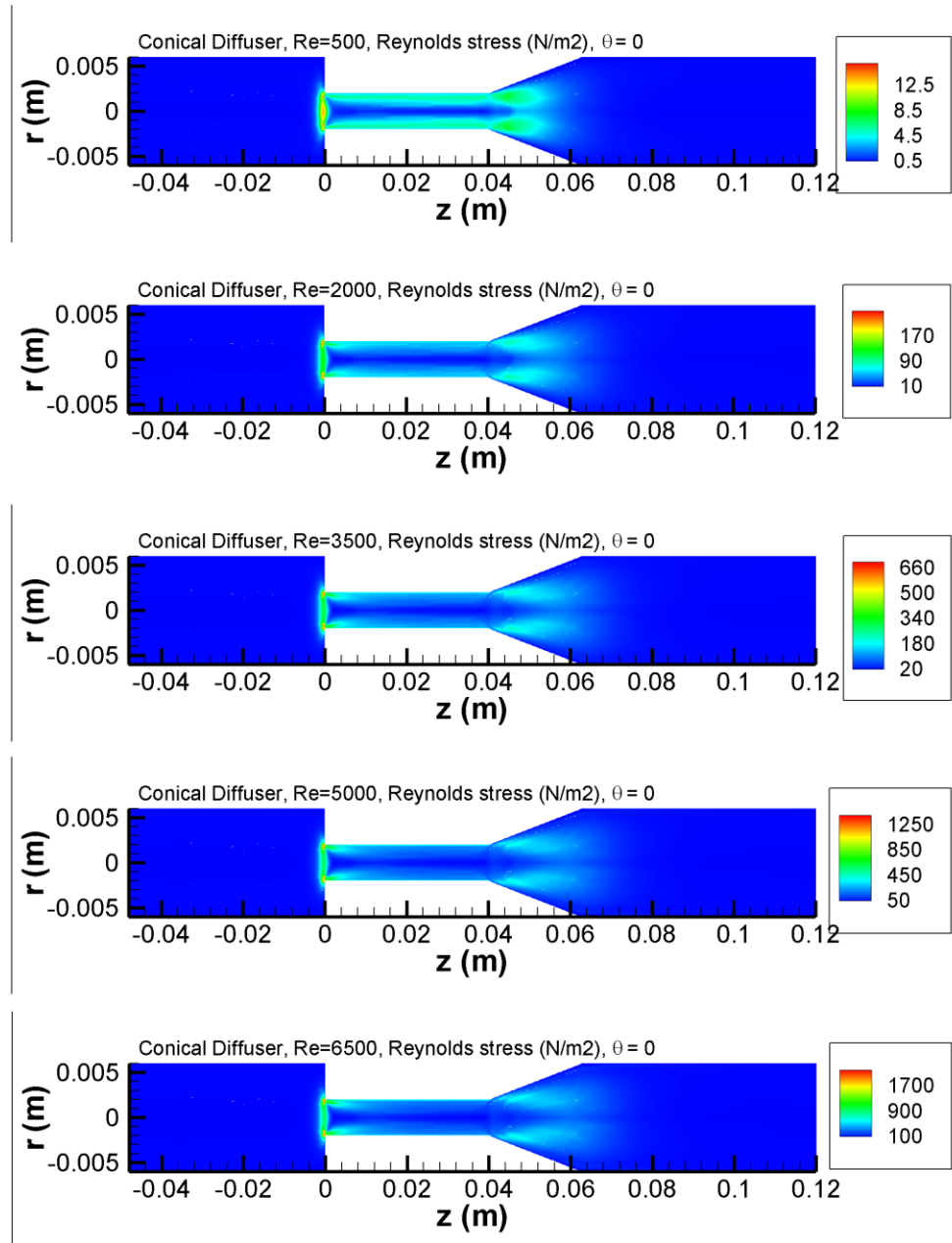


Figure 3.6. Contours of Reynolds stress magnitude for the conical diffuser orientation of the FDA CPI nozzle.

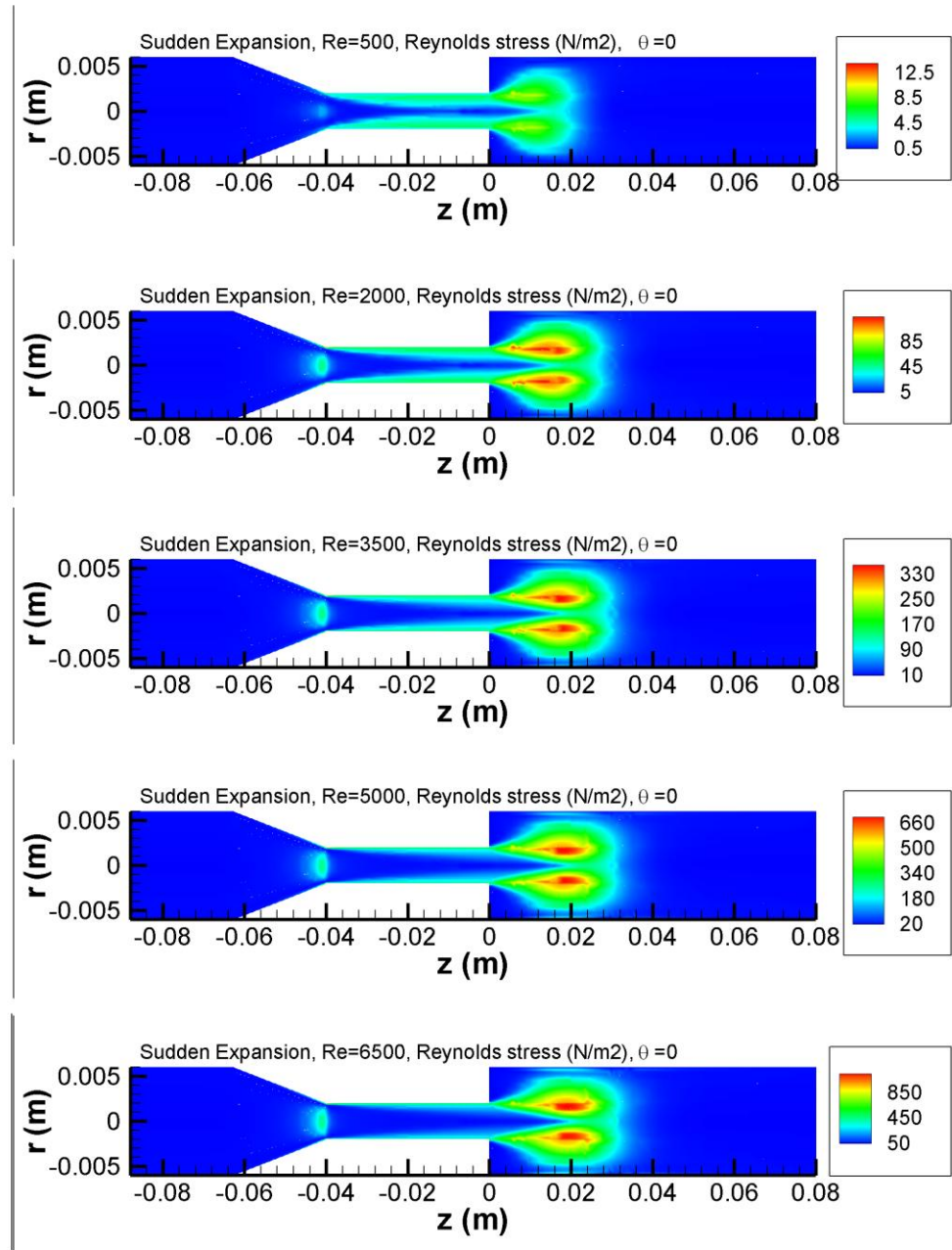


Figure 3.7. Contours of Reynolds stress magnitude for the sudden expansion orientation of the FDA CPI nozzle.

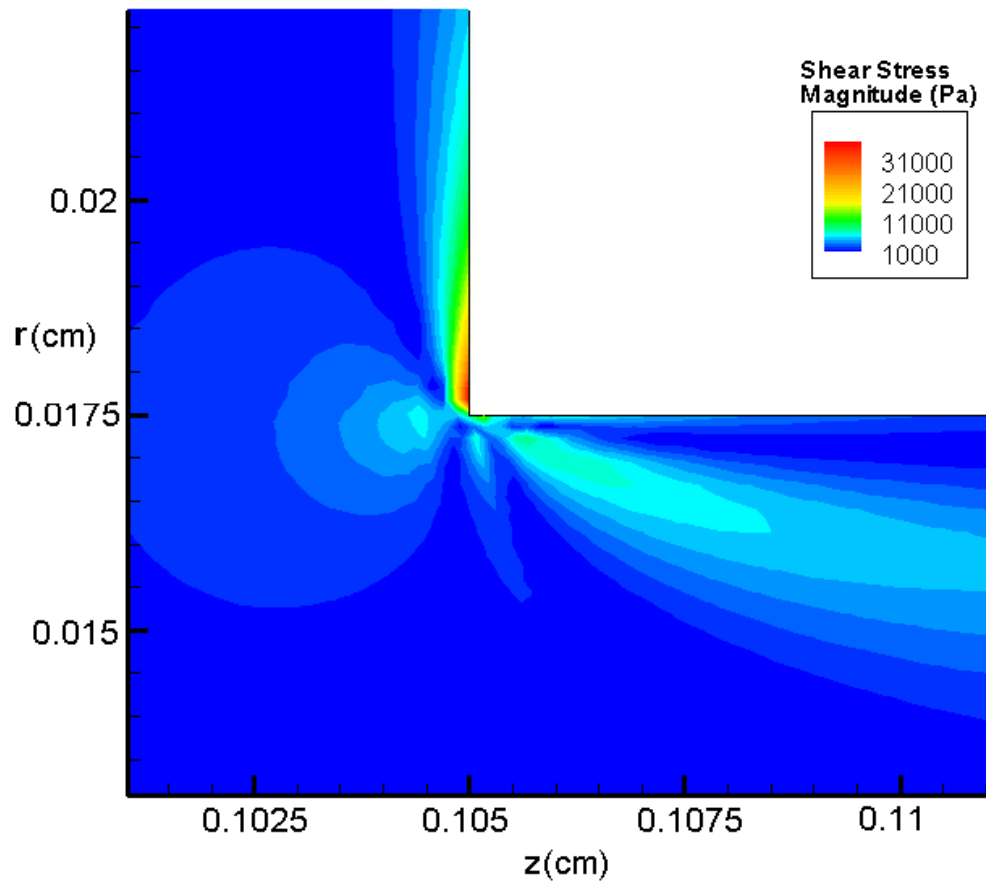


Figure 3.8. Contours of shear stress magnitude at the entrance of a sharp contraction ($CR = 27:1$; $Re = 1055$; $\mu = 0.005$ Pa-s). High shear stresses are seen at the corner of the contraction, and a plume of elevated shear stress magnitude is seen to extend into the capillary. CR: Contraction Ratio.

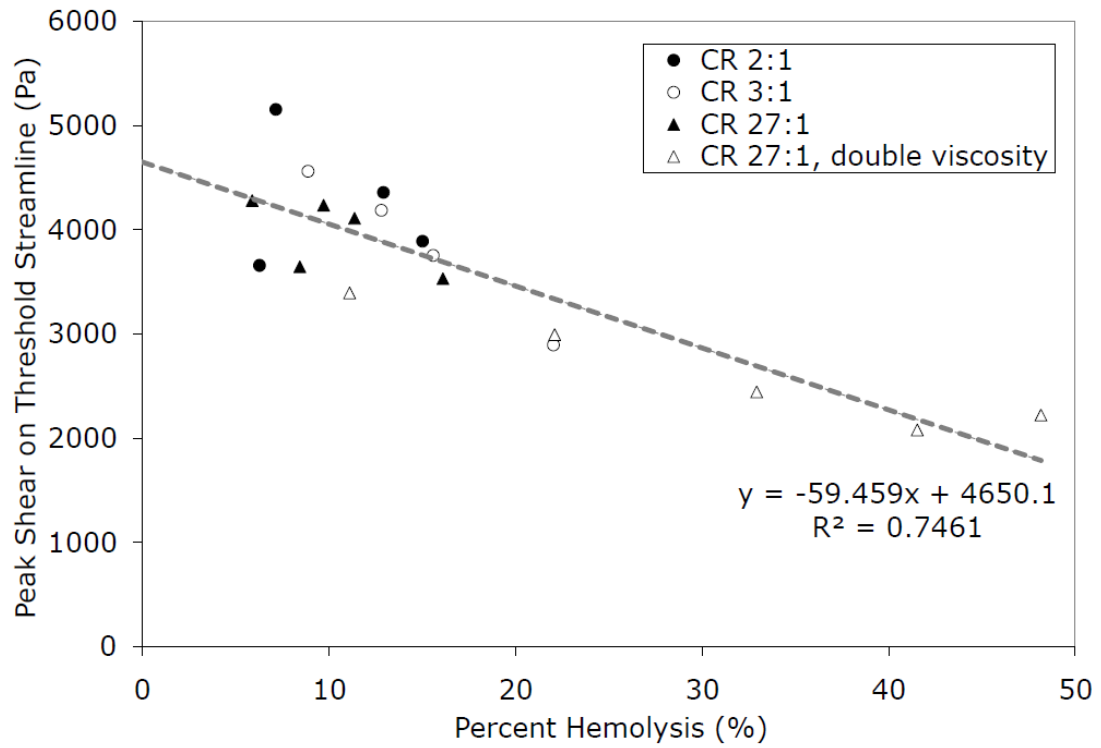


Figure 3.9. Peak shear stress on threshold streamline versus percent hemolysis. The slope of the trendline shows the lack of a consistent threshold peak shear stress across investigated parameters. Hemolysis threshold streamline is chosen such that the "hemolysis zone" shown in Figure 2 encompasses a fraction of the flow equal to the percent hemolysis from Keshaviah's data. CR: Contraction Ratio.

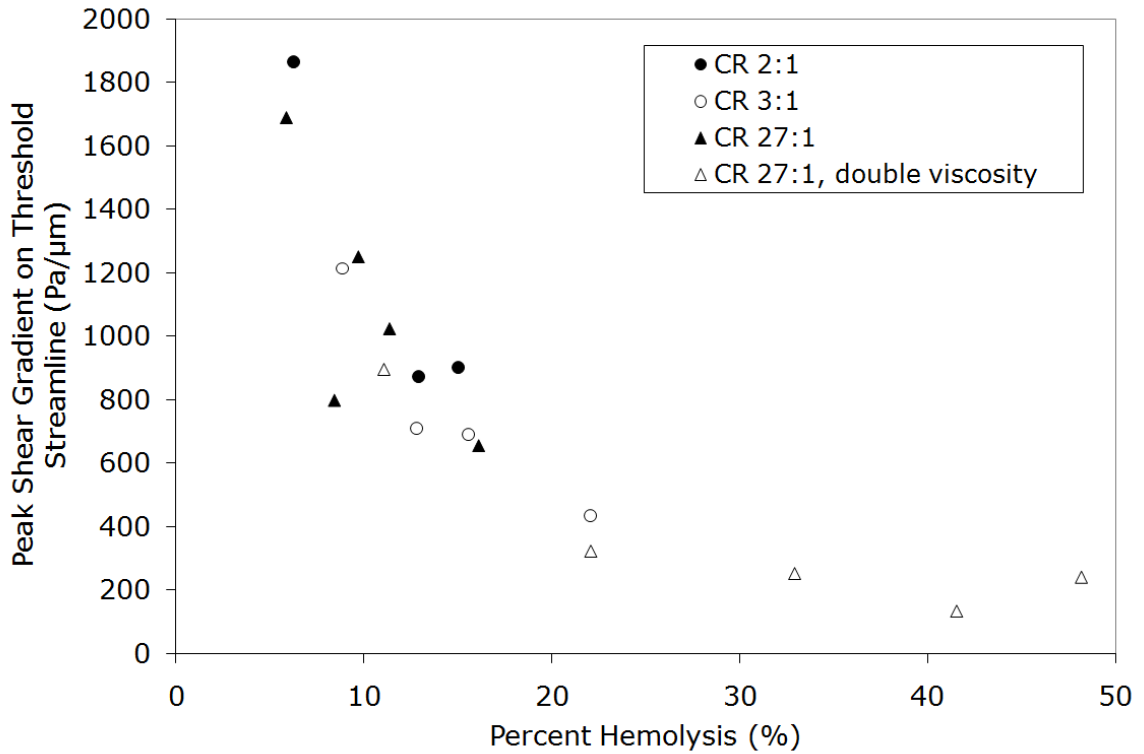


Figure 3.10. Peak gradient of shear stress with respect to displacement along a streamline on the threshold streamline versus percent hemolysis. The data does not indicate a constant threshold value for the gradient of the shear stress, and lower gradients are observed for the higher viscosity experiments, even though hemolysis is higher. CR: Contraction Ratio.

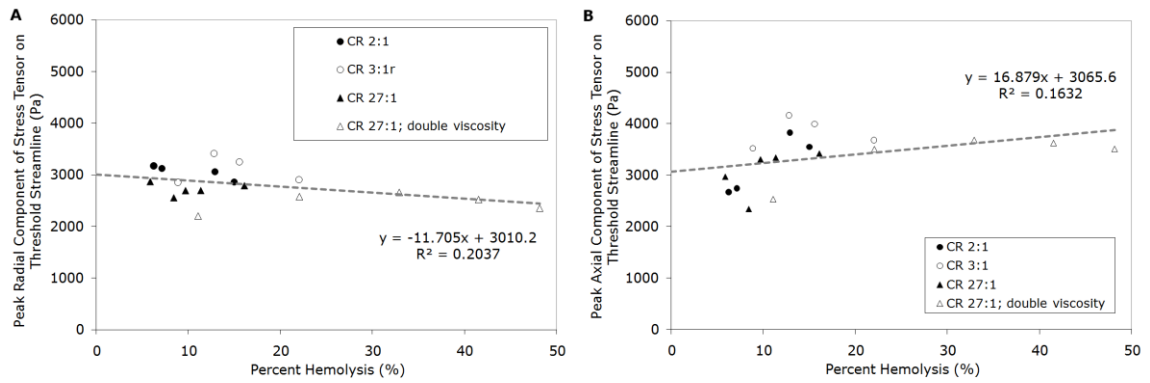


Figure 3.11. **A)** Peak radial stress tensor component on threshold streamline versus percent hemolysis for various contraction ratios and viscosities. **B)** Peak axial stress tensor component on threshold streamline versus percent hemolysis for various contraction ratios and viscosities. For both plots, a regression of the data is shown – for both extensional components, the slope of the regression is smaller than that for the shear stress.

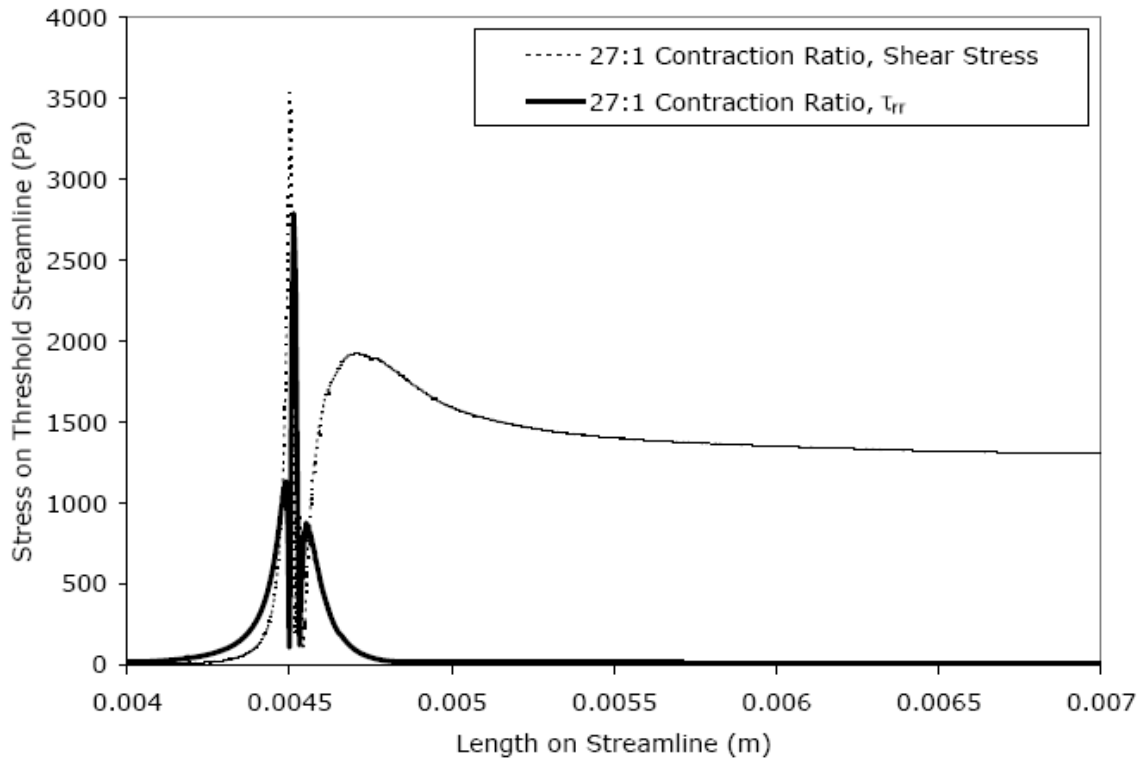


Figure 3.12. Comparison of τ_{rz} and τ_{rr} along the threshold streamline for a single experimental scenario ($Re = 1055$; $\mu = 0.005$ Pa-s). This plot shows that τ_{rr} has a sharp peak at the entrance of the capillary and then drops to zero once in the capillary, while the shear stress peaks at the entrance, but then maintains a value of the same order of magnitude as the peak through the capillary. This indicates that the effect of τ_{rr} is concentrated at the entrance of the capillary, while that of τ_{rz} likely would be an important effect throughout the capillary, contrary to the entrance-effect conclusions of Keshaviah.

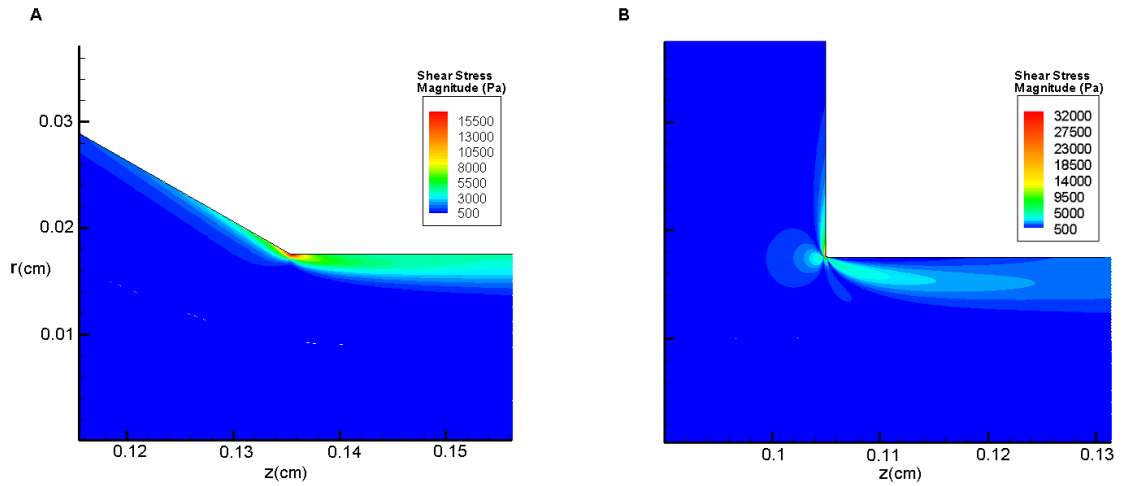


Figure 3.13. Contours of shear stress magnitude for (A) a tapered geometry with a high volumetric flow rate and (B) a 27 to 1 sharp contraction with a low flow rate. For (A) $Re = 1173$; $\mu = 0.005$ Pa-s; For (B) $CR = 27:1$; $Re = 706$; $\mu = 0.005$ Pa-s

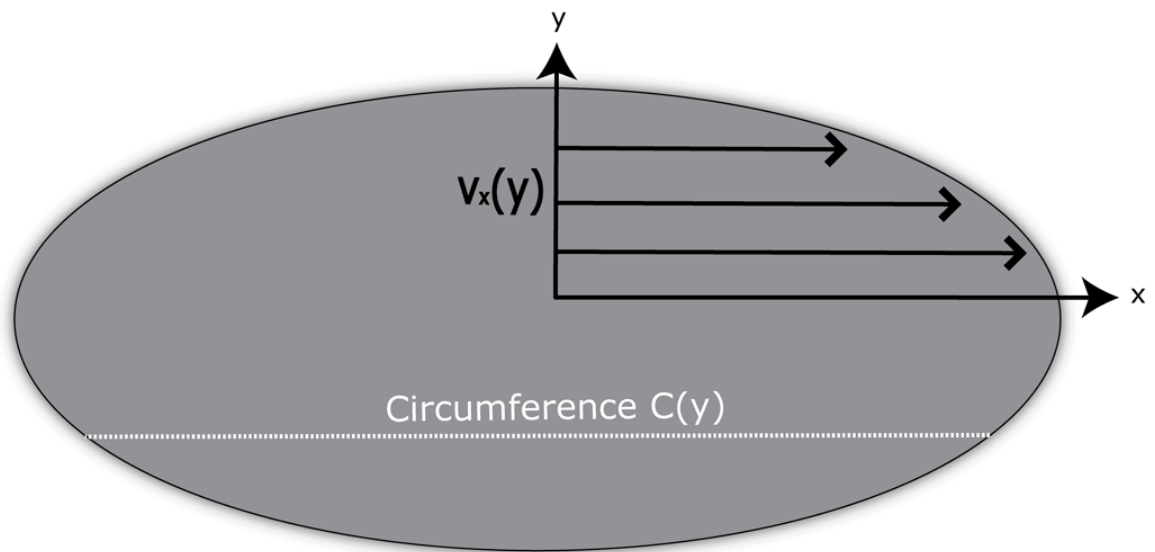


Figure 3.14: Velocity components in the red blood cell membrane (seen from above) according to Fischer: $v_x = fC(y)$ and $v_y = 0$ where f is the tank-tread frequency.

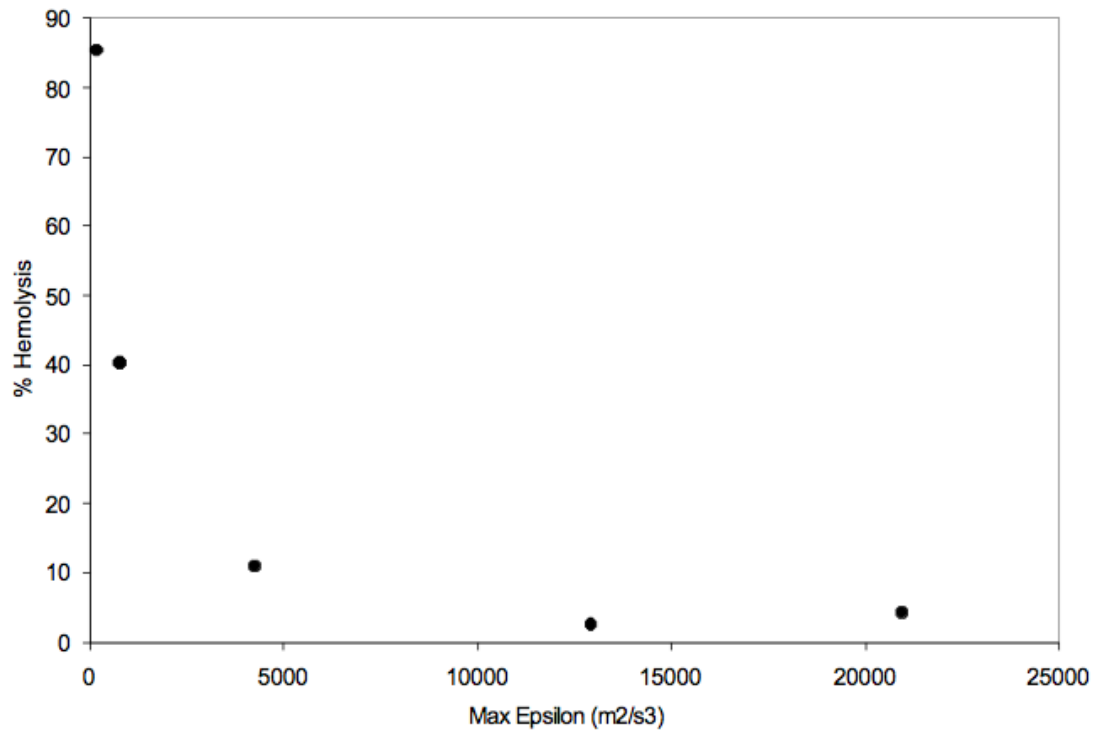


Figure 3.15: Percent hemolysis versus maximum rate of turbulent kinetic energy dissipation on the threshold iso-surface (i.e. percent volume isolated by iso-surface = percent hemolysis). No threshold value for ϵ is apparent.

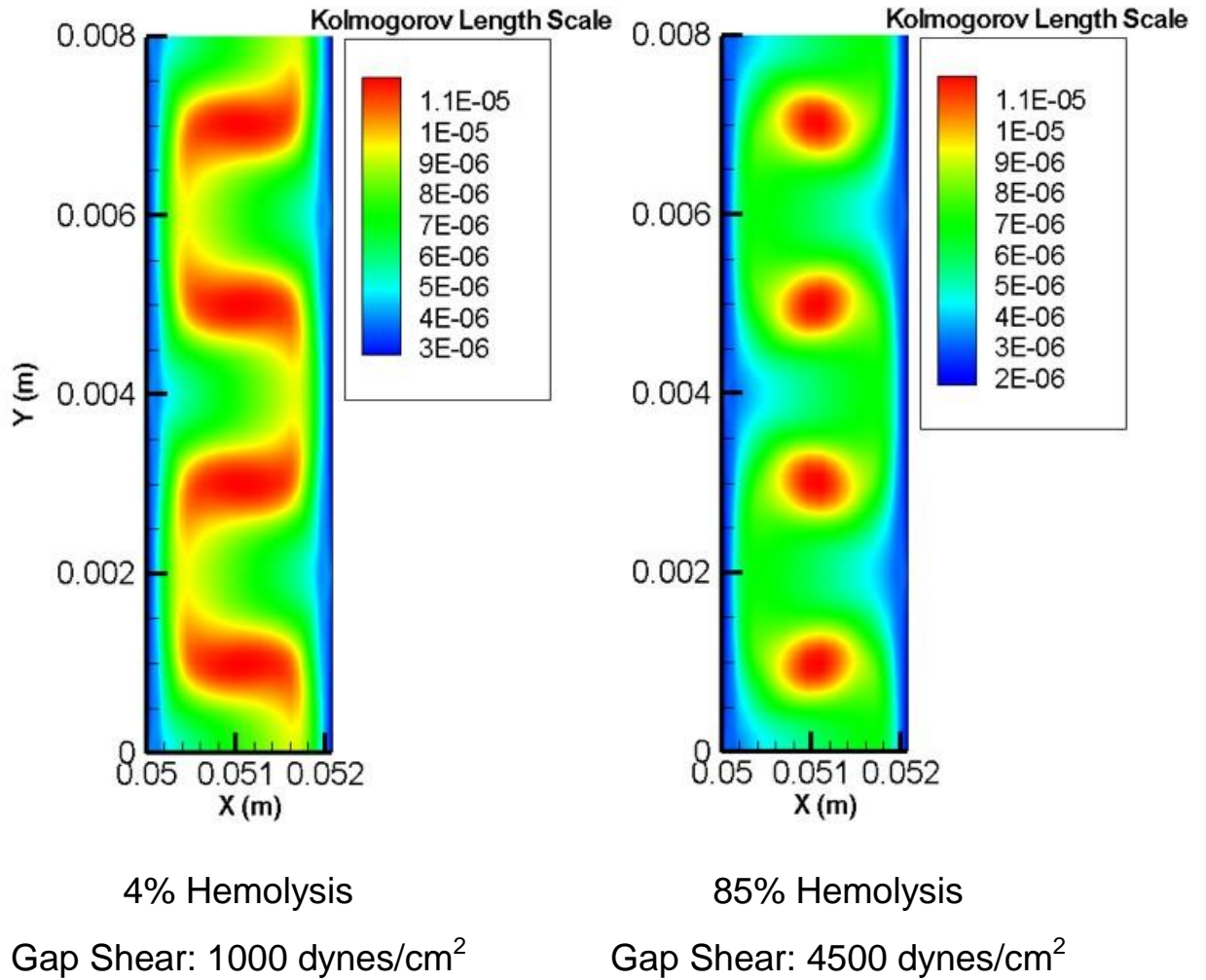


Figure 3.16: Kolmogorov Length Scales for two gap shear values and, correspondingly, two levels of hemolysis. Length scales of the size of a RBC are found at both rotational rates, with a larger portion of the flow exposed to smaller KLS in the case with more hemolysis.

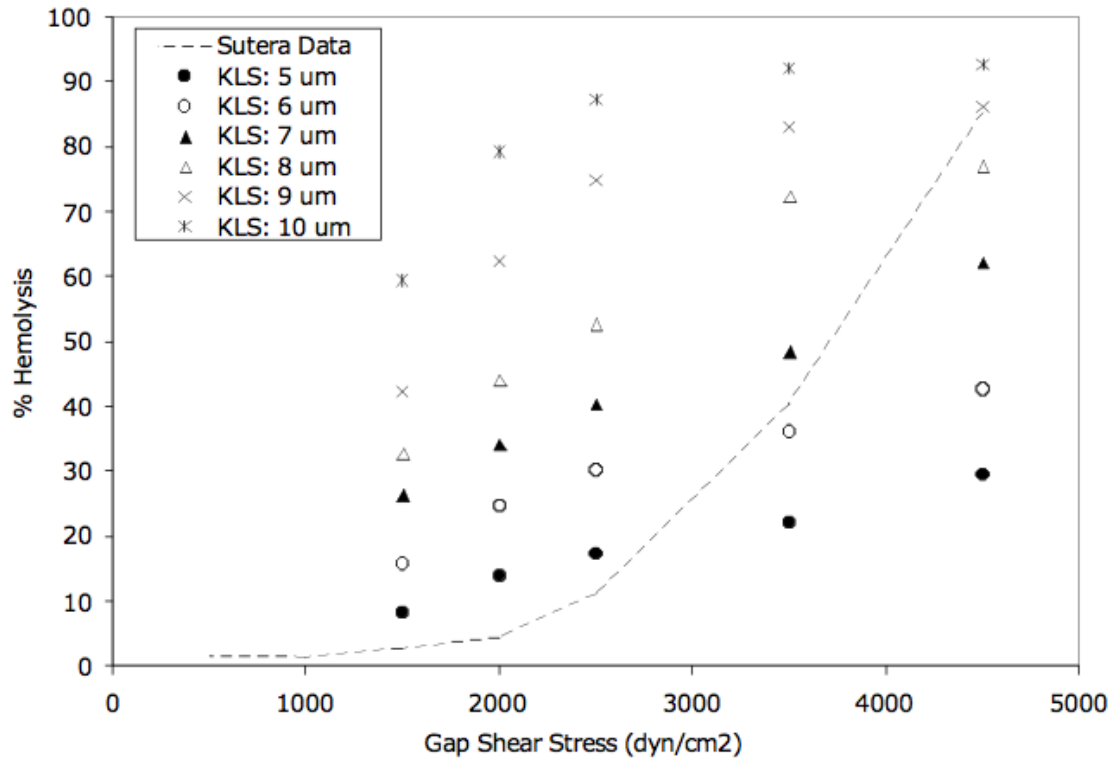


Figure 3.17: Percent hemolysis/Percent volume isolated by KLS iso-surface versus gap shear stress. If a threshold KLS were evident, Sutera's data would fall on the same curve as the data points for one of the Kolmogorov Length Scales, however it does not.

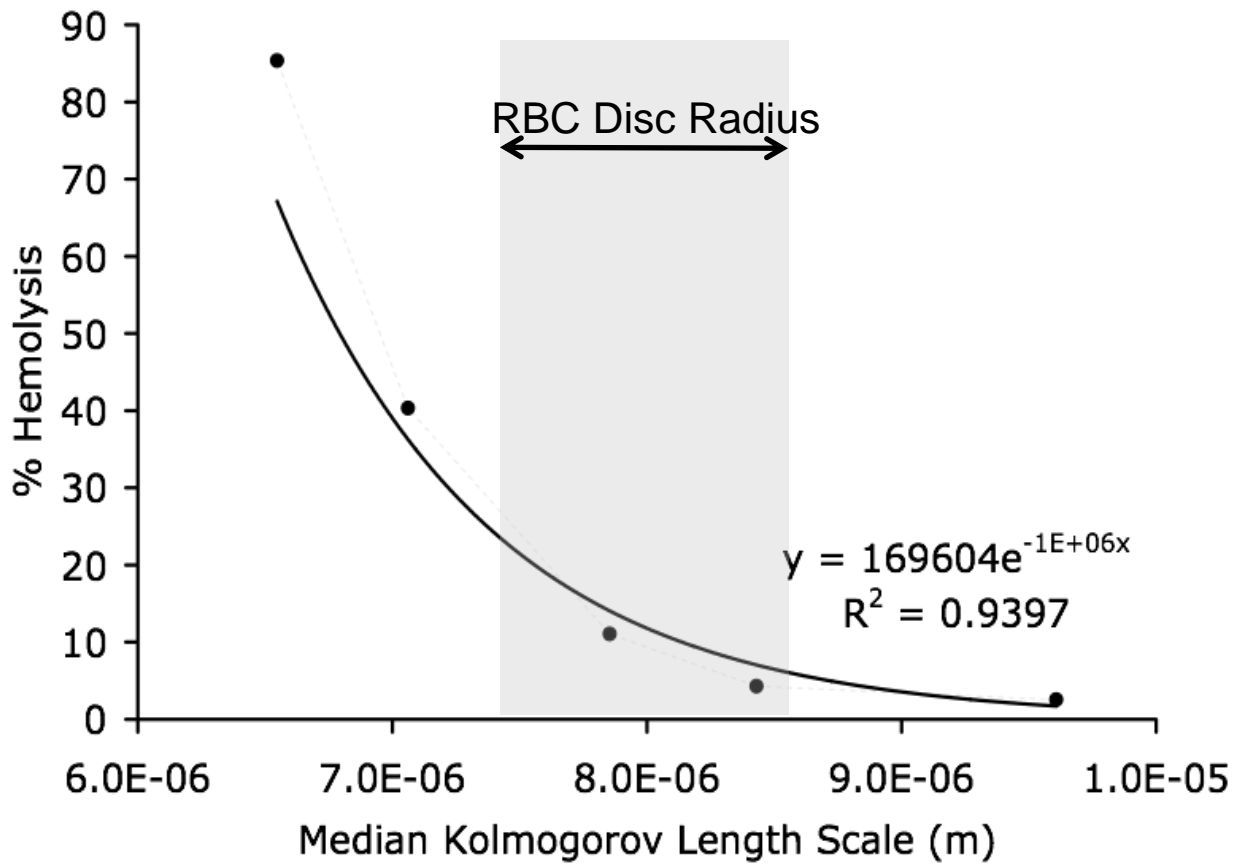


Figure 3.18: Percent hemolysis versus median Kolmogorov Length Scale. The plot shows a dependence of hemolysis on median KLS, with smaller median KLS values indicating more hemolysis. The size range for a RBC is shown for comparison.

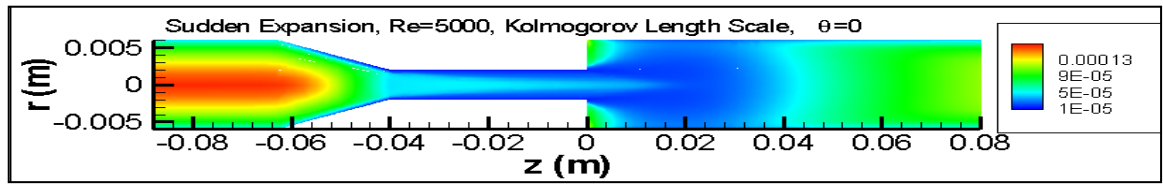


Figure 3.19: Kolmogorov Length Scales for the FDA CPI nozzle geometry in the sudden expansion orientation, at $Re = 5000$. Kolmogorov Length Scales on the same order of magnitude as the size of a RBC are seen.

Contraction Ratio	Viscosity (Pa s)	Re Number	Experimental % Hemolysis	Maximum τ_{xz} (Pa)	Maximum τ_{xy} (Pa)	Maximum τ_{yz} (Pa)
<i>Sharp Contraction</i>						
27:1	0.005	706	5.9	2868	2969	4280
27:1	0.005	844	9.7	2697	3108	4235
27:1	0.005	931	11.4	2698	3343	4110
27:1	0.005	1056	16.1	2791	3423	3531
27:1	0.005	846	8.4	2559	2338	3645
2:1	0.005	924	6.3	3173	2673	3658
2:1	0.005	1011	7.1	3124	2745	5154
2:1	0.005	1126	12.9	3062	3825	4357
2:1	0.005	1227	15.0	2863	3551	3892
3:1	0.005	874	8.9	2855	3520	4562
3:1	0.005	1028	12.8	3413	4164	4186
3:1	0.005	1108	15.6	3252	3996	3752
3:1	0.005	1257	22.0	2907	3681	2895
27:1	0.013	200	11.1	2205	2530	3396
27:1	0.013	247	22.1	2577	3503	2995
27:1	0.013	307	32.9	2658	3681	2446
27:1	0.013	362	41.5	2521	3621	2081
27:1	0.013	406	48.2	2356	3506	2224
<i>Tapered Contraction</i>						
3:1	0.005	1070	1.1	2788	2659	2029
3:1	0.005	1173	1.9	2610	2325	3342
3:1	0.0013	411	9.7	3042	3038	4621

Table 3.1: Summary of simulation parameters and results. Capillary diameter - 0.035 cm. Maximum - maximum value on threshold streamline.

CHAPTER 4: RENAL ARTERY STENOSIS

4.1 Introduction to Stenoses

The effect of a stenosis on pressure loss has been studied in geometries similar in size to renal artery stenosis, resulting in empirical equations put forth by Young et al. and Shalman et al. (as modified by Yim, et al.) for steady flows. Young et al. developed the following correlation, which relates the pressure drop across a stenosis to blood vessel dimensions, flow characteristics, and coefficients dependent on stenosis geometry (Young, 1979):

$$\frac{\Delta p}{\rho U_o^2} = \frac{K_v}{\text{Re}} + \frac{K_t}{2} \left[\frac{A_o}{A_1} - 1 \right]^2 \quad (4.1)$$

where Δp is the pressure drop across the artery, ρ is the density of blood, U_o is the average blood velocity in the unobstructed artery, K_v and K_t are coefficients dependent on stenosis shape and geometry, Re is the Reynolds number in the unobstructed artery, A_o is the cross-sectional area of the unobstructed artery, and A_1 is the minimum cross-sectional area. Young et al. state that the coefficients K_v and K_t can be determined for different geometries by fitting experimental pressure drop measurements using a least squares regression. For the blunt plug stenosis geometry studied by Young et al., the average K_t is 1.52, and K_v is given by the following equations (Young, 1979):

$$K_v = 32 \frac{L_a}{D} \left(\frac{A_o}{A_1} \right)^2 \quad (4.2)$$

$$L_a = 0.83L_s + 1.64D_1 \quad (4.3)$$

Where D is the unobstructed artery diameter, L_s is the stenosis length, and D_1 is the minimum diameter. Seeley and Young applied the above correlation to previous data

from a smooth stenosis and found that good agreement was achieved if the correlation was modified by replacing the term A_0/A_1 with A_0/A_{1a} (Seeley, 1976):

$$\frac{A_0}{A_{1a}} = 0.75 \frac{A_0}{A_1} + 0.25 \quad (4.4)$$

The Reynolds number used in the arterial simulations was 675, within the range of Young's correlation, which was developed for a Reynolds number range from approximately 50 to 1000.

An additional correlation was developed by Yim et al. The following equations give the pressure drop estimation used by Yim et al. which is a modified version of that proposed by Shalman (Yim, 2004).

$$\Delta P = \frac{1}{2} \frac{\rho Q^2}{A_0^2} \left[\left(\frac{A_0}{A_1} \right)^2 - 1 \right] + \frac{128}{\pi} \frac{\rho \nu}{d_l^4} L_{1-2} I_{1-2} Q + \beta \frac{\rho Q^2}{A_1^2} \frac{A_1}{A_3} \left[1 - \frac{A_1}{A_3} \right] \quad (4.5)$$

$$I_{1-2} = \frac{(D/D_1)^3 - 1}{3(1 - D_1/D)} \quad (4.6)$$

where Q is the blood volumetric flow rate, A_0 and A_1 are defined as above, A_3 is the cross-sectional area of the artery distal to the stenosis, ν is the kinematic viscosity of blood, L_{1-2} is the length of the converging section of the artery, I_{1-2} is a shear force integral defined by equation (9), and β is a coefficient between 0.85 and 1. In contrast to the Young model, these expressions apply for a stenosis of an axisymmetric, conic converging and diverging shape.

4.2 Renal Artery Stenosis Geometries and Computational Domains

4.2.1 Stenosis Geometries

Three types of stenosis geometries were studied – a blunt stenosis to mimic Young’s work, a conical stenosis to mimic Yim’s work, and an elliptical stenosis (as a better model of physiologically realistic stenoses). The geometries considered are shown in Figure 1.4. The length of the renal artery for all cases was 50 mm, the diameter was 5 mm, and the length of the stenosis was 5 mm in all simulations except in the study of stenosis length, in which the length was varied from 2.5 to 5 mm.

4.2.2 Computational Domain

4.2.2.1 Boundary Conditions

The model parameters of artery diameter and flow rate were chosen to be comparable to a typical renal artery (Kem, 2005). Simulation conditions were steady, laminar or turbulent flow (determined based on a critical Reynolds number), with a total blood flow rate of 10 mL/s. The critical Reynolds number for transition to turbulent flow was related to the Reynolds number in the un-occluded artery and the percent occlusion, based on the data of Azuma and Fukushima (Azuma, 1976). The artery was modeled with rigid walls, which is not representative of arterial walls in general, but may be used in the case of stenosis, in which the artery wall is stiffened (Giannattasio, 2001; Bortolotto, 1999; London, 2005).

The fluid specified was blood, with a viscosity of 0.004 Pa s and a density of 1060 kg/m³. The blood was assumed to be Newtonian, which is a common assumption (Perktold, 1991; Frauenfelder, 2006; Ku, 1997) for vessels that are large compared to the size of a red blood cell (Nguyen, 2008; Yamaguchi, 2006). The symmetric stenoses were

modeled using the 2D axisymmetric solver in order to simplify the calculations and save computational time. In addition to the 2D steady flow simulations, additional simulations were performed using a pulsatile velocity profile at the inlet in order to compare transient results to those found with steady flow. 3D simulations were used, first, to investigate the effect of eccentricity (the deviation of the center of the stenosis from the centerline of the artery) and, secondly, the effect of the axial location of the stenosis when the entire system (abdominal aorta, renal arteries, renal artery branches) is taken into account. For 2D simulations, the inlet boundary condition was specified as a constant velocity and the outlet boundary condition was specified as an outflow condition. For 2D transient simulations, the inlet boundary condition was given as the pulsating velocity profile taken from Skalak and Chien (Skalak, 1987), and the outlet was specified as an outflow. For 3D simulations of only the artery, the same steady flow boundary conditions used in 2D were set; however, for 3D simulations that included a section of abdominal aorta, the renal arteries, and first generation renal artery branches, the inlet condition was a mass flow rate (88.3 g/s) and the outlets were all given outflow conditions with the constraint that 10.6 g/s passed through each one of the two renal arteries. See Figure 4.1 for an illustration of the 3D system geometry.

4.2.2.2 Grid

For both 2D and 3D simulations, the geometry and mesh were created in Gambit 2, then imported into Fluent 6 for simulation. For 2D simulations, each mesh was created as a quadrilateral grid. For 3D simulations, all grids were hexahedral. Each grid was refined in regions of high velocity gradient and then refined globally until the percent difference for the pressure loss and velocity profile at multiple cross sectional cuts

between a more and less refined simulation solution was less than 3%. In addition, the outlet boundary condition was changed in order to verify that the solution was independent of this condition; the simulation solution did not change when the outlet boundary condition was varied.

4.3 Two-Dimensional Steady Flow Results

The pressure loss along the length of the artery was calculated as the absolute value of average pressure at the artery outlet minus average pressure at the artery inlet. The pressure loss for an artery as described above but lacking any constriction was modeled using the 2D, axisymmetric, laminar solver, in order to validate the simulations for the most basic geometry. Excellent agreement between these simulations and theoretical pressure loss for tube flow prompted the extension of the simulation conditions to more complicated geometries.

4.3.1 Effect of Stenosis Axial Position

The effect of the stenosis axial location on the pressure loss through an artery was investigated in two ways. First, a long artery was modeled and given a flat entrance velocity profile, which was allowed to fully develop before reaching the end of the artery through the inclusion of a sufficient entrance length. The axial location of an 80% stenosis ($\% \text{ stenosis} = 1 - D_1^2/D^2$) was varied along the length of the artery so that the flow entering the stenosis varied from a flat velocity profile to a fully developed, parabolic profile. The results of these simulations showed no dependence of pressure loss on the development of flow at the stenosis entrance. The variation of axial position was then reexamined by introducing the abdominal aorta and the main renal artery branch

into the system, thus giving the model a more realistic entrance velocity profile as well as outlet conditions (Figure 4.1). The results of these simulations indicated only a slight dependence of pressure loss on axial position, from 24.6 to 22.2 mm Hg, for an 80% stenosis, and none for the less severe cases studied (Figure 4.2). Varying the stenosis length from 2.5 mm to 5 mm had a similarly small effect on the pressure loss across the stenotic artery, changing the value only up to 10% of the total pressure loss, or 2 mm Hg.

The simulations investigating the effect of stenosis axial location on pressure loss led to two interesting results. The first, indicated by simulations of a long, straight artery, is that the development of flow does not have an effect on the pressure loss through the artery. For these simulations, the stenosis was placed close to the entrance of the artery where the flow profile is still generally flat and then moved progressively farther from the entrance until the stenosis was situated beyond the entrance length for the artery, at which distance the flow is fully developed. No significant difference in the pressure loss through the artery was seen for the developing and fully developed regions.

Secondly, the model was extended to include the abdominal aorta, the renal arteries, and the main renal artery branches, in order to create more physiologically realistic entrance and outlet conditions. The axial position of a stenosis along the renal arteries was then varied. The results of these simulations show that as the stenosis is moved farther from the artery inlet, and thus closer to the artery branch, the pressure loss decreases only slightly. The blood velocity profile at the entrance of the renal artery for these simulations was significantly different than that for a straight renal artery with a flat velocity profile. Given the artery length, however, the flow is not allowed to develop before the entrance to the renal artery branches, so it may be that the decrease in pressure

loss is due to end effects rather than the velocity profile, such as truncation of the stenosis jet when the stenosis is near the artery branch.

4.3.2 Effect of Stenosis Shape and Percent Stenosis

Simulations with stenoses ranging from 45-90% stenosis were modeled in order to investigate the critical percent stenosis associated with malfunction of the renin-angiotensin-aldosterone system in the kidney. Three geometries were modeled; an elliptical stenosis, a blunt stenosis mimicking Young's geometry, and a conical stenosis mimicking Shalman's geometry. Figure 4.3 shows that as the percent stenosis increases, the pressure loss across the artery increases and that the threshold for hemodynamic relevance (i.e., $\Delta P > 10$ mm Hg) is reached for percent stenosis greater than approximately 75%.

The results of simulating all three geometries at the critical stage of occlusion show that the blunt geometry gives a consistently higher pressure loss than the other two structures, followed by Shalman's structure, with the elliptical structure giving the lowest pressure losses as a function of percent stenosis (Figure 4.3).

A goal of this work was to probe the "rule of thumb" regarding the critical percent stenosis to ascertain pathologically relevant pressure losses in the renal artery. This rule of thumb has been found to be approximately 75-80% stenosis, and some studies have indicated a difference in patient outcome for those suffering from severe (75-80%) stenosis compared to moderate stenosis (Balk). In addition to this critical percent stenosis, an average pressure drop of 10 mm Hg is commonly given as the threshold for physiologically relevant pressure loss in the renal artery; this value was verified through this work. From Figure 4.3, it is apparent that the threshold pressure loss of 10 mm Hg is

reached at approximately 75% stenosis, and that the range of critical percent stenosis is marked by a dramatic increase in arterial pressure loss. This result serves to confirm both the percent stenosis “rule of thumb” as well as the threshold pressure loss, both used by physicians.

The simulation results for the geometries of Young and Shalman give similar values and follow the same trend as the calculated values from their respective correlations. The discrepancy between the simulation results for Young’s geometry compared to the theoretical results could be due to the nature of the constant K_t , which is an average value derived from experiments using multiple stenosis geometries and ranges from 1.52 to 1.83 depending on the geometry used. The simulation results consistently gave a larger pressure drop than Young’s correlation for a blunt stenosis, with the discrepancy becoming larger after the critical percent stenosis is reached and achieving a maximum of 60 mm Hg at 90 percent stenosis. Shalman’s correlation also gives a smaller pressure loss through a conical stenosis when compared to the computed results, although the difference is less for this correlation with a maximum discrepancy of 10 mm Hg. The best agreement was found when comparing the elliptical stenosis to Young’s correlation using the modified area term for smooth stenoses. This result strengthens the conclusion that the area reduction of a stenosis is the most significant parameter for predicting pressure loss.

When the results of the blunt stenosis, conical stenosis and an elliptical stenosis are compared in Figure 4.3, it is evident that the stenosis structure has an effect on pressure loss. The dependence of pressure loss on stenosis structure is not surprising when one considers known effects of constriction geometry from classical fluid

mechanics. For example, the pressure loss measured across an orifice plate will be higher than that across a Venturi meter of the same minimum diameter, because of the fluid behavior in a tapered constriction (Venturi meter) as opposed to a sharp contraction (orifice plate). Typically, the severity of a stenosis is given by the percent stenosis based on the area of occlusion as calculated at the narrowest point of the constriction. This, however, does not capture the difference in pressure losses occurring due to a gently converging conical stenosis (Shalman) compared to the sudden contraction of the blunt stenosis (Young). By characterizing a stenosis by percent occlusion only, a significant amount of information about the possible pressure losses due to the stenosis is lost. The results in Figure 4.3 help to emphasize this point. There is little question that a physician should intervene for the blunt geometry, while it is less clear in the case of the other stenosis structures. One can conclude that the variation in structure for commonly occurring arterial stenoses is significant through visual examination of patient images (e.g., MRI) from multiple stenosis case studies (Douis, 2008; Pheiffer, 2004; Han, 2005; Serter, 2007), and that description of stenosis severity based only on percent stenosis is insufficient.

4.4 Two-Dimensional Time-Dependent Results

4.4.1 Effect of Stenosis Shape on Peak Pressure Loss

Results from these steady flow simulations were also compared to the results for pulsatile blood flow. This was done in order to establish that using steady flow, as opposed to pulsatile flow, would still lead to correct conclusions. The results of simulating a 75% occluded elliptical, a 75% occluded Shalman-type and a 75% occluded

Young-type stenosis using a pulsatile inlet velocity are shown in Figure 4.4. From this plot it is evident that the use of a pulsatile inlet condition leads to the same conclusions as using a steady flow: that hemodynamically significant pressure losses are present at 75% occlusion and that the stenosis structure has a significant impact on the pressure loss with the blunt stenosis being the most severe. Comparing, for example, the peak pressure drops for either the steady or unsteady computation, we find the Shalman structure to have a slightly higher pressure drop peak than the elliptical structure, both of which are about half the loss for the blunt geometry examined by Young. This comparison confirms that the use of steady flow in other simulations yields reliable results.

4.5 Three-Dimensional CFD Results – Effect of Stenosis Eccentricity

The effect of stenosis eccentricity was investigated using a 3D model also (Figure 4.5). Eccentricity is the degree to which a stenosis is non-symmetric in the axial plane. Here, eccentricity is defined as the distance between the stenosis axial center and the artery axial center divided by the stenosis radius. This definition means the upper limit of eccentricity increases with the extent of occlusion. In other words, the smaller the stenotic lumen, the closer its center can approach the wall of the artery. The simulations carried out were for a 50% and an 80% occluded elliptical stenosis. The results of varying the degree of asymmetry for these stenoses showed that there was no dependence on eccentricity (Figure 4.6).

The investigation of the effect of stenosis eccentricity did not show a dependence of the pressure loss through an artery on this parameter. This result serves to indicate that the principal cause of increased pressure loss by a stenosis is through the reduction of the

area available to flow. The percent stenosis is the governing parameter for stenosis severity when referring to pressure losses.

4.6 Conclusions

The process of atherosclerosis causes the formation of plaques in the circulatory system that lead to a variety of cardiovascular diseases. Computational fluid dynamics has been used to increase our understanding of the deposition process in coronary arteries (Wada, 2002) and the effects of flow through stenoses in the coronary, carotid and renal arteries. Alteration of flow in the renal artery causes a pressure loss that sabotages the hormonal control of the systemic blood pressure by the kidney. Clearly, the hemodynamic effects of altered artery geometry can have a significant impact on health, and an increased understanding of these effects is important.

CFD offers a powerful and versatile alternative to physical flow field experimentation, and has proved an acceptable method for modeling arterial stenoses. The results obtained in this study through simulation were reasonable and displayed good agreement with expected theoretical trends. The pressure loss through a renal artery, modeled along with the aorta and renal branches, is related only slightly to the axial position of the stenosis along the artery – decreasing as the stenosis is moved farther away from the artery entrance by approximately 10% of the maximum pressure loss. This dependence was not, however, seen for a single straight artery. It was shown that the eccentricity of a stenosis does not have an effect on the pressure loss, indicating that the percent stenosis is the most significant parameter for stenosis severity. Additionally, investigation of the relationship between percent stenosis and arterial pressure loss

indicates a critical percent stenosis for the renal artery of approximately 75%. This critical percent stenosis is indicated by a pressure loss consistent with the threshold hemodynamically relevant average pressure loss of 10 mm Hg previously proposed as well as a drastic increase in pressure loss for percent stenosis $> 75\%$. The pressure losses across a stenotic artery were also found to depend on the structure of the stenosis. When comparing conical, blunt, and elliptical structures, it was found that the blunt structure led to a higher pressure loss and that this discrepancy is exacerbated once the critical percent stenosis is reached. Percent occlusion appears to have a more significant impact on the pressure loss than structure, however – for the most severe case, a 10% increase in percent stenosis leads to a four-fold increase in pressure loss but for the highest percent occlusion a change in structure leads to only a two-fold increase in pressure loss. Clearly, there is a critical degree of occlusion for a renal artery stenosis, but other factors including immediate stenosis structure are important.

Portions of this chapter have been reproduced from the following sources:

Heflin LA, Street CB, Papavassiliou DV, O’Rear EA. *A Computational Investigation of the Geometric Factors Affecting the Severity of Renal Arterial Stenoses*. Journal of Biorheology. 2009; 23: 102-110.

4.7 Nomenclature

A_0 – cross-sectional area of unobstructed artery

A_1 – minimum cross-sectional area

A_3 – cross-sectional area of artery distal to stenosis

D – unobstructed artery diameter

D_1 – minimum diameter

I_{1-2} – shear force integral

K_v and K_t – coefficients dependent on stenosis shape and geometry

L_{1-2} – length of the converging section of the artery

L_s – stenosis length

Q – blood volumetric flow rate

Re – Reynolds number

U_0 – average blood velocity in the unobstructed artery

β - coefficient between 0.85 and 1

Δp – the pressure loss across the artery

ν - kinematic viscosity of blood

ρ - density of blood

4.8 References

Azuma T, Fukushima T. Flow Patterns in Stenotic Blood Vessel Models. *Biorheol* 1976; 13: 337-355.

Balk E, Raman G, Chung M, Ip S, Tatsioni A, Alonso A, Kupelnick B, Chew P, DeVine D, Gilbert S, Lau J. Comparative Effectiveness of Management Strategies for Renal Artery Stenosis. In: Comparative Effectiveness Review No. 5. Rockville, MD: Agency for Healthcare Research and Quality.

Bortolotto L, Safar M, Billaud E, Lacroix C, Asmar R, London G, et al. Plasma Homocysteine, Aortic Stiffness, and Renal Function in Hypertensive Patients. *Hypertens* 1999; 34: 837-842.

Douis H, Shabir S, Lipkin G, Riley R. Drug-eluting stent insertion in the treatment of in-stent renal artery restenosis in three renal transplant recipients. *J Vasc Interv Radiol* 2008; 19: 1757-1760.

Frauenfelder T, Lotfey M, Boehm T, Wildermuth S. Computational fluid dynamics: hemodynamic changes in abdominal aortic aneurysm after stent-graft implantation. *Cardiovasc Intervent Radiol* 2006; 29:613-623.

Giannattasio C, Failla M, Emanuelli G, Grappiolo A, Boffi L, Corsi D, et al. Local Effects of Atherosclerotic Plaque on Arterial Distensibility. *Hypertens* 2001; 38: 1177-1180.

Han M, Criado E. Renal artery stenosis and aneurysms associated with neurofibromatosis. *J Vasc Surg* 2005; 41: 539-543.

Ku D. Blood Flow in Arteries. *Annual Review of Fluid Mechanics* 1997; 29:399-434.

London G, Marchais S, Guerin A, Pannier B. Arterial stiffness: pathophysiology and clinical impact. *Clin Exp Hypertens* 2005; 26: 689-699.

Nguyen K, Clark C, Chancellor T, Papavassiliou DV. Carotid geometry effects on blood flow and on risk for vascular disease. *J Biomech* 2008; 41:11-19.

Perktold K, Resch M, Peter R. Three-dimensional numerical analysis of pulsatile flow and wall shear stress in the carotid artery bifurcation. *J Biomech* 1991; 24:409-420.

Pheiffer T, Müller B, Huber R, Reiher L, Häfele S, Sandmann W. Management of Patients with Renal Artery Stenosis. *Herz* 2004; 29: 76-89.

Serter S, Oran I, Parildar M, Memiş A. Fibromuscular dysplasia-related renal artery stenosis associated with aneurysm: successive endovascular therapy. *Cardiovasc Intervent Radiol* 2007; 30: 297-299.

Shalman E, Barak C, Dgany E, Noskowitz H, Einav S, Rosenfeld M. Pressure-based simultaneous CFR and FFR measurements: understanding the physiology of a stenosed vessel. *Comput Biol Med* 2001; 31:353-363.

Skalak R, Chien S. *Handbook of Bioengineering*. New York: McGraw-Hill, 1987.

Wada S, Karino T. Theoretical Prediction of Low-Density Lipoproteins Concentration at the Luminal Surface of an Artery with a Multiple Bend. *Ann Biomed Eng* 2002; 30: 778-791.

Yamaguchi T, Ishikawa T, Tsubota K, Imai Y, Nakamura M, Fukui T. Computational Blood Flow Analysis - New Trends and Methods. *J Biomech Sci Eng* 2006; 1:29-50.

Yim P, Cebra J, Weaver A, Lutz R, Soto O, Vasbinder B, Ho V, Choyke P.
Estimation of the differential pressure at renal artery stenoses. *Magn Reson Med*
2004; 51:969-977.

Young D. Fluid Mechanics of Arterial Stenoses. *J Biomech Eng* 1979; 101:185-
196.

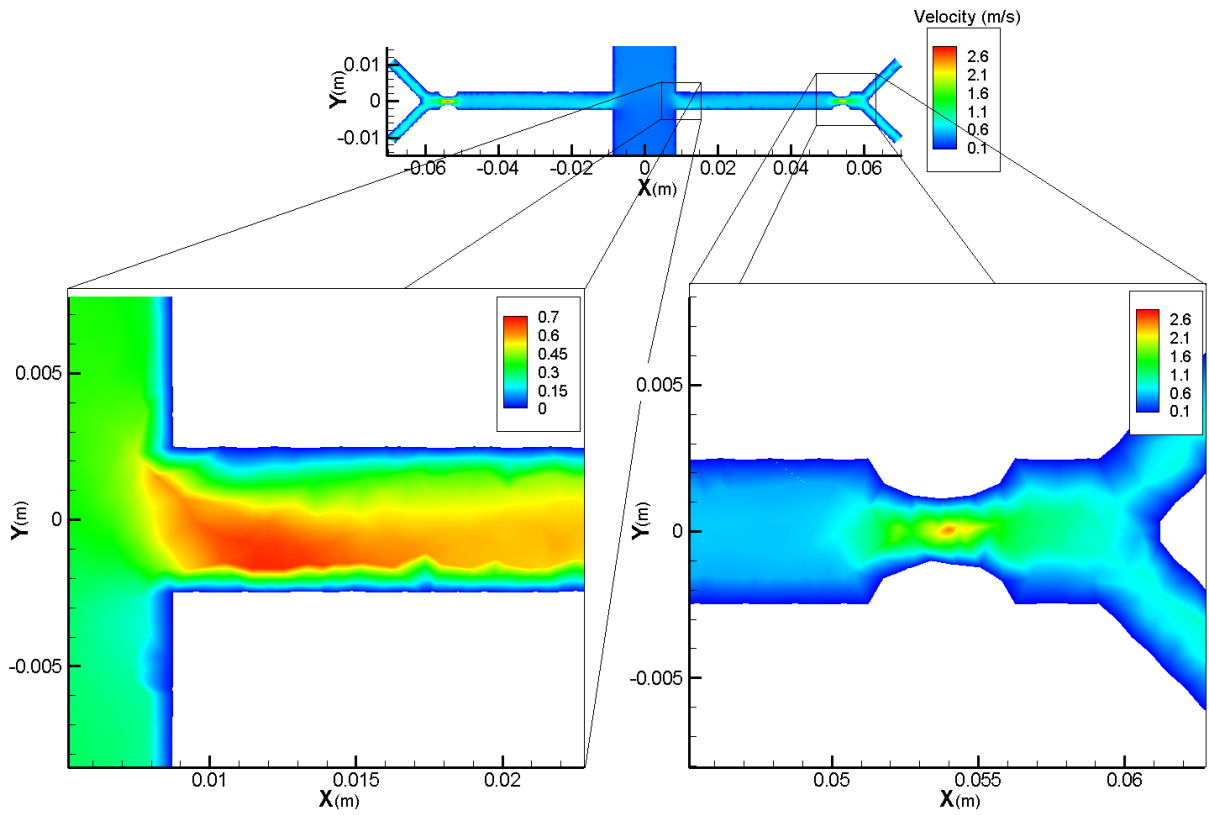


Figure 4.1. 3D model of abdominal aorta, renal arteries and renal branches with an 80% stenosis located at 0.9 normalized axial position. The insets show the velocity profile as blood enters the renal artery from the abdominal aorta and the velocity profile in and immediately after the stenosis. The velocity profile entering the renal artery is drastically different from the flat velocity profile given in previous, renal artery only simulations.

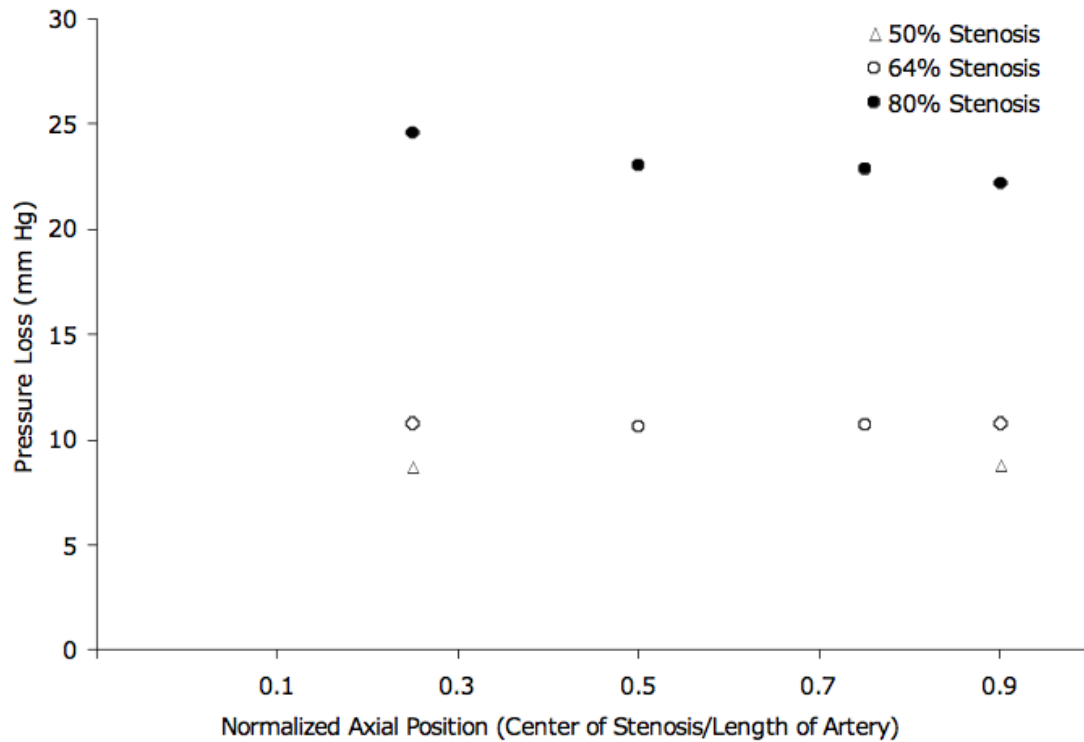


Figure 4.2. Pressure loss versus axial location for a renal artery. In this system, the abdominal aorta, the renal arteries, and the main renal artery branch are simulated in order to achieve a more realistic inlet velocity profile and outlet conditions. Simulation conditions are: steady flow; elliptical stenosis; blood viscosity, 0.004 Pa s; blood density, 1060 kg/m³; blood flow rate through renal artery, 10 mL/s; renal artery diameter, 5 mm; renal artery length, 50 mm; for 50% stenosis, laminar model; for 64% and 80% stenosis, turbulent k-ε model.

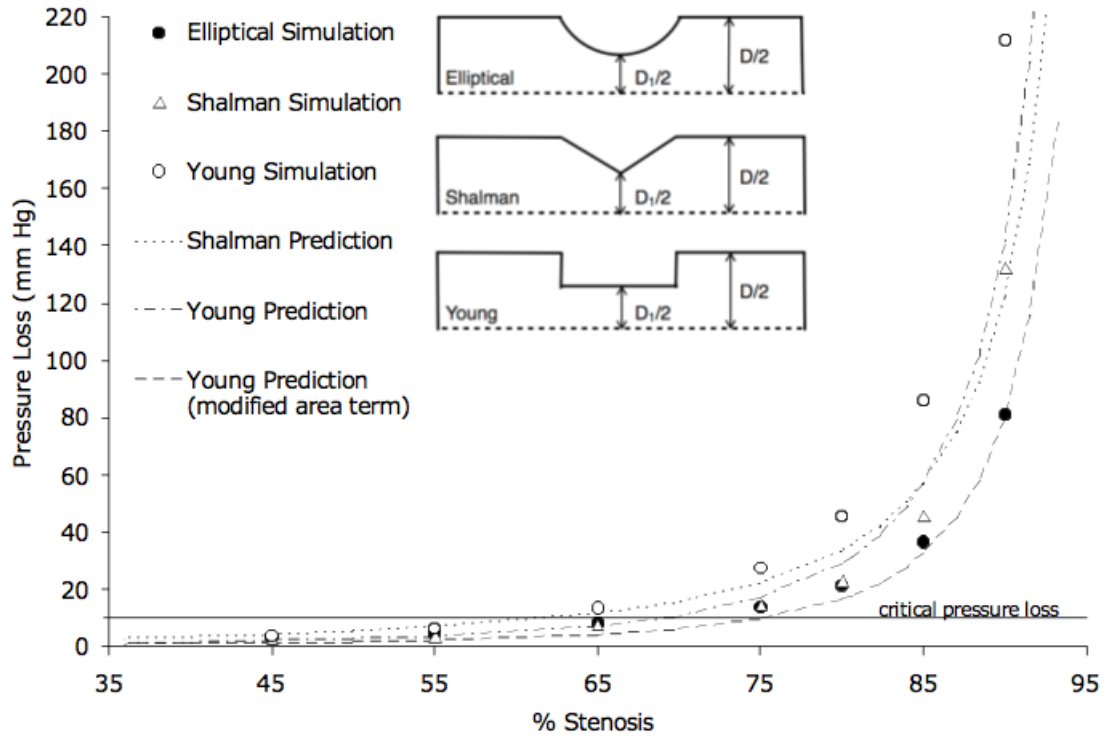


Figure 4.3. Pressure loss versus percent stenosis. Results show a clear critical percent occlusion near 75% stenosis. Simulation conditions are: steady flow; blood viscosity, 0.004 Pascal second; blood density, 1060 kg/m³; blood flow rate through renal artery, 10 mL/second; up to 50% stenosis, laminar model; higher than 50% stenosis, turbulent k- ϵ model.

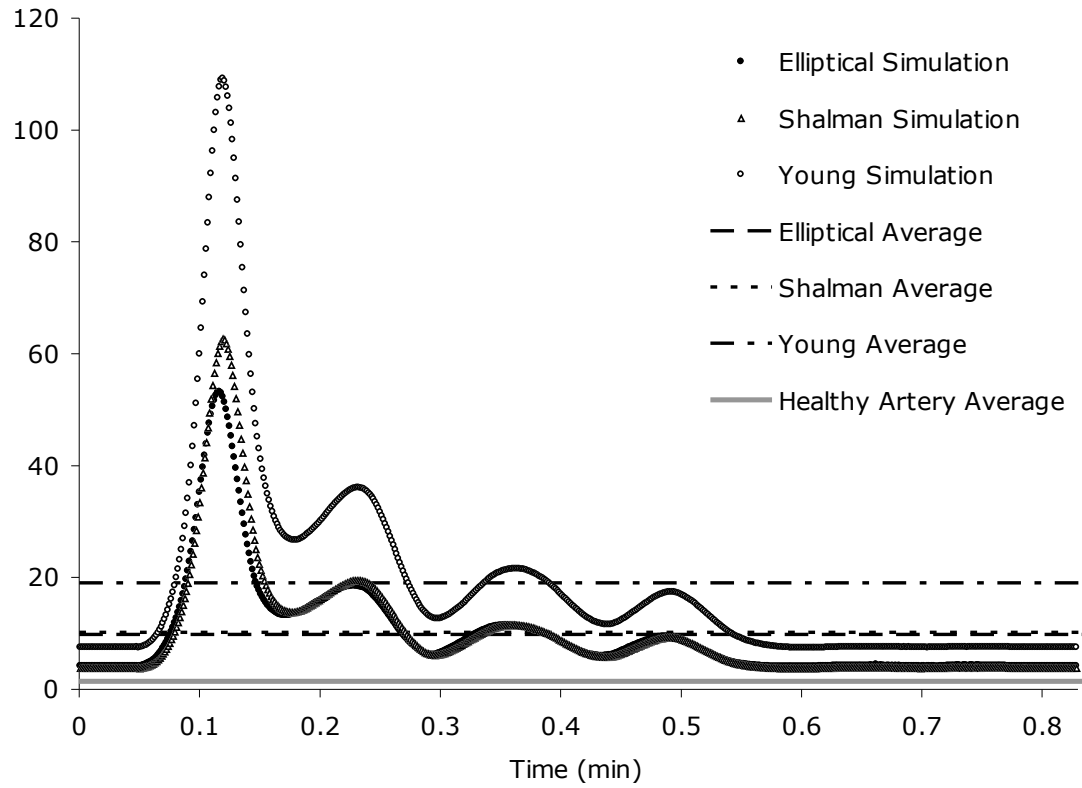


Figure 4.4. Pressure loss versus time for one pulse. Results show that hemodynamically significant pressure loss occurs for a 75% stenosis and that the stenosis structure is important in determining the pressure loss across a constriction. Simulation conditions are: unsteady flow; blood viscosity, 0.004 Pascal second; blood density, 1060 kg/m³; 75% stenosis; turbulent k-ε model.

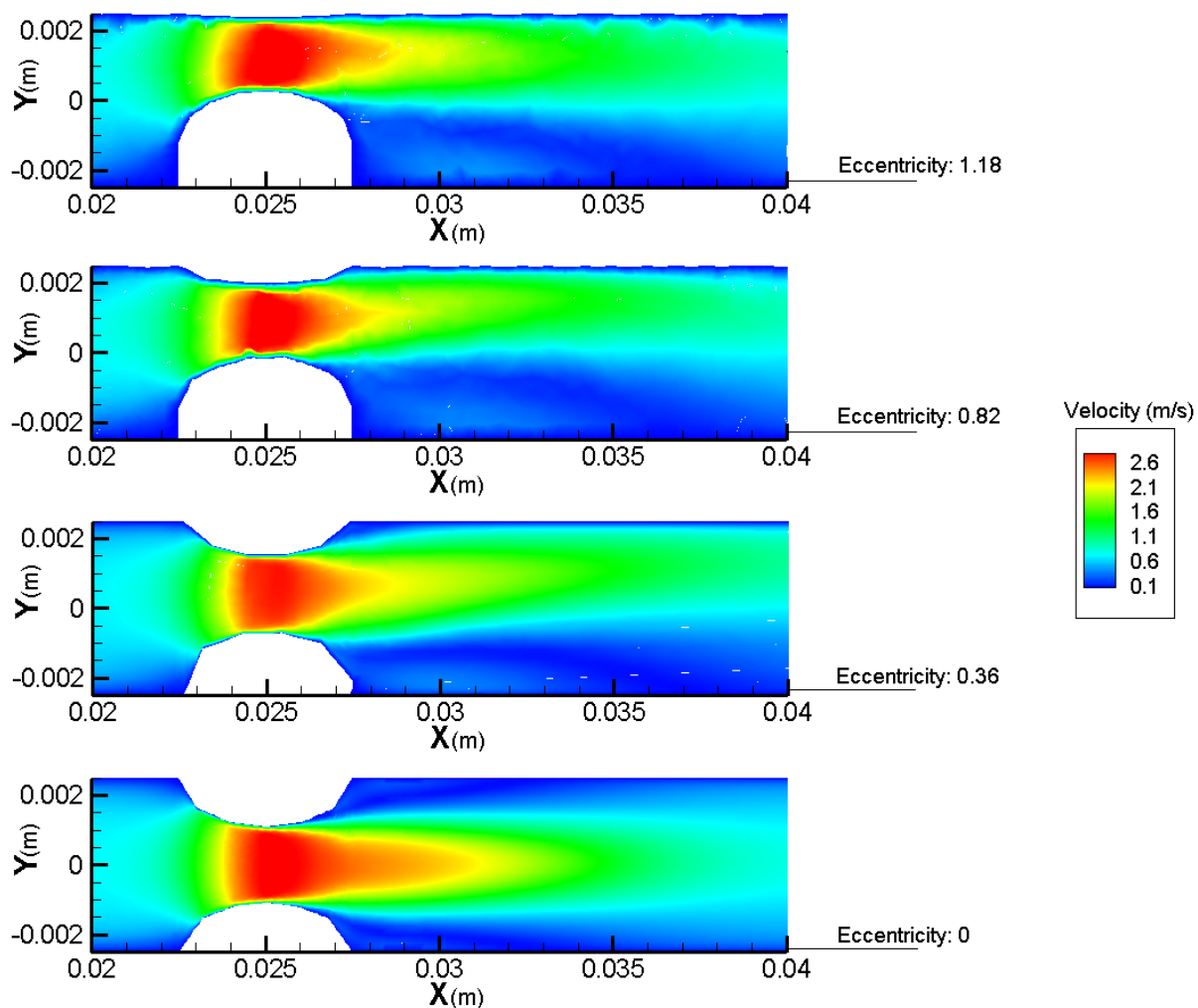


Figure 4.5. Velocity profiles in and immediately following an 80% stenosis placed at the center of a 5 cm renal artery. Starting from the top image, the stenosis is moved progressively closer to the center of the artery in these 3D simulations until the stenosis and the artery are co-axial (eccentricity = 0). Eccentricity = [Distance between the axial center of the artery and the axial center of the stenosis]/[Stenosis radius].

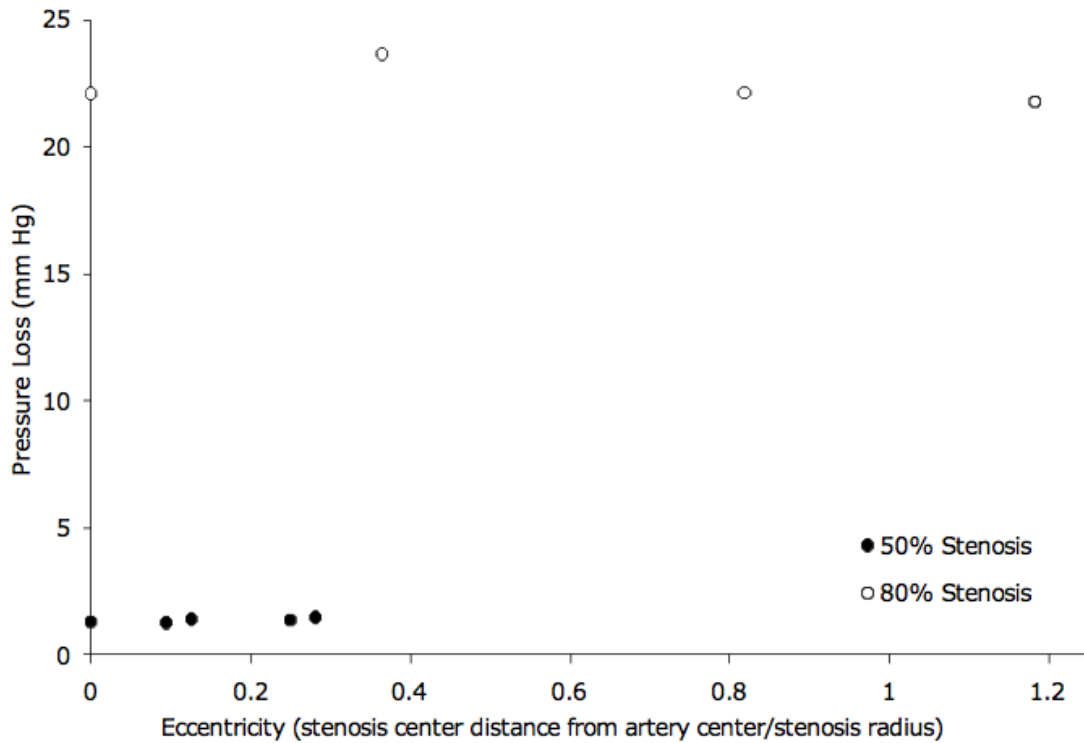


Figure 4.6. Pressure loss versus stenosis eccentricity. Eccentricity is defined as the distance between the axial center of the artery and the axial center of the stenosis divided by the stenosis radius. This definition means the upper limit of eccentricity increases with the extent of occlusion. In other words, the smaller the stenotic lumen, the closer its center can approach the wall of the artery. Simulation conditions are: steady flow; elliptical stenosis; blood viscosity, 0.004 Pascal second; blood density, 1060 kg/m³; blood flow rate through renal artery, 10 mL/second; for 50% stenosis, laminar model; for 80% stenosis, turbulent k-ε model.

CHAPTER 5: RENAL ARTERY ANEURYSM IN TWO-DIMENSIONS

5.1 Renal Artery Aneurysm Geometries and Computational Domain

5.1.1 Renal Artery Aneurysm Geometries

Various saccular and fusiform aneurysm geometries were also examined *in silico*. According to Henke et al. (Henke, 2001), the single most common site for a renal artery aneurysm or RAA is at the primary or main bifurcation of the renal artery. Saccular RAA were modeled by a protuberance out of the Y-juncture, both with and without a neck, for three different values of the aneurysm radius (ranges of 4.175-8.125 mm and 6.5-13 mm, respectively). Simulations of fusiform aneurysms (radii 6.5-19.5 mm) at the main bifurcation were also conducted. In order to determine if aneurysm location on the renal artery has a noteworthy effect on the pressure difference, we examined a saccular aneurysm of the main artery for four different radii (6.5-15.5 mm). Table 5.1 is an illustration of the different geometries where the dimensions for each of the cases studied are provided.

The previously described aneurysms were modeled to give an indication of the effects of typical structures and locations. Currently, a link between RAA structure and hypertension has not been established. It is quite possible that some aneurysm geometries do not result in hypertension. As a result, a patient-specific study, in which the subject had a large RAA of known geometry definitely associated with severe hypertension was modeled, using the geometry described in Degertekin et al. (Degertekin, 2006). In this case, the patient had a large saccular renal artery aneurysm of the main renal artery. The aneurysm was treated using a stent graft, and the patient's

hypertension was greatly diminished. An image of this aneurysm is shown in figure 5.1, as well as the 2D model of the aneurysm geometry.

5.1.2 Computational Domain

5.1.2.1 Boundary Conditions

The simulation conditions were steady, laminar flow, blood flow rate of 10 ml/s (Cooney, 1976), constant velocity at inlet, and constant pressure outlets for all outlets. The physical properties of the blood applied in the simulations were blood viscosity of 0.004 Pa·s and blood density of 1060 kg/m³. For vessels that are large compared to red blood cells, blood can be treated as a Newtonian fluid (Ku, 1997; Yamaguchi, 2006) as shown in models by many investigators (Perktold, 1991; Rindt, 1996; Frauenfelder, 2006; Nguyen, 2008). The renal artery in these simulations was modeled as a 5 mm diameter, smooth wall tube with a length of 50 mm (Kem, 2005).

5.1.2.2 Grid

The aneurysm geometries of interest were created initially in Gambit 2, as a 2D model, fitted with a quadrilateral mesh, and exported into Fluent 6. After preliminary simulation in Fluent, the initial mesh was adapted in regions of high velocity gradient, followed by additional global refinements after subsequent simulation. The number of grid cells required for grid independence varied slightly depending on the size or location of the aneurysm.

5.2 Two-Dimensional Steady Results

The simulation conditions were initially validated by modeling straight tubes without an aneurysm and comparing the results to those calculated using the Hagen-Poiseuille equation.

5.2.1 Effect of Aneurysm on Arterial Pressure Loss

The pressure gradient through the renal artery was calculated as the difference between the average pressure at the outlets and the average pressure at the inlet of the computational domain. Pressure losses for normal and pathologic renal arteries were determined from computation. The pressure gradient for a normal renal artery was quite small at 0.9 mm Hg. Simulations carried out with various RAA incorporated into the renal artery model included the assumption that the weakened walls and the RAA do not deform significantly with time. For any of the simulations with nondeformable saccular or fusiform RAA interposed at the main bifurcation, the pressure loss did not vary significantly from that for a normal renal artery (Table 5.1). Similarly, there was again no significant change in the pressure loss for the simulation interposing a saccular aneurysm on the main artery, compared to a control artery. Thus, values found for the pressure loss in all cases were small (~1 mm Hg), regardless of the location or size of the nondeformable aneurysm. These values are well below the assumed threshold of 10 mm Hg suggested by Yim et al. (Yim, 2004). Since eighty percent of all renal artery aneurysms are saccular and the most common single location for these is the main bifurcation, the values above were not expected.

The results clearly showed that the geometry and location of a nondeformable aneurysm alone could not affect the pressure loss along a renal artery to the point of

causing significant differences relative to the pressure loss along a typical renal artery. This led to the hypothesis that some other phenomenon associated with the aneurysm may be causing a large pressure difference. A plausible explanation could be a blockage occurring due to a bending of the weakened artery wall at the aneurysm, such as the geometry depicted in Figures 5.2-C and D.

5.3 Two-Dimensional Deformed Steady Flow Results

5.3.1 Effect of Deformation on Arterial Pressure Loss

In the second phase of this study, calculations were performed where it was assumed that deformation of the weakened walls had occurred. An examination of the pressure acting on the inner surface of the distal aneurysm-artery wall cusp in the static case (i.e., the undeformed cusp, Figure 5.2B) supports the hypothesis of deflection of the weakened vessel walls into the lumen of the renal artery. Pressure on the inner surface of the aneurysm cusp is greater than the pressure on the opposing surface (i.e., the inner wall of the artery adjacent to the aneurysm). Higher pressure in the aneurysm can be understood from Bernoulli's Law — flow stagnates inside the aneurysm, so the pressure goes up. For the saccular aneurysm of the main branch (Figure 5.2), it was assumed that the walls could deform and that the pressure gradients across the cusp would cause forces that would tend to push the cusp into the lumen of the artery. Initial deflection into the path of the flowing blood yields an even greater pressure difference across the cusp (Figure 5.2C) and, thus, a greater driving force for occlusion. This data demonstrates that this type of blockage can lead to exaggerated pressure gradients. The pressure gradient, as a function of percent occlusion for both saccular aneurysm locations (main renal artery

and renal artery bifurcation), is given in Table 5.1. Figure 5.3 is a plot of the change in pressure across the artery with increasing percent occlusion. As the percent occlusion (i.e., one minus the ratio of the unblocked lumen area over the total lumen area of the artery) increases, the gradient increases. For the saccular aneurysm of the main artery (see Figure 5.2), approximately 60% occlusion leads to the pathologically relevant threshold value of 10 mm Hg. Figure 5.4 is a summary of the proposed mechanism for this aneurysm geometry.

Simulations of blood flow in virtual representations of RAA do not demonstrate a significant pressure loss in the renal artery when the walls of the aneurysm and artery are fixed. This is true even when the simulations mimicked common aneurysm geometries known to be associated with hypertension. Assuming that hemodynamics is an important factor in renin-dependent hypertension, some other phenomenon must be contributing. Further simulations were carried out in which a deformed cusp was imposed. Eliminating the fixed wall constraint seems reasonable, because it is self-evident that the RAA walls are weakened and they are known to collapse when unloaded (Kyriacou, 1996). Importantly, the pressure values obtained from CFD indicate that the associated forces will act so as to initiate deflection of the wall into the artery. Penetration of the cusp into the flow of the artery leads to a greater force inducing deflection, and consequently, greater partial occlusion. As a result of the presence of a constriction at the deflected cusp, CFD calculations demonstrate that a pathologically significant drop in pressure can occur. The results of the CFD simulations could be verified clinically through the use of miniaturized pressure guide wires, which have been used to provide reliable pressure measurements in the renal artery. However, advances in

medical imaging are probably needed to verify the mechanism of occlusion. Gross et al. (Gross, 2001) presented data from a study on renal artery stenoses, in which the pressure gradient across each of 46 stenoses was measured directly. The measured magnitude and trend of the pressure gradients for differing percent stenosis from Gross et al. compare favorably with the values obtained in this study, and serve to validate the computational results.

There is a report in the medical literature with observations consistent with this analysis (Stansby, 1991). Stansby et al. described the case of a hypertensive renal artery aneurysm patient who underwent captopril-renography where evidence of a stenosis was found. However, upon arteriography and during surgery, no stenosis was found. After aneurysm resection, another captopril-renogram was performed and no evidence of a stenosis was observed. This case indicates that an aneurysm-associated constriction could be present, but could go undetected during arteriography or surgery.

A variety of surgical techniques are currently used to treat renal artery aneurysms. Common types of treatment include excising the aneurysm, exclusion with a stent graft, renal artery bypass and aneurysm embolization. Excepting embolization, these treatments would not only exclude the aneurysm, but also halt any hemodynamic effects that would lead to a constriction. For example, a stent graft placed across the aneurysm opening would not only stop blood from flowing into the aneurysm, but would keep the wall of the aneurysm-artery intersection from deflecting into the blood stream. In the case-study examined in this work, the patient was treated with a 5.0x26.0 mm Jostent Graftmaster stent. Our simulation of this pathologic aneurysm was altered to include this stent (with dimensions as specified by the manufacturer), and the results indicated that

the stent would inhibit the formation of an occlusion and that the stent itself had no effect on the pressure loss in the artery. Embolization of renal artery aneurysms is successful in ameliorating hypertension through a different mechanism. Because embolization precludes blood flow into the aneurysm, the Bernoulli effects that lead to high pressure in the aneurysm and subsequent arterial occlusion are not present. In these ways, the surgical treatments now in use may not only be preventing aneurysm rupture, but could also be alleviating renovascular hypertension by eliminating the occlusion.

Deformations occurring for the fusiform aneurysm and the wide-necked saccular aneurysm of the main bifurcation were not modeled, because it was not anticipated that these geometries would lead to deformation into the blood stream. Figure 5.5 is an illustration of the forces acting on the aneurysm wall for the A) fusiform aneurysm, B) wide-necked saccular aneurysm and C) saccular aneurysm with neck, imposed on the contours of pressure calculated from these simulations. The pressure within the fusiform and mild saccular aneurysms would tend to force the walls of the aneurysm out uniformly. In contrast, for the saccular aneurysm with neck, it can be seen how the pressure could force the aneurysm/artery intersection into the blood stream. An interesting outcome of this study is a prediction of the types of aneurysms that would be prone to causing hypertension. Fusiform and wide-necked saccular aneurysms (Figure 5.5) are not expected to form occlusions. Further investigation is required to determine if the ~70% of renal artery aneurysm patients who suffer from hypertension have aneurysm geometries that would tend to occlude blood flow.

The structure of the artery-aneurysm intersection appears to play a vital role in the hemodynamic pressure difference through the artery. This sort of phenomenon may

not be apparent in clinical cases due to the limitations of current medical imaging. This occlusion also might not be observed in autopsy studies due to the flow-induced nature of the deflection. The results imply that the mechanism through which a RAA causes hypertension is probably related to an associated constriction or other distortion of the renal artery, where, similar to a stenosis, an occlusion of 60% or greater is capable of inducing hypertension.

5.4 Conclusions

The variety in shape, size and location of RAA implies that some general phenomenon is causing altered hemodynamics in the artery. This work demonstrates that deflection of a cusp is a plausible mechanism consistent with the principles of fluid mechanics and the known properties of RAAS. This work does not take into account mechanical kinking or twisting of the blood vessel due to the presence of an aneurysm, therefore, that possibility cannot be eliminated. Currently, there appears to be no evidence in support of or opposed to a hypothesis based on kinking or twisting. This sort of event would alter the hemodynamics within the artery, so it is fundamentally consistent with geometric factors leading to a loss of renal artery pressure and resultant renovascular hypertension.

An understanding of the underlying mechanism could prove valuable. Improved detection provides the option of earlier intervention. There is however much debate as to which renal artery abnormalities require medical intervention (Hubert, 1980; Lumsden, 1996; Bastounis, 1998; Hupp, 1992). Knowledge of the mechanism(s) that lead to

secondary hypertension might not only influence when to intervene, but might also help guide clinicians in the specific mode or details of surgery.

Clearly, there is an association between renal artery aneurysms and hypertension. This work illustrates that the presence of an aneurysm alone does not lead to renin-dependent hypertension. In addition, the study shows that a constriction associated with a renal artery aneurysm has the potential to induce hypertension. This analysis also predicts certain types of RAA are more prone to causing hypertension. Since the detailed configuration of the geometric structure of the vessel at the renal artery-renal artery aneurysm intersection appears to be critical in the determination of the hemodynamic pressure drop, high resolution imaging techniques should be used to elucidate this structure. Determining renal artery abnormalities of concern is an important goal that would assist physicians in clinical decision making. In order to extend this study and increase the validity of the transient-occlusion hypothesis, simulations incorporating the distensibility of the arterial wall have been undertaken, as discussed in the following chapter.

Portions of this chapter have been reproduced from the following sources:

Heflin LA, Street CB, Papavassiliou DV, Kem DC, Wu DH, O'Rear EA. *Transient Stenotic-Like Occlusions as a Possible Mechanism for Renovascular Hypertension due to Aneurysm*. Journal of the American Society of Hypertension. 2009; 3:192-200.

5.5 References

Bastounis E, Pikoulis E, Georgopoulos S, Alexiou D, Leppaniemi A, Boulafendis D. Surgery for renal artery aneurysms: a combined series of two large centers. *Eur Urol* 1998; 33:22-27.

Degertekin M, Bayrak F, Mutlu B, Gurses B, Guran S, Demirtas E. Images in cardiovascular medicine. Large renal artery aneurysm treated with stent graft. *Circulation* 2006; 113:e848-849.

Cooney D. *Biomedical Engineering Principles: An Introduction to Fluid, Heat, and Mass Transport Processes*. New York: Marcel Dekker, 1976.

Frauenfelder T, Lotfey M, Boehm T, Wildermuth S. Computational fluid dynamics: hemodynamic changes in abdominal aortic aneurysm after stent-graft implantation. *Cardiovasc Intervent Radiol* 2006; 29:613-623.

Gross C, Krämer J, Weingärtner O, Uhlich F, Luft F, Waigand J, Dietz R. Determination of renal arterial stenosis severity: comparison of pressure gradient and vessel diameter. *Radiology* 2001; 220: 751-756.

Henke P, Cardneau J, Welling T, 3rd, Upchurch G, Jr., Wakefield T, Jacobs L, et al. Renal artery aneurysms: a 35-year clinical experience with 252 aneurysms in 168 patients. *Ann Surg* 2001; 234:454-462; discussion 462-453.

Hubert J, Jr., Pairolero P, Kazmier F. Solitary renal artery aneurysm. *Surgery* 1980; 88:557-565.

Hupp T, Allenberg J, Post K, Roeren T, Meier M, Clorius J. Renal artery aneurysm: surgical indications and results. *Eur J Vasc Surg* 1992; 6:477-486.

Kem D, Lyons D, Wenzl J, Halverstadt D, Yu X. Renin-dependent hypertension caused by nonfocal stenotic aberrant renal arteries: proof of a new syndrome. *Hypertension* 2005; 46:380-385.

Ku D. Blood Flow in Arteries. *Annual Review of Fluid Mechanics* 1997; 29:399-434.

Kyriacou SK, Humphrey JD. Influence of size, shape and properties on the mechanics of axisymmetric saccular aneurysms. *J Biomech* 1996; 29: 1015-1022.

Lumsden A, Salam T, Walton K. Renal artery aneurysm: a report of 28 cases. *Cardiovasc Surg* 1996; 4:185-189.

Nguyen K, Clark C, Chancellor T, Papavassiliou DV. Carotid geometry effects on blood flow and on risk for vascular disease. *J Biomech* 2008; 41:11-19.

Perktold K, Resch M, Peter R. Three-dimensional numerical analysis of pulsatile flow and wall shear stress in the carotid artery bifurcation. *J Biomech* 1991; 24:409-420.

Rindt C, Steenhoven A. Unsteady flow in a rigid 3-D model of the carotid artery bifurcation. *J Biomech Eng* 1996; 118:90-96.

Stansby G, Hilson A, Hamilton G. Renovascular hypertension secondary to renal artery aneurysm detected by captopril-renography. *Eur J Vasc Surg* 1991; 5:343-346.

Yamaguchi T, Ishikawa T, Tsubota K, Imai Y, Nakamura M, Fukui T. Computational Blood Flow Analysis - New Trends and Methods. *J Biomech Sci Eng* 2006; 1:29-50.

Yim P, Cebra J, Weaver A, Lutz R, Soto O, Vasbinder B, Ho V, Choyke P.
Estimation of the differential pressure at renal artery stenoses. *Magn Reson Med*
2004; 51:969-977.

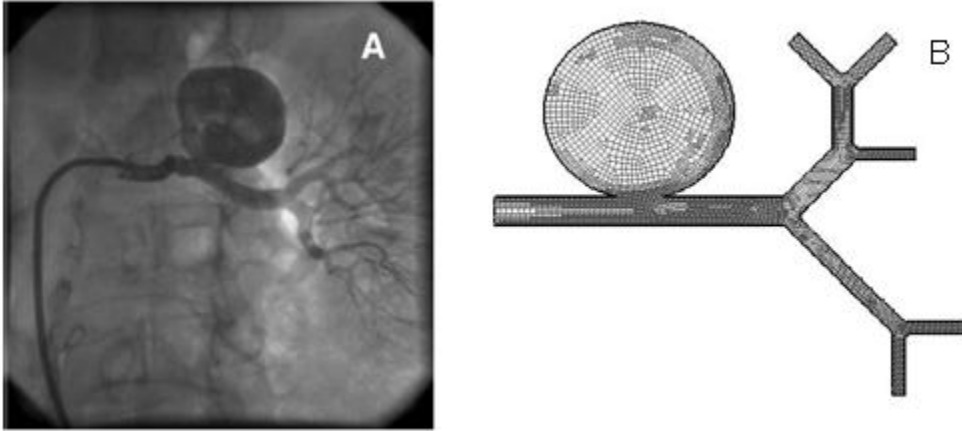


Figure 5.1. (A) Saccular aneurysm of the renal artery (Degertikin)*; (B) 2D mesh representative of pathologic geometry given in Degertikin, et al. (dimensions 33 x 31 mm).

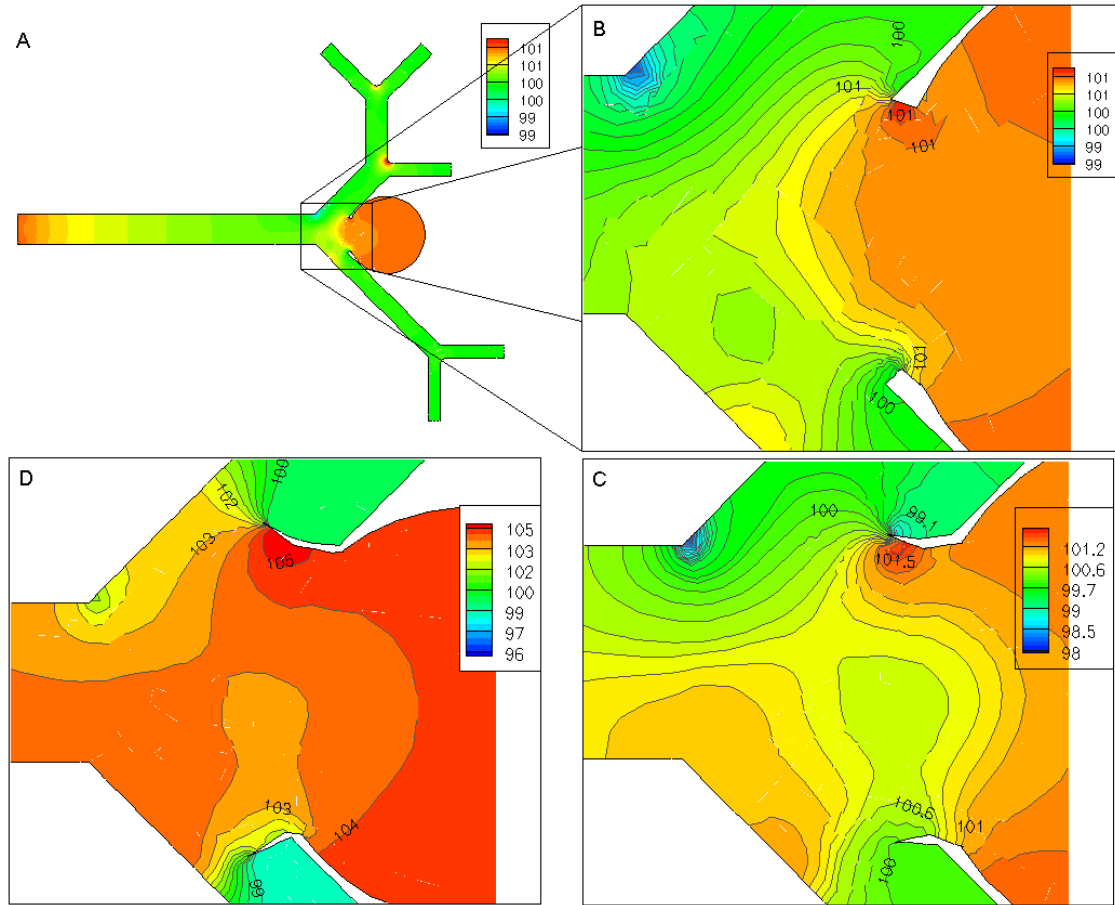


Figure 5.2. Possible progression of occlusion of the renal artery by aneurysm cusp. Pressure values in A, B, C and D are mm Hg A) Saccular renal artery aneurysm of the main bifurcation; B) Close-up showing higher pressure inside the aneurysm when compared to pressure in arterial branches; C) Initial deflection of the aneurysm cusp into the blood stream – the pressure difference across the cusp is larger than before deformation; D) Aneurysm cusp occluding the arterial branches with high pressure on the upstream side of the cusp - up to a 5 mm Hg pressure difference across the cusp.

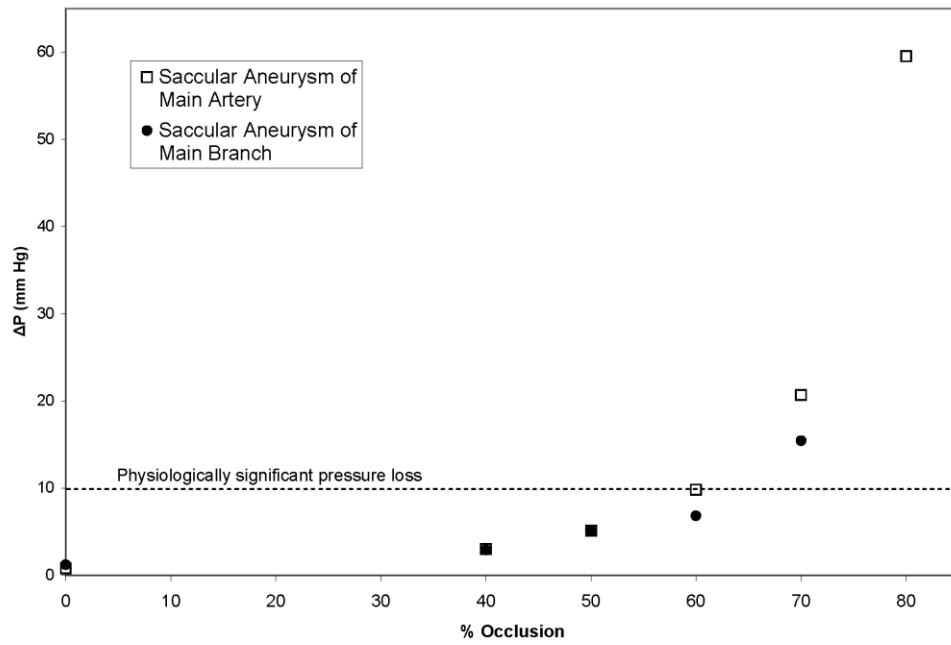


Figure 5.3. Increase in pressure loss across the renal artery with increasing percent occlusion for the saccular aneurysm of both the main artery and the main branch. The dashed line shows where the physiologically relevant pressure loss is reached.

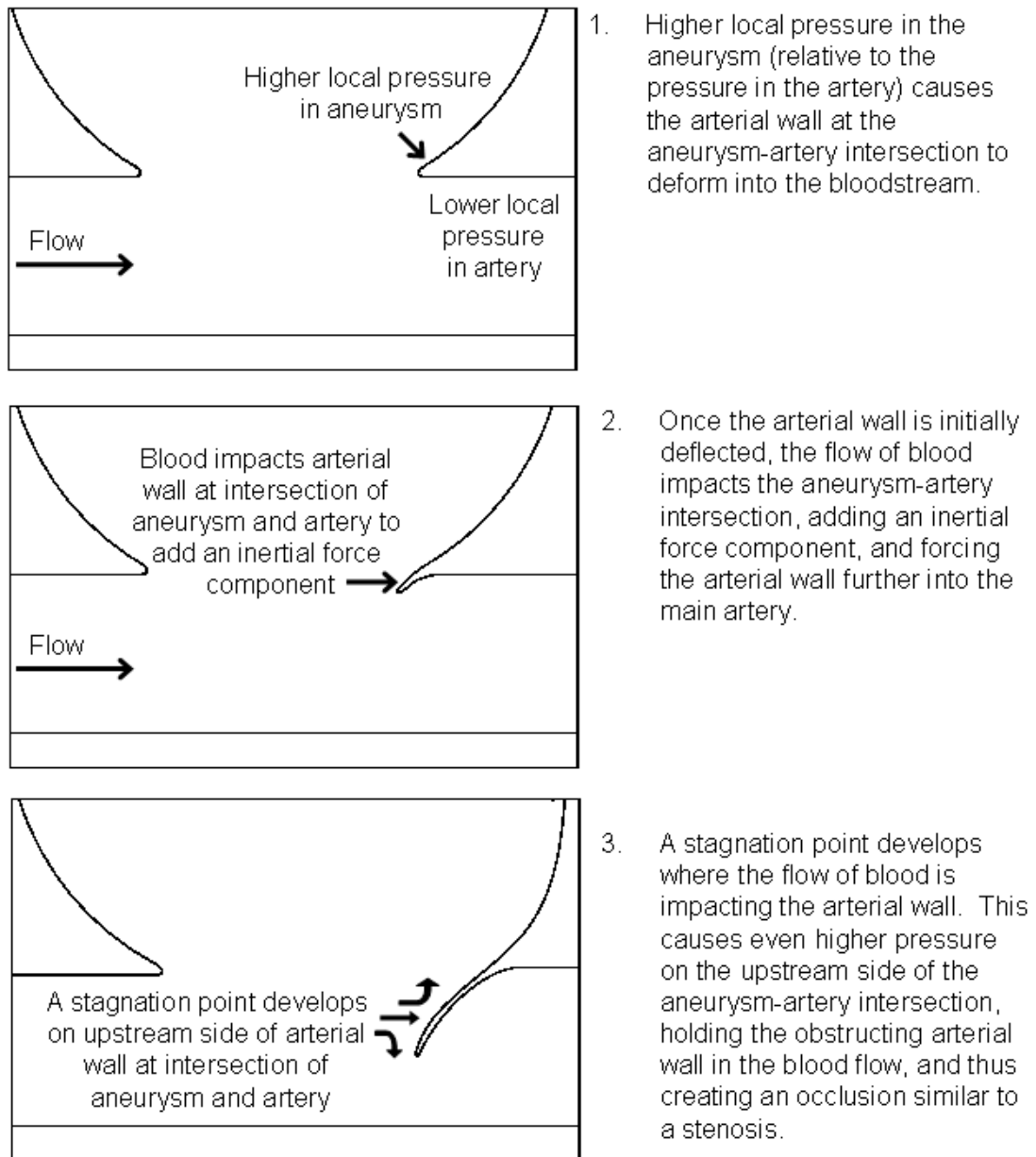


Figure 5.4. Illustration of the proposed mechanism of occlusion for the saccular aneurysm of the main renal artery.

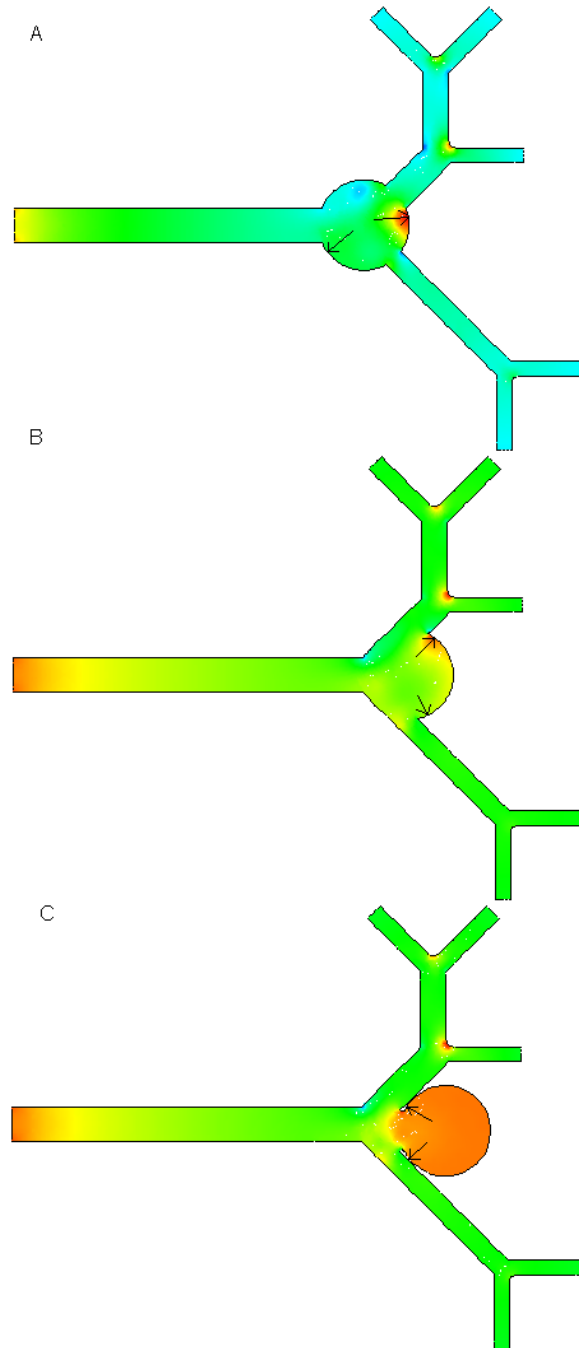


Figure 5.5. The effect of geometry on the predicted correlation between aneurysms and hypertension. A) Pressure inside the fusiform aneurysm would tend to force the walls of the aneurysm outward, B) Similar to the fusiform aneurysm, the walls of the mild saccular aneurysm would be forced outward; C) The forces acting on the walls of the saccular aneurysm with neck would tend to deform the aneurysm lip into the blood stream.

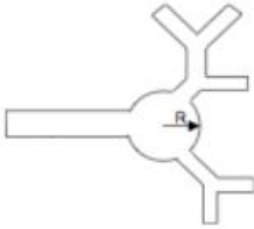
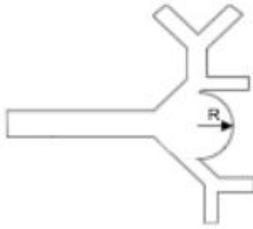
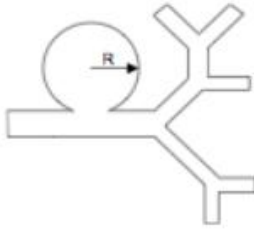
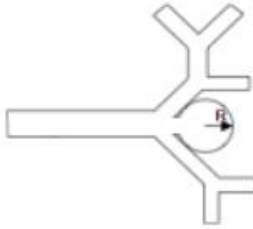
Fusiform aneurysm of main branch		Saccular aneurysm of main branch		Saccular aneurysm of main artery		Saccular aneurysm of main artery with neck ^o	
							
R (mm)	ΔP (mm Hg)	R (mm)	ΔP (mm Hg)	R (mm)	ΔP (mm Hg)	R (mm)	ΔP (mm Hg)
6.50	1.03	6.50	1.21	6.50	0.90	4.88	1.27
9.75	1.02	9.75	1.17	9.75	0.87	6.50	1.20
13.00	1.15	13.00	1.18	13.00	0.87	8.13	1.30
16.25	1.30			15.5	0.80		
19.50	0.88						

Table 5.1 Calculated pressure losses for renal arteries with various aneurysms.

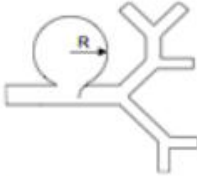
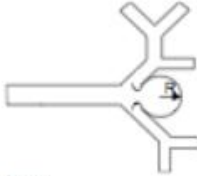
Saccular aneurysm of main artery with constriction		Saccular aneurysm of main branch with constriction	
			
R: 16.5 mm		R: 6.5 mm	
% Occlusion	ΔP (mm Hg)	% Occlusion	ΔP (mm Hg)
70	20.68	70	15.42
60	9.80	60	6.81
50	5.07	50	5.04
40	3.00	40	2.89

Table 5.2. Calculated pressure losses for various aneurysms with imposed occlusions.

CHAPTER 6: RENAL ARTERY ANEURYSM IN THREE-DIMENSIONS

6.1 Introduction to Three-Dimensional RAA Model

6.1.1 Aneurysm Fluid Structure Interaction Literature Review

Fluid structure interaction (FSI) simulations are increasingly being used to investigate the dynamics of aneurysms in various vascular systems, however to date the study of renal artery aneurysms in this manner is lacking. In other systems, for example, fluid structure interaction has been used to study the wall motion of cerebral aneurysms (Balocco, 2010) and aortic aneurysms (Wang, 2011), as well as in the prediction of aneurysm rupture, such as in abdominal aortic aneurysms (Xenos, 2010). In this work, the capabilities of FSI are used in a different way – to understand the influence of the aneurysm on the native artery as opposed to simply the outward movement or pulsation of the aneurysm wall, as previous studies have typically investigated.

6.1.2 Three-Dimensional Aneurysm Geometries

The aneurysm geometries investigated in this fluid-structure interaction portion of the work are similar to those discussed previously that were modeled using rigid-wall, 2D CFD. The length and diameter of the artery were unchanged from the previously discussed RAA geometries, however the angle of the branch and the width of the branching arteries were changed to reflect the average values determined from measurement of multiple images from patients with RAA (Bastounis, 1998; Bisshops, 2001; Degertekin, 2006; Douis, 2008; Gallagher, 2008; Gill, 2001; Henke, 2001; Kem, 2005; Mounayer, 2000; Pfeiffer, 2004; Pfeiffer, 2003; Tan, 2001; Uta, 2008; White, 2009). The simulated geometries are shown in Figures 6.1 and 6.2. Figure 6.1 is a plot of the saccular aneurysm of the main artery model. The typical aneurysm diameter was

1.5 cm (the average size of renal artery aneurysms that are surgically removed), though this value was varied for comparison. Initially, the aneurysm geometry was created by simply intersecting a spherical aneurysm with a cylindrical artery, a geometry that has been used by others as an approximation of an aneurysm with a neck in cerebral aneurysm models (Balocco, 2010). After these simulations, a better neck approximation was created by reducing the aneurysm opening from an elliptical shape to a more circular shape on the downstream edge (see inset of Figure 6.1). This created more surface area on which the pressure inside the aneurysm could act, in order to induce deflection of the cusp into the flowing blood in the artery.

The second geometry investigated was a saccular aneurysm of the main renal artery branch (Figure 6.2), a combination of both the most common type of aneurysm and the most common location. In order to approximate an aneurysm with a neck, the geometry was created to mimic an aneurysm that is sitting tightly against the arterial branch, with a shared wall between the aneurysm sac and the artery. In reality, the wall of a saccular aneurysm overlaps the wall of the artery from which it formed in a more or less laminated structure. The shared wall of the saccular aneurysm model used here is an approximation of the double-layered arrangement of the real aneurysm and arterial walls, and represents the region where these overlap. This approximated aneurysm neck is shown in Figure 6.2. The shared wall of the aneurysm and the artery is highlighted in Figure 6.2E; this is the region in which the mechanical properties of the vessel wall were varied. An aneurysm of the average 1.5 cm size was used, with the center of the aneurysm being placed on the axis line of the arterial branch. Initially, the aneurysm was modeled with a cusp on both the upper and lower branches, meaning there was a shared

wall between the aneurysm sac and both branches of the renal artery. Subsequently, an asymmetrical aneurysm similar to one found in the literature (Trunfio, 2008) was modeled by removing the lower shared wall between the aneurysm and the artery – this sort of aneurysm could be classified as an *asymmetrical wide-necked* aneurysm.

6.1.3 Computational Domain

6.1.3.1 Boundary Conditions

For all simulations, a velocity inlet was specified at the entrance of the renal artery. A constant velocity profile was set at the artery inlet. The outlets were specified as pressure outlets. The inlet velocity for the steady state simulations was 0.5 m/s, which is the average velocity of blood entering the renal artery if a 600 ml/min flowrate is assumed, and the pressure specified at the outlets was 0 Pa. At all boundaries between the fluid and the solid, a fluid-solid interface boundary condition was specified. The solid boundaries at the inlet and outlet of the artery were given a fixed boundary condition.

6.1.3.2 Grid

For all simulations, an unstructured tetrahedral mesh was created for the desired geometry. For most simulations, the mesh was more refined near fluid-solid boundaries and in regions with small geometric features. Initially, a healthy renal artery was modeled, and it was found that the deformation of the arterial wall was of the correct order of magnitude, approximately 5% of the artery diameter, accepted as the approximate deformation of arterial walls *in vivo* (Bertram).

In some cases, convergence was difficult to achieve with this sort of mesh, and a more uniform mesh was created. A uniform mesh is recommended for moving mesh

cases in which convergence is difficult, since such a mesh is known to behave better for simulations with large deformations. The average number of grid cells for all simulations was approximately 100,000 cells.

6.2 Saccular Renal Artery Aneurysm of Main Artery Results

6.2.1 Effect of Aneurysm Geometry

The initial aneurysm geometry of a sphere intersecting a cylinder did not lead to very large deformations of the artery surrounding the aneurysm, as can be seen in Table 6.1. Even when some geometric properties, such as the distance between the aneurysm and artery center, were changed, the deformation did not increase to a value considered capable of causing any effect on the pressure loss in the artery, remaining at a maximum deflection of tenths of a millimeter. For most cases, the arterial wall thickness was 1 mm, but some simulations with a wall thickness of 0.5 mm were performed in order to see the effect of reduced wall thickness, however deflection remained similarly small even with a thinner wall. The basic spherical geometry was the simplest possible approximation of an aneurysm with a neck, but once no significant deformations were seen, a “cusp” was added on the downstream edge of the aneurysm. This cusp was created to more closely resemble the circular opening that appears to be present in saccular aneurysms with a neck. Again, the difference between this and the original geometry can be seen in the inset of Figure 6.1. With the addition of this cusp, the deflection of the arterial wall into the blood flow increased by an order of magnitude, although for this particular configuration the deformations still did not appear significant enough to cause a large pressure loss across the artery. The geometry of the cusp also seems to have a significant

effect on the amount of deformation, with a longer cusp leading to larger deflection. This is clear in Table 6.1, where the simulations with cusp Young's moduli of 1×10^4 Pa and 1×10^5 Pa both exhibited a larger deformation when the cusp length was increased. The longer cusp provides a larger area for the high pressure within the aneurysm to act on, allowing for a larger deflection of the cusp.

6.2.2 Effect of Mechanical Properties

It was expected that the mechanical properties of the aneurysm wall would have a large effect on the deformation observed, so this parameter was varied. While little has been reported about renal artery aneurysm walls, in cerebral aneurysms it is observed that the aneurysm wall is stiffer than the arterial wall, although the mechanical properties can vary around the aneurysm wall, especially in regions where rupture is likely (Ferguson, 1972; Scott, 1972; Steiger, 1989). The exact character and progression of the changes in wall properties during and after the formation of an aneurysm is not well understood, however, so it is possible that the arterial wall near the aneurysm is weakened compared to the artery and other portions of the aneurysm wall. A reduction in the Young's modulus of the cusp led to an increase in the computed deflection of the cusp into the blood flow, a phenomenon that makes sense considering the lessened resistance of the arterial wall to deformation with a reduced Young's modulus. These results can also be seen in Table 6.1 – for the aneurysm with a cusp Young's modulus of 1×10^4 Pa, the deformation is larger than that for 1×10^5 Pa. Additionally, a simulation was completed where the Young's modulus of the aneurysm wall was reduced for comparison. This decrease in Young's modulus leads to a “ballooning” of the aneurysm sac, in which the aneurysm pulled farther away from the artery and expanded in size.

In the saccular aneurysm, it was observed that some of the deformation of the artery that occurred due to the aneurysm was a bulging of the arterial wall where the artery and aneurysm intersected. Because of this, a simple anisotropic model was applied to the arterial solid in order to see if this affected the type of deformation observed. This was accomplished by increasing the circumferential Young's modulus by an order of magnitude. However, the results of this simulation did not show a noticeable effect of the orthotropy of the arterial wall on the deformation, with the magnitude of deformation being an intermediate value between those observed in isotropic simulations at the lower and higher Young's moduli. More investigation of the effect of the anisotropy of arterial tissue should be undertaken, however, using a more complicated material model.

This model of a saccular aneurysm of the main artery is similar to a case study from the literature in which a patient had curable, RAA-dependent hypertension (Degertikin, 2006). The simulations of this similar geometry, however, did not display deformation capable of causing renin-dependent hypertension. This is possibly due to the way in which the geometry of the intersection between the aneurysm and the artery was created in the simulation software; it has become clear that the details of this geometry greatly affect the calculated deformations, and current imaging techniques have not provided accurate characterization of this microstructure. Additionally, it is possible that using a constant inlet velocity profile might obscure the effect of the hemodynamics on this type of aneurysm. It is noted from the literature that the majority of saccular aneurysms occurring along the artery are situated on the top-side of the artery. Because the renal artery intersects the descending aorta almost at a right angle, the velocity profile

of blood entering the renal artery would be expected to be far from flat. The number of aneurysms located on the top of the artery may indicate an effect of this characteristic velocity profile on other regions of the artery – which might also affect how the hemodynamics would influence the movement of the aneurysm and arterial walls.

6.3 Saccular Renal Artery Aneurysm of Main Branch Results

6.3.1 Effect of Mechanical Properties

Similar to the saccular aneurysm of the main artery, the deformation of a saccular aneurysm of the main branch depends largely on the mechanical properties of the diseased arterial wall. A decrease in the Young's modulus of the shared wall cusp for the saccular aneurysm of the main branch leads to a larger deformation of the cusp into the blood flow, in a direction consistent with the hypothesized mechanism for unnecessary activation of the RAAS as described in Chapter 5. That is, the deflection of the cusp between the aneurysm and artery wall is such that the artery is partially occluded. This held true for all cases in which the cusp Young's modulus was decreased. Compared to the cusp deflection seen for aneurysms located on the main artery, the deflection of the cusp of the aneurysm of the main branch is typically larger (see Table 6.2). This larger magnitude of displacement reflects the higher pressure build up in the aneurysm located on the main branch compared to that on the artery, and also the effect of a larger cusp area for this location. The progressive increase in cusp deflection with decreasing Young's modulus can be seen for two cusp thicknesses in Figures 6.3 and 6.4. The percent occlusion was measured at the point of maximum deflection for both the thick and thin cusp, and is plotted versus cusp Young's modulus in Figure 6.5. Clearly, as the

As the cusp Young's modulus is decreased, the percent occlusion increases. Additionally, a thinner cusp leads to a larger occlusion of the artery. The thinnest and weakest cusp in this aneurysm geometry led to higher deflections than any other of the geometries investigated. In addition to these mechanical property variations, simulations were performed in which the aneurysm sac had spatially varying properties, with a stiffer aneurysm cap and a weaker wall close to the artery (specified as distal Young's modulus and proximal Young's modulus, respectively, in Table 6.2). This was done in order to assess how a variable aneurysm wall stiffness, which appears to be the physiological reality, would affect cusp deformation. In Table 6.2 it can be seen that a lower proximal Young's modulus leads to slightly larger deflection of the aneurysm cusp. The percent occlusion for these simulations is also shown in Figure 6.5, and it is clear that a weaker aneurysm wall in the region near the cusp can lead to a larger occlusion of the artery. Figure 6.5 shows that, while the percent occlusion is becoming large for the weakest, thinnest aneurysm walls, the critical percent occlusion of approximately 70% is not yet reached. Notable, however, is that these simulations were performed at the average blood velocity through the renal artery, so it remains possible that the peak velocity may further deform the aneurysm wall and cause a critical occlusion. For the variable Young's modulus case, however, if the aneurysm Young's modulus is decreased further, the aneurysm wall again balloons, which does not allow an occlusion to form.

It is important to note that for this geometry the type of deformation appears to typically be of a nature to occlude the artery without leading to an expansion of the artery elsewhere. This is in contrast to the aneurysm of the main artery, where large cusp deflection is typically coincident with a circumferential expansion of the artery

surrounding the aneurysm. Because the pressure loss due to a constriction is dependent on the reduction of area available to flow, the aneurysm of the main branch appears to more readily lead to the type of deflection capable of causing a larger pressure loss, as opposed to the aneurysm of the main artery, where a compensatory circumferential expansion of the artery may occur.

6.3.2 Effect of Aneurysm Asymmetry

In a case study of a symptomatic renal artery aneurysm, Trunfio et al. describe a patient with a wide-necked renal artery aneurysm (Trunfio, 2008), with the appearance of an asymmetry in which one side of the aneurysm was wide open, with the other side appearing to fold over and sit on the artery wall. A model mimicking this type of aneurysm was created by removing the shared wall cusp on the lower branch of the artery model. This created an asymmetric flow, and this model showed similarly large deformation of the aneurysm cusp (Table 6.2). When the thickness of the cusp was decreased, this deflection became larger. Additionally, as the mechanical properties of this cusp were reduced, the deflection was again increased. The fact that a thinner cusp leads to larger deflection makes sense, because a thinner wall would typically provide less resistance to deflection than a thicker wall. It is apparent that reducing the cusp thickness has a large effect on the cusp deflection, similar to reducing the Young's modulus. This result underscores the importance of the microstructure of the aneurysm. Figures 6.6 and 6.7 show the increasing cusp deflection with decreasing cusp modulus for the asymmetric aneurysm geometries. Clearly, this asymmetric geometry is only capable of leading to an occlusion of one branch of the artery. In this case, the un-occluded branch may receive more flow in order to compensate for the increased resistance of the

upper branch, thus reducing the perceived difference in pressure loss caused by the constriction. Although this shift in flow may occur, symptomatic single branch stenoses are observed clinically, showing that this type of single branch deflection could lead to renin-dependent hypertension

6.4 Conclusions

In this portion of the work, the hypothesis proposed in Chapter 5 was investigated using significantly more complicated Fluid-Structure-Interaction methods. The results of these simulations show that the hemodynamics in a diseased renal artery can in some cases lead to occlusions similar to those known to induce renin-dependent hypertension. Although multiple simplifying assumptions were made in the simulation set-up, it is important to note that the computations were performed using accurate fluid velocities and arterial dimensions, as well as mechanical properties covering a range of values widely used in the modeling of arterial structural mechanics. It is clear from the simulations that the microstructure of the intersection between the aneurysm and the artery is very important. The mechanical properties of the diseased wall also greatly affect the degree of deformation, with a low Young's modulus leading to more deformation and thus larger occlusions. Additionally, the area of the aneurysm/artery cusp influences the degree of deformation, with a larger area leading to more deformation. The thinnest aneurysm cusp was seen to lead to the largest deformations, again emphasizing that the specific structure of the aneurysm/artery intersection is vital. The saccular aneurysm located at the main branch lead to the largest occlusions – saccular aneurysms are the most common type of renal artery aneurysm and the main

branch of the artery is the most common location for an aneurysm (Henke, 2001). This could indicate that the approximately 70% of renal artery aneurysm patients suffering from renovascular hypertension experience this co-morbidity through the mechanism described here. The hypothesis proposed previously for stenotic-like occlusions due to renal artery aneurysm has been shown to be valid for some types of renal artery aneurysms.

6.5 References

Balocco S, Camara O, Vivas E, Sola T, Guimaraens L, Gratama van Andel H, Majoie C, Pozo J, Bijmens B, Frangi A. Feasibility of estimating regional mechanical properties of cerebral aneurysms in vivo. *Med Phys* 37(4): 2010: 1689-1706.

Bastounis E, Pikoulis E, Georgopoulos S, Alexiou D, Leppaniemi A, Boulafendis D. Surgery for renal artery aneurysms: a combined series of two large centers. *Eur Urol* 1998; 33:22-27.

Bisshops R, Popma J, Meyerovitz M. Treatment of Fibromuscular Dysplasia and Renal Artery Aneurysm with Use of a Stent-Graft. *J Vas Interv Radiol* 2001; 12: 757-760.

Degertekin M, Bayrak F, Mutlu B, Gurses B, Guran S, Demirtas E. Images in cardiovascular medicine. Large renal artery aneurysm treated with stent graft. *Circulation* 2006; 113:e848-849.

Douis H, Shabir S, Lipkin G, Riley R. Drug-eluting stent insertion in the treatment of in-stent renal artery restenosis in three renal transplant recipients. *J Vasc Interv Radiol* 2008; 19: 1757-1760.

Ferguson G. Physical factors in the initiation, growth, and rupture of human intracranial saccular aneurysms. *J Neurosurg* 1972; 37: 666-677.

Gallagher K, Phelan M, Stern T, Bartlett S. Repair of complex renal artery aneurysms by laparoscopic nephrectomy with ex vivo repair and autotransplantation. *J Vasc Surg* 2008; 48: 1408-1413.

Gill I, Murphy D, Hsu T, Fergany A, Fettouh H, Meraney A. Laparoscopic Repair of Renal Artery Aneurysm. *J Urol* 2001; 166: 202-205.

Henke P, Cardneau J, Welling T, 3rd, Upchurch G, Jr., Wakefield T, Jacobs L, et al. Renal artery aneurysms: a 35-year clinical experience with 252 aneurysms in 168 patients. *Ann Surg* 2001; 234:454-462; discussion 462-453.

Kem D, Lyons D, Wenzl J, Halverstadt D, Yu X. Renin-dependent hypertension caused by nonfocal stenotic aberrant renal arteries: proof of a new syndrome. *Hypertens* 2005; 46:380-385.

Mounayer C, Aymard A, Saint-Maurice J, Chapot R, Merland J. Balloon-assisted coil embolization for large-necked renal artery aneurysms. *Card Vasc Int Radiol* 2000; 23: 228-230.

Pfeiffer T, Reiher L, Grabitz K, Grunhage B, Hafele S, Voiculescu A, Furst G, Sandmann W. Reconstruction for renal artery aneurysm: Operative techniques and long-term results. *J Vasc Surg* 2003; 37: 293-300.

Pfeiffer T, Müller B, Huber R, Reiher L, Häfele S, Sandmann W. Management of Patients with Renal Artery Stenosis. *Herz* 2004; 29: 76-89.

Scott S, Ferguson G, Roach M. Comparison of the Elastic Properties of Human Intracranial Arteries and Aneurysms. *Can J Physiol Pharmacol* 1972; 50: 328-332.

Steiger HJ, Aaslid R, Keller S, Reulen HJ. Strength, elasticity and viscoelastic properties of cerebral aneurysms. *Heart Vessels* 1989; 5: 41-46.

Tan W, Chough S, Saito J, Wholey M, Eles G. Covered Stent for Renal Artery Aneurysm. *Cath Card Intervent* 2001; 52: 106-109.

Trunfio R, Demertzis S, Van Den Berg JC, Scilari F. A new surgical approach for exclusion of renal artery aneurysms avoiding organ ischemia. *Eur J Vasc Endovasc Surg* 2008; 36: 559-561.

Uta H, Michael K, Hermann P, Martin H, Eckhart B. A rare case of acute renal failure – acute bilateral renal artery embolism. *Nephrol Dial Transplant* 2008; 23: 2095-2097.

Wang X, Li X. Computational simulation of aortic aneurysm using FSI method: Influence of blood viscosity on aneurismal dynamic behaviors. *Comput Biol Med* 2011; 41: 812-821.

White C, Olin J. Diagnosis and management of atherosclerotic renal artery stenosis: improving patient selection and outcomes. *Nat Clin Pract Cardiovasc Med* 2009; 6: 176-190.

Xenos M, Rambhia S, Alemu Y, Einav S, Ricotta JJ, Labropoulos N, Tassiopoulos A, Bluestien D. Patient based abdominal aortic aneurysm rupture risk prediction combining clinical visualizing modalities with fluid structure interaction numerical simulations. *Conf Proc IEEE Eng Med Biol Soc.* 2010: 5173-5176.

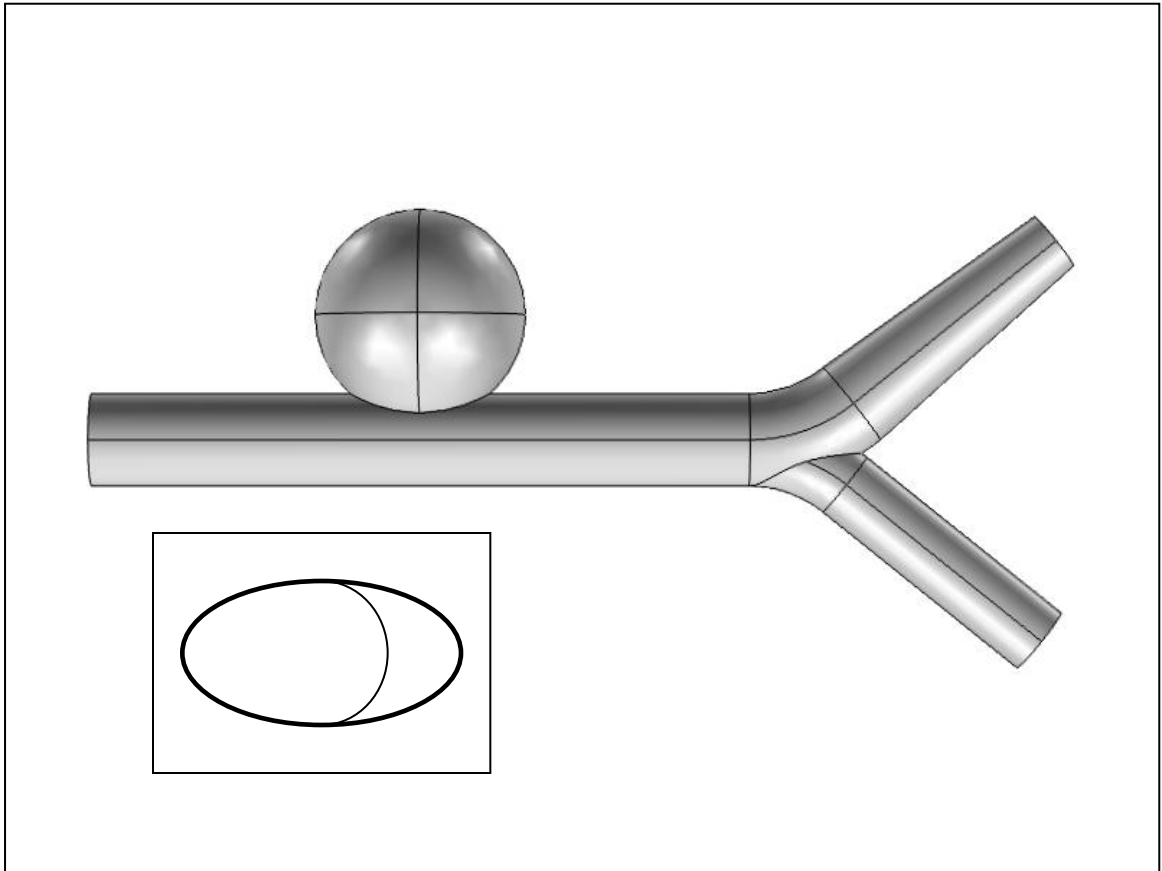


Figure 6.1. Saccular Aneurysm of Main Artery Geometry. The aneurysm is located in the middle of the artery, which has a length of 50 mm. A 1.5 mm aneurysm is shown. Inset: Original (heavy line) and revised (light line) neck geometries.

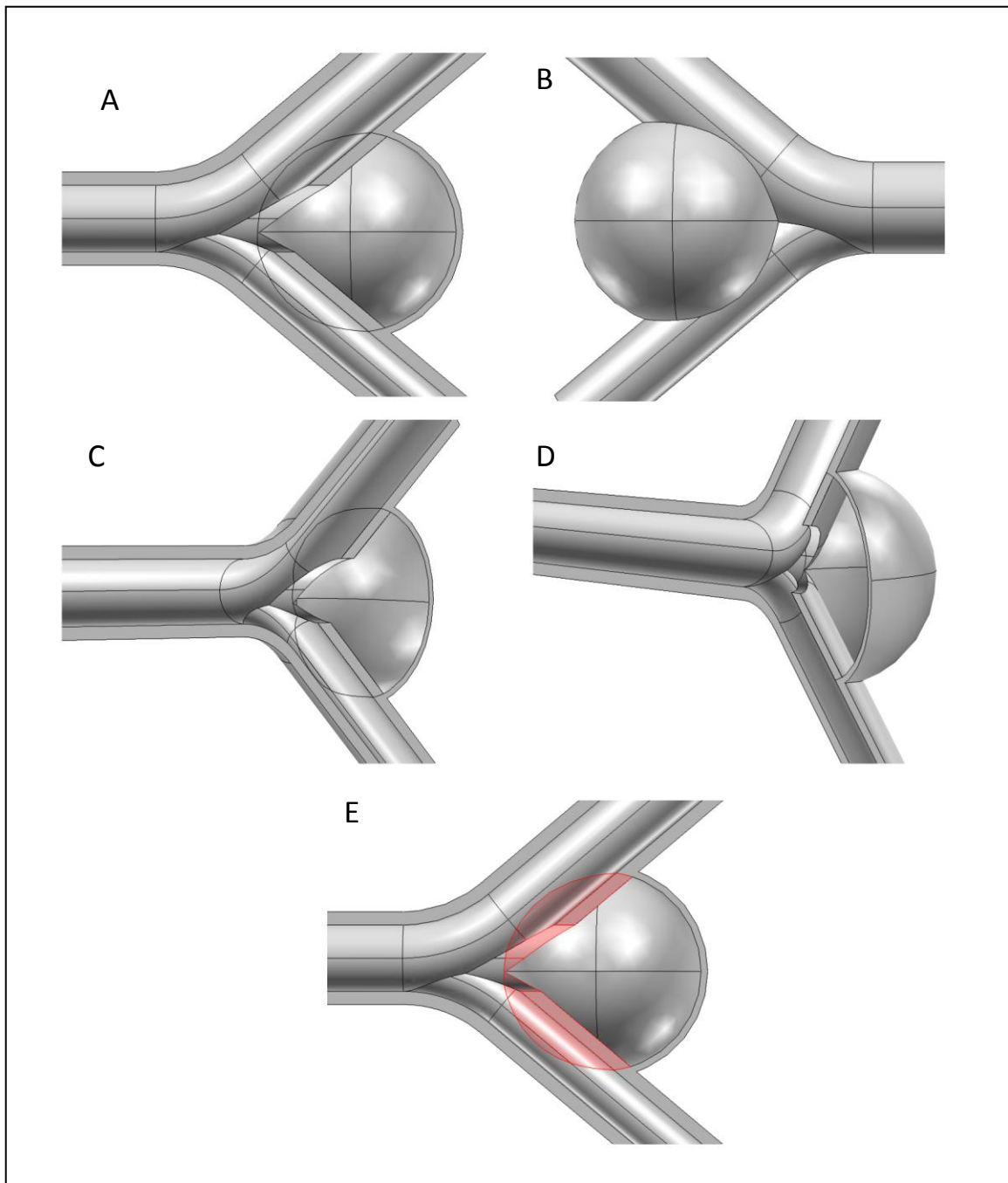


Figure 6.2. Saccular aneurysm of the main branch geometry. A) Cut-away view of artery and aneurysm. B) Exterior view of artery and aneurysm. It is clear that the aneurysm is resting tightly against the artery branch. C) and D) Two different perspectives of the entrance to the aneurysm, showing the opening in the artery wall that leads to the aneurysm. E) Cut-away view of aneurysm, with cusp domain highlighted in red.

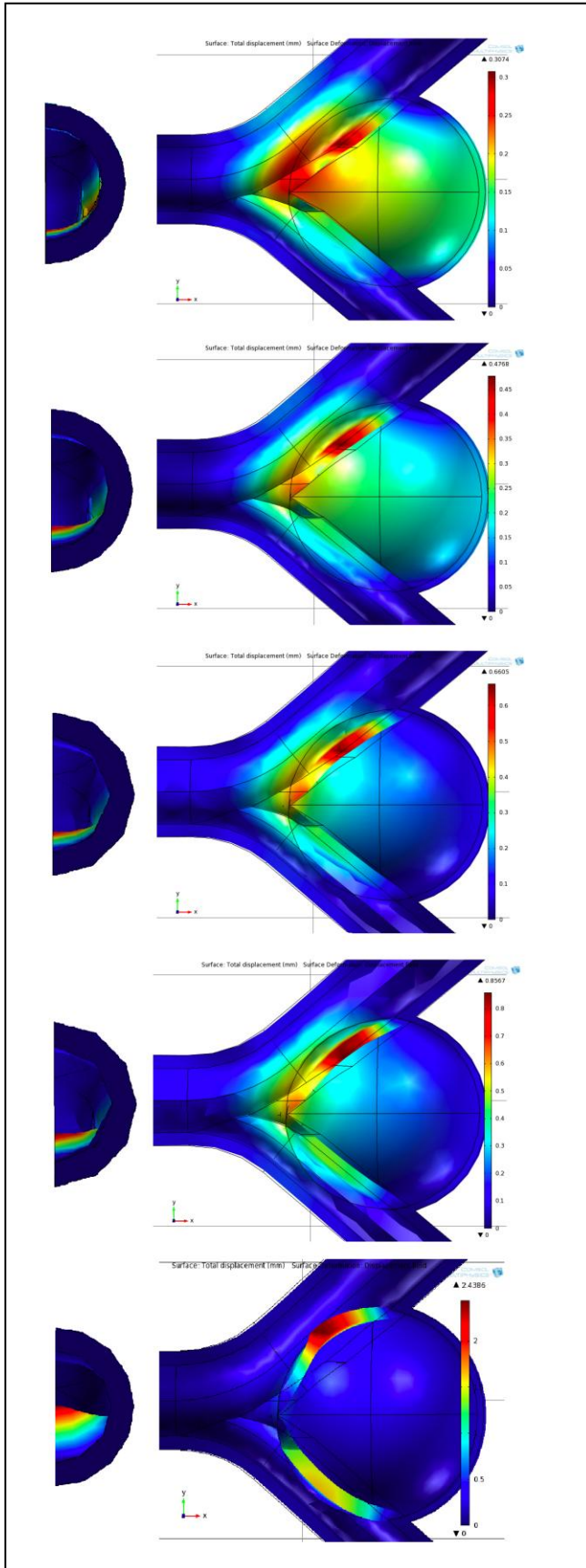


Figure 6.3. Decreasing Young's modulus for symmetric saccular aneurysm of the main artery. The perspective on the left is looking down the upper branch, towards the occlusion. From top to bottom, the cusp Young's moduli are 1×10^5 , 5×10^4 , 1×10^4 , 5×10^3 and 1×10^3 Pa. The deflection of the cusp increases with decreasing Young's modulus

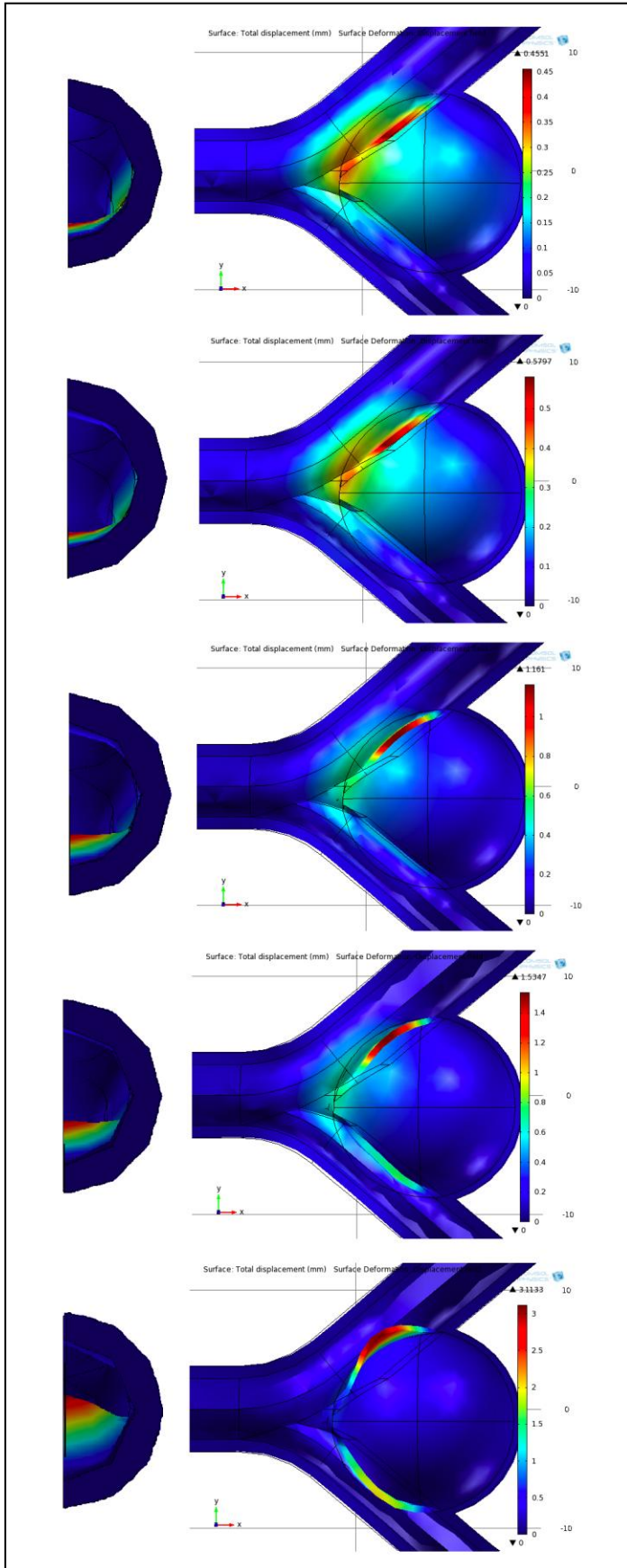


Figure 6.4. Decreasing Young's modulus for symmetric saccular aneurysm of the main artery, thin cusp. The perspective on the left is looking down the upper branch, towards the occlusion. From top to bottom, the cusp Young's moduli are 1×10^5 , 5×10^4 , 1×10^4 , 5×10^3 and 1×10^3 Pa. The deflection of the cusp increases with decreasing Young's modulus.

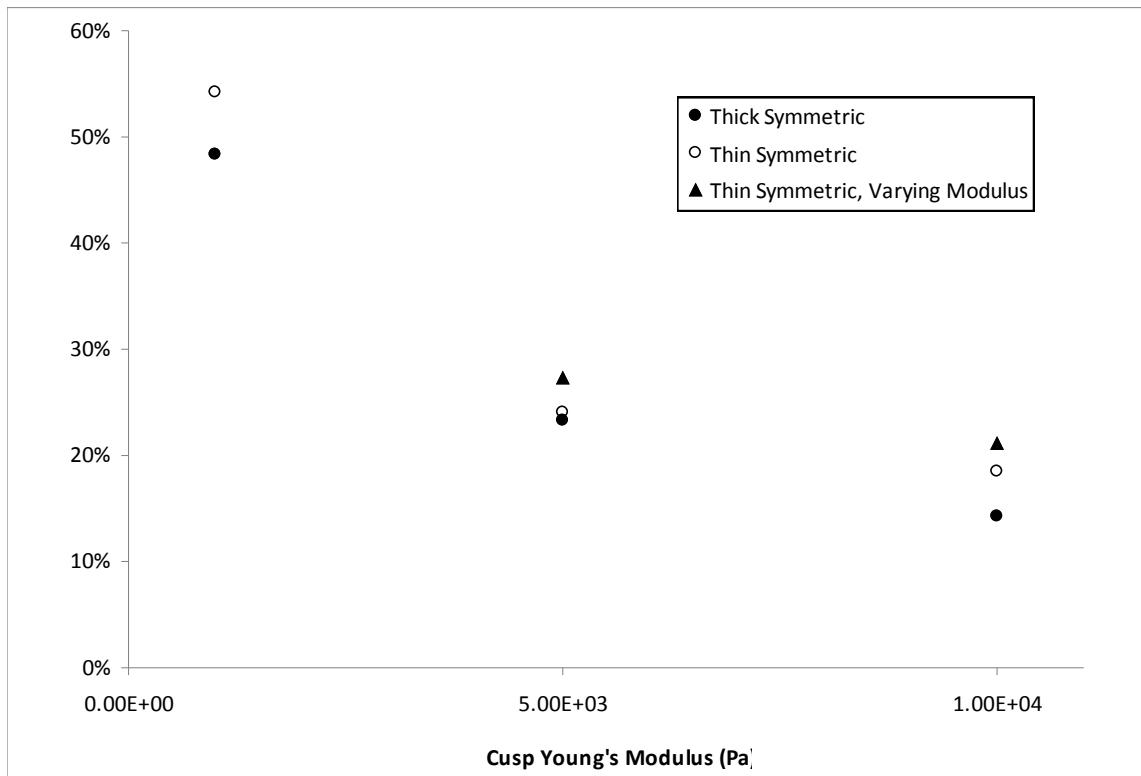


Figure 6.5. Percent Occlusion versus cusp Young's modulus for a symmetric aneurysm of the main branch. The measured maximum percent occlusion increases with decreasing Young's modulus, and also with a thinner wall. Thick = 1 mm. Thin = 0.5 mm.

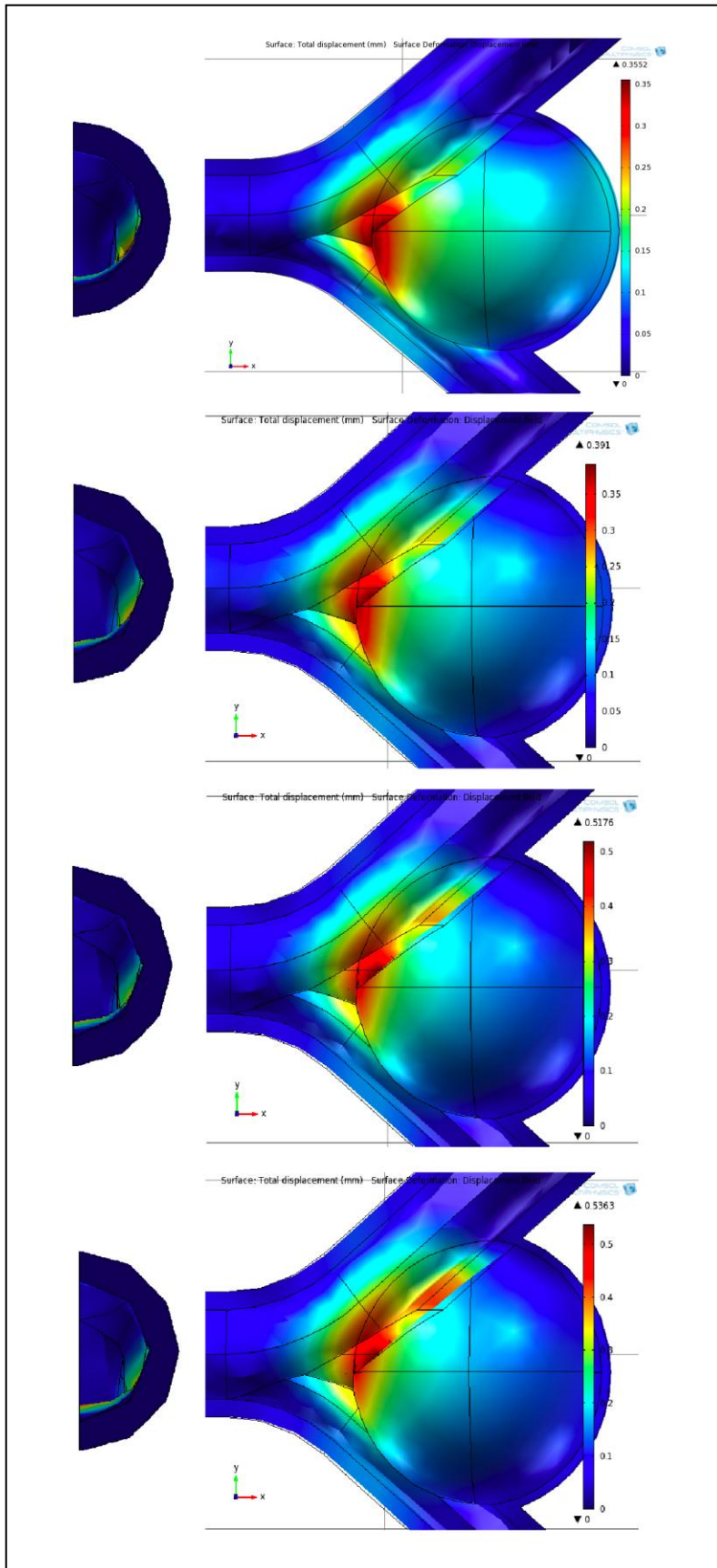


Figure 6.6. Decreasing Young's modulus for asymmetric saccular aneurysm of the main artery. The perspective on the left is looking down the upper branch, towards the occlusion. From top to bottom, the cusp Young's moduli are 1×10^5 , 5×10^4 , 1×10^4 , and 5×10^3 Pa. The deflection of the cusp increases with decreasing Young's modulus.

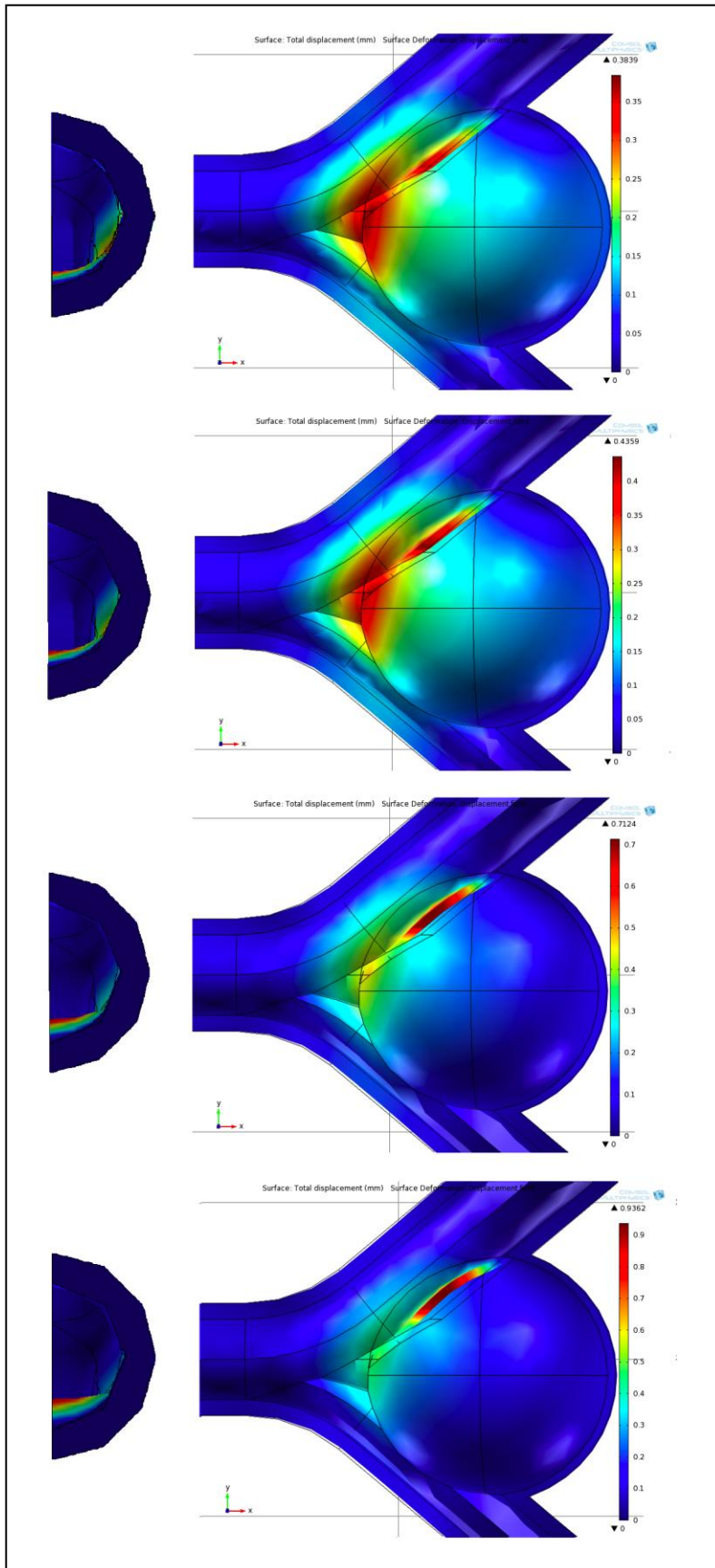


Figure 6.7. Decreasing Young's modulus for asymmetric sacular aneurysm of the main artery, thin cusp. The perspective on the left is looking down the upper branch, towards the occlusion. From top to bottom, the cusp Young's moduli are 1×10^5 , 5×10^4 , 1×10^4 and 7.5×10^3 Pa. The deflection of the cusp increases with decreasing Young's modulus.

Main Artery Geometry										
Aneurysm Type	Aneurysm Radius (mm)	Cusp Thickness (mm)	Cusp Length (mm)	Aneurysm I (Pa)	Artery I (Pa)	Cusp I (Pa)	Max Deformation (mm)	% Occlusion	ΔP (mm Hg)	
Spherical	7.5	N/A	N/A	3.00E+07	1.00E+06	N/A	0.01	-	-	-
Spherical	7.5	0.25	4	1.00E+06	1.00E+05	1.00E+05	0.05	-	-	-
Spherical	7.5	0.25	4	1.00E+06	1.00E+05	1.00E+04	0.26	10%	4.2	
Spherical	10	0.25	5	1.00E+06	1.00E+05	1.00E+04	0.36	13%	4.2	
Spherical	7.5	0.25	4	1.00E+06	1.00E+05	1.00E+04	0.33	13%	4.2	
Spherical	7.5	0.25	4	1.00E+06	1.00E+05	5.00E+03	0.4	13%	4.2	
Spherical	7.5	0.25	5	1.00E+06	1.00E+05	5.00E+03	0.62	18%	4.2	

Table 6.1. Saccular aneurysm of the main artery simulations performed.

Main Branch Geometry									
Aneurysm Type	Aneurysm Radius (mm)	Cusp Thickness (mm)	Aneurysm E (Pa)	Artery E (Pa)	Cusp E (Pa)	Max Deformation (mm)	% Occlusion	ΔP (mm Hg)	
Spherical	7.5	1	1.00E+05	1.00E+05	1.00E+05	0.31	10%	3.7	
Spherical	7.5	1	1.00E+05	1.00E+05	5.00E+04	0.48	12%	3.9	
Spherical	7.5	1	1.00E+05	1.00E+05	1.00E+04	0.66	14%	7.8	
Spherical	7.5	1	1.00E+06	1.00E+05	5.00E+03	0.86	23%	8.3	
Spherical	7.5	1	1.00E+06	1.00E+05	1.00E+03	2.4	48%	7.8	
Spherical	7.5	0.5	1.00E+05	1.00E+05	1.00E+05	0.46	7%	6	
Spherical	7.5	0.5	1.00E+05	1.00E+05	5.00E+04	0.58	14%	6.1	
Spherical	7.5	0.5	1.00E+05	1.00E+05	1.00E+04	1.16	18%	6.2	
Spherical	7.5	0.5	1.00E+05	1.00E+05	5.00E+03	1.53	24%	8.1	
Spherical	7.5	0.5	1.00E+05	1.00E+05	1.00E+03	3.11	54%	8.9	
Spherical	7.5	0.5	P/D: 5.0E+04/1.00E+06	1.00E+05	1.00E+04	1.13	21%	8.3	
Spherical	7.5	0.5	P/D: 5.0E+04/1.00E+06	1.00E+05	5.00E+03	1.42	27%	8.4	
Spherical Asymmetric	7.5	1	1.00E+05	1.00E+05	1.00E+05	0.22	5%	5.6	
Spherical Asymmetric	7.5	1	1.00E+05	1.00E+05	5.00E+04	0.25	6%	7.8	
Spherical Asymmetric	7.5	1	1.00E+05	1.00E+05	1.00E+04	0.36	7%	7.8	
Spherical Asymmetric	7.5	1	1.00E+05	1.00E+05	5.00E+03	0.42	7%	7.8	
Spherical Asymmetric	7.5	0.5	1.00E+05	1.00E+05	1.00E+05	0.38	7%	5.8	
Spherical Asymmetric	7.5	0.5	1.00E+05	1.00E+05	5.00E+04	0.44	6%	5.8	
Spherical Asymmetric	7.5	0.5	1.00E+05	1.00E+05	1.00E+04	0.71	9%	7.5	
Spherical Asymmetric	7.5	0.5	1.00E+05	1.00E+05	7.50E+03	0.94	12%	7.6	

Table 6.2. Saccular aneurysm of the main branch simulations performed. P/D = Proximal Aneurysm Young's Modulus/Distal Aneurysm Young's modulus for aneurysm with variable stiffness.

CHAPTER 7: CONCLUSIONS

7.1 Conclusions

7.1.1 Hemolysis

Interest in the accurate estimation of hemolysis from computational methods clearly remains high, as more and more investigators are using CFD estimations to establish safety of proposed blood contacting devices. The simulations performed here show that hemolysis observed in laminar capillary entrance flow is related to the extensional components of the stress tensor. A threshold value of the extensional stresses of 3000 Pa for exposure times on the order of microseconds is proposed based on the computational results of the simulated experimental work. In addition to this evident threshold value, a mechanism based on accepted characteristics of red blood cells through which extensional flow would lead to hemolysis was developed. The indication that extensional stresses are related to hemolysis does not exclude hemolysis due to shear stresses, however it does indicate that extensional stresses should be taken into account when estimating hemolysis with CFD. In addition to the laminar flow simulations, modeling of a turbulent Couette flow viscometer experimental set-up was also completed, and suggested that hemolysis in a turbulent flow may be related to the Kolmogorov Length Scale for the flow, rather than the Reynolds stresses. Hemolysis appears to have some dependence on the median Kolmogorov Length Scale in the turbulent Couette viscometer. Additional research into this relationship should be pursued, as flows similar to that seen in the Couette viscometer are observed in some blood contacting devices, such as some centrifugal blood pumps.

7.1.2 Renovascular Hypertension

Atherosclerosis in the renal arteries can lead to the formation of stenoses, which are known to cause renin-dependent hypertension. This ability to unnecessarily induce the renin-angiotensin-aldosterone hormonal control system is considered to be related to the pressure loss caused by the constricted artery. Through the use of computational fluid dynamics, it was possible to investigate the effect of stenosis shape on this pressure loss across the artery, as well as the effect of percent stenosis on this pressure loss. Results from these simulations showed that the pressure loss across a stenosis is not strongly related to the axial position of the stenosis or the stenosis eccentricity. The percent stenosis, as expected, has a large effect on the pressure loss across the stenosis, reaching a critical value at approximately 75%. This confirms the rule of thumb generally accepted by physicians to indicate a hemodynamically significant stenosis. This critical stenosis is characterized by a pressure loss of 10 mm Hg and a drastic increase in pressure loss with increasing percent stenosis. The stenosis shape was also found to have a large effect on the calculated pressure loss, with a blunt stenosis leading to the largest losses, followed by a conical stenosis, and then an elliptical stenosis. The difference in pressure loss between stenosis shapes increases after the critical percent stenosis is reached. It is evident that the fraction of area occluded is the parameter most strongly related to pressure loss in stenoses, however the immediate structure of the stenosis also appears to have a significant effect.

Renal artery aneurysms are additionally known to be related to renin-dependent hypertension, although currently no clinical understanding of this phenomenon is available. In fact, there is much debate among physicians as to which aneurysms require

surgical intervention (Hubert, 1980; Lumsden, 1996; Bastounis, 1998; Hupp, 1992). Through the simulation of generalized renal artery aneurysm models, assuming rigid walls, it became clear that a renal artery aneurysm alone is not capable of causing a hemodynamically significant pressure loss. High pressure within the aneurysm did, however, indicate that an aneurysm related occlusion might form and be responsible for a larger pressure loss across the artery. Through the inclusion of a cusp in the rigid wall model, it became clear that a transient stenotic-like occlusion associated with a renal artery aneurysm might be capable of causing a large enough pressure loss to induce renin-dependent hypertension.

This hypothesis was further investigated through the use of fluid-structure-interaction simulations in which the fluid flow and distensibility of the arterial wall were coupled. These simulations showed that, for some renal artery aneurysm geometries, the hypothesis that high pressure within the aneurysm can lead to an occlusion of the blood flow in the artery is plausible. The saccular aneurysm of the main branch, a geometry that combines the most common location and aneurysm type, was seen to allow for the most deformation of the arterial wall. The mechanical properties, specifically the Young's modulus, were shown to have a large effect on the degree of arterial wall deformation, with a lower Young's modulus allowing for greater deflection of the aneurysm cusp. The area of the cusp was shown to have an effect as well, with a larger aneurysm cusp leading to larger deflection. Perhaps one of the more significant conclusions from this work is that the aneurysm/artery intersection microstructure is vital to the calculated deformations, and thus greater resolution of this morphology is necessary for the accurate prediction of the deformations of the arterial wall.

7.2 Suggested Future Work

There is much evidence to suggest that extensional stresses may be vital to the accurate estimation of red blood cell damage in flow. Additional research should be undertaken not only to attempt the reproduction of these results in other systems, but also to improve the experimental measurement of hemolysis in the simulated systems. Even very recently, the inaccuracy and lack of precision in results from the current methods of hemolysis measurement is high, and better measurements can only lead to better estimation of hemolysis from computational methods. The flow of blood in various systems should be modeled in order to determine whether extensional stresses are correlated to hemolysis in other systems.

By adding the fluid-structure-interaction simulations to the set of renal artery aneurysm models, it has been shown that the proposed mechanism through which renal artery aneurysms may lead to renovascular hypertension is valid for some cases. This model could be greatly improved, and more accurate estimates of the percent occlusion resulting from specific aneurysms attained, through the addition of accurate anisotropic, viscoelastic material models for the arterial wall. In addition, through collaboration with physicians, a more accurate measurement of the microstructure of the aneurysm/artery intersection should be determined in order to incorporate this into the model, as the details of this geometry are clearly integral to the degree and type of deformation.

7.3 References

Bastounis E, Pikoulis E, Georgopoulos S, Alexiou D, Leppaniemi A, Boulafendis D. Surgery for renal artery aneurysms: a combined series of two large centers. *Eur Urol* 1998; 33:22-27.

Hubert J, Jr., Pairolero P, Kazmier F. Solitary renal artery aneurysm. *Surgery* 1980; 88:557-565.

Hupp T, Allenberg J, Post K, Roeren T, Meier M, Clorius J. Renal artery aneurysm: surgical indications and results. *Eur J Vasc Surg* 1992; 6:477-486.

Lumsden A, Salam T, Walton K. Renal artery aneurysm: a report of 28 cases. *Cardiovasc Surg* 1996; 4:185-189.